PEOPLE'S DEMOCRATIC REPUBLIC OF ALGERIA

MINISTRY OF HIGHER EDUCATION
AND SCIENTIFIC RESEARCH
FERHAT ABBAS SETIF-1 UNIVERSITY
FACULTY OF SCIENCES
DEPARTMENT OF PHYSICS

Université Ferhat Abbas Sétif 1

THESIS PRESENTED FOR OBTAINING the PhD degree

Domain: Matter Science **Field:** Physics

Speciality: Radiation and matter

Presented by:

Maroua BENGROUN

Theme

Study of Radioelements and Heavy metal Transfer from Soil to Plants: Nuclear Techniques Optimization by Monte Carlo simulation for quantitative analysis

Defended on: 10/01/2024

In front of the jury composed of:

M.	KHARFI Faycal	Professor	Ferhat Abbas Setif-1 University	President
Mme.	AMRANI Naima	Professor	Ferhat Abbas Setif-1 University	Supervisor
M.	AZBOUCHE Ahmed	Senior researcher	CRNA- Algiers	Co-Supervisor
M.	MAOUCHE Djamel	Professor	Ferhat Abbas Setif-1 University	Examiner
M.	KHELIFI Rachid	Professor	Saad Dahlab Blida-1 University	Examiner
M.	BENTRIDI Salaheddine	Doctor	Khemis Miliana University	Invited

Academic year : 2023/2024

ACKNOWLEDGEMENTS

Alhamdulillah, I begin by expressing my deepest gratitude and thanks to Allah, the Most Merciful and the Most Gracious, for his blessings, guidance, and unwavering support throughout my journey of pursuing this thesis.

I would like to thank my supervisors, Dr Ahmed AZBOUCHE senior researcher in CRNA for his kind advice and helpful guidance, and Prof Naima Amrani, for her friendly attitude and support throughout this thesis work. Their encouragement provided me with an opportunity to work freely on my thesis.

I am deeply grateful to Professor Faycal KHARFI for chairing the jury, and Professors Djamel MAOUCHE, Rachid KHLIFI and Dr Salaheddine BENTRIDI for accepting the role of examiners in my thesis defense. Their expertise, critical evaluation, and valuable feedback will significantly contribute to the completion of this work.

I extend my gratitude to all the individuals who have supported me throughout my academic journey, including my family, friends and colleagues. I am immensely thankful to Dr. Louiza BOUNEMIA for the support and encouragement you have provided me, and for your contribution to my academic success. You have been a source of inspiration for me, and you have helped build my self-confidence and unlock my full potential.

The last but not least, I would like to express my heartfelt thanks to my parents for their support, love, and belief in my abilities. Their encouragement, sacrifices, and constant motivation have been instrumental in my academic journey. I am truly grateful for their guidance, understanding, and the values they instilled in me, which have shaped the person I am today.

"Nothing in life is to be feared, it is only to be understood. Now is the time to understand more, so that we may fear less."

Marie Curie

Table of contents

ACKNOWLEDGEMENTS II

TABLE OF CONTENTS IV

FIGURES LIST VI

LIST OF TABLES VIII

GENERAL INTRODUCTION 1

CHAPTER I. BACKGROUND THEORY 5

I.1 RADIOACTIVITY AND ITS SOURCES 5
1.1 Natural radioactivity 5
1.2 Artificial radioactivity 6
1.3 Radioactive decay chain 6
1.4 Radioactive families 7
1.5 Secular equilibrium 8
1.6 Gamma Ray Interaction with Matter 8
A. Rayleigh scattering 9
B. Photoelectric effect 10
C. Compton scattering 11
D. Pair production 12
1.7 Photon beam attenuation 12
1.8 Self-absorption effect 13
1.9 Coincidence summing effect 14
1.10 Interaction of electrons with matter 16
A. Ionization process 16
B. Bremsstrahlung radiation 16
C. Multiple coulomb interaction 17
D. Positron interaction (Annihilation) 17
1.11 Mean path of charged particle through matter 17
1.12 Detectors 18
1)Semi-conductor detectors 18
A. N-type semiconductors 18
B. P-type semiconductors 18
2) Scintillation Detectors 18
3) HPGe detectors 19
1.13 Detector specifications 20
1) Energy resolution 20
2) Detection efficiency 20
I.2 NUCLEAR TECHNIQUES 21
2.1 Gamma Spectrometry technique 21
2.1.1 Detection setup 21
2.1.2 Spectrum analysis 22
1) Energy calibration 22
2) Efficiency calibration 23
2.1.3 Background noise 23
2.1.4 Detection limit 24
2.2 X-Ray Fluorescence technique (XRF) 24
2.2.1 EDXRF (Energy Dispersive X-ray fluorescence) working principle 24
X fluorescence spectrum 26

2.2.2 Wavelength dispersive X-ray fluorescence technique 26
WD-XRF working principle 27
2.3 Quantitative X-ray Spectra analysis 28
I.3 Monte Carlo technique 28
3.1 Monte Carlo methods 28
3.2 Random number generator 29
3.3 Radiation transport 29
3.4 Monte Carlo codes 29
3.5 MCNP code 31
3.6 MCNP code structure 31
Input File 31
A.Geometry specifications 32
B.Surface cards 32
C.Cell cards 33
D.Data specifications 33
E.MODE card 33
F.Tally specification cards 33
G.Materials specification 33
H.Source specifications 34

CHAPTER II. MATERIALS AND METHODS 34

II.1 Experimental device of the gamma spectrometry technique laboratory 34
1.1 HPGe detector 34
1.2 DSA (Digital Spectrum Analyzer) system 35
1.3 Genie 2000 software 35
1.3.1 Hardware Configuration Editor: 35
1.3.2 Certificate Editor: 35
1.3.3 Library Editor: 36
1.3.4 MCA Input Definition: 36
1.3.5 Acquisition and Gamma Analysis: 36
II.2 Calibration of the measurement chain 36
Energy calibration: 36
II.3 Laboratory Standard Preparation 37
II.4 Efficiency calibration using the standard preparation 38
II.5 Monte Carlo simulation 39
Modelling of source-HPGe detector MCNP5 39
II.6 Characterization of soil and plant matrices using WD-XRF technique 41
Sample preparation for WD-XRF analysis 41
II.7 EDXRF system Instrumentation 42
7.1 Sample preparation for XRF analysis 42
7.2 Spectrum analysis 42

CHAPTER III. RESULTS AND DISCUSSION 45

III.1. Energy and efficiency calibration curves in the Gamma measurement chain 45
III.2. Validation of the detector-source model 48
III.3. Study of sample density effect on gamma energy efficiencies using MCNP5 model 52
III.4. Determination of self-absorption correction factors using the developed model 54
III.5. XRF results 59

CHAPTER IV. SOIL TO PLANT TRANSFER FACTOR APPLICATION 62
IV.1 SOIL TO PLANT TRANSFER FACTOR APPLICATION 62
1.1 Mobility of environmental radionuclides in the Soil 62
1.2 Radionuclides soil-plant transfer factor mechanism: 63
1.3 Crops characteristics used in research study 63
1.4 Soil-to crop transfer factors determination 64
1.5 Radiological indices estimation 65
Radium equivalent activity ($Raeq$) 65
Internal Hazard Index (Hint) 65
Absorbed dose rate (Dγ) 65
Annual effective dose equivalent (AEDE) 66
Annual gonadal dose equivalent (AGDE) 66
1.6 Samples collection and preparation 66
1.7 Radioactivity concentration measurements 67
1.8 Radiation hazard indices 69
1.9 Soil-plant Transfer factors 70
1.10 Transfer of metals and trace elements 70
1.11 Determination of the heavy metals transfer 71
1.12 Variation of transfer factors in function of the activity concentrations of radionuclides in soil 73
IV.2 ABSORBED FRACTION BY PLANT FOR THE EROSION CORRECTION MODELS 75
2.1 Theoretical models for cultivated soils used in erosion estimation 75
Proportional Model: 76
Simplified Mass Balance Model (Mass Balance Model 1): 77
Mass Balance improved model (Mass balance 2): 77
Mass Balance Model Incorporating Soil Movement by Tillage (Mass Balance Model 3): 78
2.2 Study of the cesium-137 transfer in cultivated areas 79

GENERAL CONCLUSION 81

REFERENCES: 83

Figures list

Figure 1. Uranium-238 decay chain……………………………………………………………7
Figure 2. Thorium-232 decay chain……………………………………………………………8
Figure 3. Three major types of photon interaction with matter…………………………….…….9
Figure 4. Rayleigh scattering…………………………………………………………………… 9
Figure 5. Depiction of photoelectric effect in a free atom……………………………………. 10
Figure 6. Compton scattering... ………………………11
Figure 7. Pair production process………………………………………….......................... .12
Figure 8. A simplified decay scheme of ^{60}Co……………………………………………...15
Figure 9. A simplified decay scheme of ^{88}Y………………..…………………………….. 15
Figure 10. A diagram showing a typical insulator, semi-conductor and conductor with band gap Eg…………………………………………………………………………………………. 19
Figure 11. Diagram of different Planar, coaxial and well configurations of HPGe detector used in γ spectrometry…………………………………………………………………………….. 20
Figure 12. Block diagram of a gamma-ray spectrometer………………………...……….…. 22
Figure 13. Schematic representation of XRF……………………………………………... 25
Figure 14. X ray fluorescence process………………………………………………….. 25
Figure 15. Schematic working principle of WDXRF system……………………………….. 26
Figure 16. Deriving Bragg's Law using the reflection geometry and applying trigonometry.. 27
Figure 17. The configuration measurement used in this study……………………………..... 35
Figure 18. Simulated HPGe detector with cylindrical geometry and shield by MCNP5…… 41
Figure 19. X-ray fluorescence spectrometer....……………………………………………....... 43
Figure 20. Gamma spectrum of ^{152}Eu measured during 10000 s………………….………… 46
Figure 21. Calibration line………......……………………………………………………….. 46
Figure 22. Experimental efficiency of the detector for multi-gamma source mixed in plant Matrix……………………………………………………………………………………….. 47
Figure 23. Experimental efficiency of the detector for multi-gamma source mixed in soil matrix………………………………………………………………………………………… 48
Figure 24. Simulated and Experimental Spectrums for the mixed standard solution in a cylindrical plant matrix……………………………………………………………………… 55
Figure 25. Experimental and simulated Efficiency curves for the plant matrix in a cylindrical geometry…………………………………………………………………...…………... 55
Figure 26. Experimental and simulated Efficiency curves for the soil matrix in a cylindrical geometry…………………………………………………………………………….……….. 56
Figure 27. Simulated Efficiency curves for different soil densities…………………….……… 56
Figure 28. Variation of the self - absorption correction factor on the sample density (g/cm^{3}).57
Figure 29. Variation of the self-absorption correction factor for soil and plant matrices according to reference sample calculated by the MCNP5……………………………….... 57
Figure 30. Some crop samples with their corresponding soils…………………………...…. 66
Figure 31. Transfer factor of artichoke, mustard and fennel samples……………………….. 70
Figure 32. Soil-to-plant transfer factor negatively correlated with activity concentration of ^{226}Ra in soil…………………………………………………………………………... 73
Figure 33. Soil-to-plant transfer factor negatively correlated with activity concentration of ^{232}Th in soil……………………………………….………………………………… 74
Figure 34. Soil-to-plant transfer factor negatively correlated with activity concentration of ^{40}K in soil…………………………………………………………………………………… 74
Figure 35. Fallout radionuclides (137Cs, 7Be, and 210Pbex) Origin used as soil tracers in erosion and sedimentation studies……………………………………………………… 78

List of tables

Table 1. Surface cards Library used in MCNP code…………………………………….……32

Table 2. Types of tallies available in MCNP………………………………..…………..… 34

Table 3. Channel numbers corresponding to the gamma energies of the 152Eu source spectrum………………………………………………………………………………..….. 36

Table 4. The used radionuclides activities…………………………………………..….. 38

Table 5. Elements present in soil for MCNP Materials Card analyzed by WD-XRF………. 43

Table 6. Elements present in plant for MCNP Materials Card analyzed by WD-XRF……... 49

Table 7. Excitation conditions…..…………………………………………………….... 49

Table 8. Comparison of the simulated to experimental FEPEs for a cylindrical geometry in soil and plant matrices…………………………………………………………...………. 50

Table 9. Concentration of elements in soil samples using XRF technique…………………. 59

Table 10. Concentration of elements in plant samples using XRF technique………………. 60

Table 11. ^{226}Ra, ^{232}Th and ^{40}Kactivity concentrations, Radium equivalent ($Raeq$),Dγ, $Hint$, AEDE, and AGDE for crops samples……………..……………………………………… 69
Table 12. ^{226}Ra, ^{232}Th, and ^{40}K activity concentrations, Radium equivalent ($Raeq$),Dγ, $Hint$, AEDE, and AGDE for soil samples……………………...………………………………. 69
Table 13. Transfer of heavy metals…………………………………………………….…73
Table 14. ^{137}Cs activity concentration in the studied soil samples……....…………………..79

General introduction

Understanding the behavior of radioactivity, its intensity, and its impact on Earth is crucial. A constant radioactive background of the planet is created by the natural atmospheric radioactivity caused by cosmic radiation and radioactive gases discharged from the ground surface. The environment contains both radionuclides with anthropogenic origins and naturally occurring radioisotopes [1]. The man-made activities are another source of contaminant radioactivity, related to the nuclear power exploitation, accidents in the nuclear power stations like Chernobyl accident 1986, nuclear weapons testing and radioactive waste disposal [2]. Large portions of natural ecosystems, including plant, fruit, and vegetable areas, were affected or even damaged as a result of the radionuclides deposition and then can transferred into human body. Therefore, the precise assessment of radionuclides activities, their distribution and their transfer from soils to different plants and crops are of high importance in environmental radiation monitoring program and becomes the main topic of numerous researches [3-6]. Gamma spectrometry technique is one of the outstanding techniques that allows the identification and quantification of the radionuclides. Among its advantages is that its ability to provide absolute determination of isotopes directly, it is also nondestructive and it has best performance in terms of reliability of the measurements in radioactivity analysis [7-10]. The quantification of radionuclides requires a prior construction of full energy peak efficiency curve for a given large sample geometry, taking into account gamma self-absorption and coincidence summing effect corrections. High purity germanium detector (HPGe) is commonly used for gamma spectrometry measurements due to its high relative efficiency and its ability to detect the low radioactivity levels in environmental samples [11,12]. The measurements can be affected using either a source standard or a reference mixed γ-source.

However, since the standards are pricey and not always available to do the quantification analysis for different geometries and different matrices in the laboratory [7,13], and also because of the lack of high precision results due to the accumulation of gamma ray errors caused by the environmental radionuclides such as ^{40}K and decay products in the ^{238}U and ^{232}Th chains. To address these limitations, a robust and powerful simulation MCNP (Monte Carlo N-Particle) code has been developed by Los Alamos National Laboratory. This code based on Monte Carlo (MC) method which is useful for accurately modeling complex physical and analytical problems and also to complement the experimental calibration procedures such as the detector calibration problems used in the gamma spectrometry measurement systems. Likewise, MCNP has been proven to be highly effective for correcting self-absorption and summing coincidence effects resulting from the experimental measurements. For this purpose, we use the MCNP5

(Monte-Carlo N-Particle) simulation code to develop a detailed model composed of a HPGe semiconductor detector with a cylindrical geometry for plant and soil matrices. The developed model is validated with the aid of the experimental measurements using the mixed standard solution. The model will be applied for the correction of self-absorption and summing coincidence effects for the both soil and plant matrices. Those corrections allow to accurately determine the specific activities for the studied samples and therefore to precisely determine the soil to plant transfer factors (TFs).

The understanding of the transfer mechanism of radionuclides and heavy metals from soil to plants/crops and the availability of data on phosphate fertilizer usage in farmlands are still limited in many developing countries [14], including Algeria.

Consequently, we aim to provide a baseline data and enlarge the information about radioactivity in soil and crops as well as the soil-plant transfer of heavy metals within agricultural areas in Algeria that are not available yet. To address this knowledge gap, the potential of X-ray fluorescence (XRF) technique will be utilized to determine the presence of those heavy metals. This research will contribute to a comprehensive understanding of the dynamics of radionuclide and heavy metals transfer in the soil-plant system, which is critical for assessing potential radiological risks associated with soil and crop contamination.

The first chapter is divided into three parts. The first part provides an overview of the theoretical concepts related to natural radioactivity, including the emission of gamma rays, interactions between gamma rays and matter, the detection system used for gamma ray measurements, the detectors employed. The second part explores nuclear techniques, specifically focusing on Gamma Spectrometry technique with the detection setup and calibration. It also covers the x-ray fluorescence (XRF) technique, detailing the working principles of energy-dispersive XRF (EDXRF) and wavelength-dispersive XRF (WDXRF), along with quantitative spectrum analysis. In the third part, the chapter transitions to Monte Carlo simulation. It begins with a brief description of Monte Carlo methods, highlighting their use of random sampling to solve complex problems. It further discusses the principles of Monte Carlo simulations, emphasizing the role of random number generators and the concept of "radiation transport" for particles. Following this, the chapter delves into popular Monte Carlo codes used in nuclear physics, such as GEANT4, FLUKA, EGSnrc, PENELOPE, and MCNP (Monte Carlo N-Particle) codes. The final section of the chapter focuses on the MCNP code, presenting detailed insights into its input file.

The second chapter shows the experimental setup used in the laboratory for the measurements, which includes detailed data of the High Purity Germanium (HPGe) detector with its associated electronics. The energy calibration is carried out using ^{152}Eu point source, ensuring accurate measurement of energy values. The efficiency calibration is performed using standard solution to determine the detection efficiency of the HPGe detector for different energies ranging from 59.54 keV to 1836.12 keV. Additionally, the chapter presents a Monte Carlo source-detector model with its all-necessary data needed to simulate the experimental measurements. The X-Ray Fluorescence (XRF) and Wavelength Dispersive X-Ray Fluorescence (WD-XRF) techniques, are also discussed in this chapter, highlighting their contribution in this research.

The third chapter encompasses the results and discussion of the work. Firstly, it entails the validation of the Monte Carlo model developed in the previous chapter, ensuring its reliability in simulating the experimental measurements. The determination of self-absorption and summing coincidence correction factors using the developed model is also discussed. Furthermore, the effect of soil sample density on gamma energy efficiencies is investigated using the MCNP5 model with the interpretation of the findings. Additionally, the chapter lists the XRF results for soil and crop samples with a comprehensive analysis and compare them with standard limits.

The last chapter delves into the environmental application soil-to-plant transfer factors, shedding light on the mobility of environmental radionuclides in the soil. The determination of specific activities in crops with their soil samples are carried out to quantify the transfer of radionuclides from soil to crops. The transfer of the radionuclides ^{226}Ra, ^{232}Th an ^{40}K will be determined as well as the transfer of heavy metals and trace elements of Cu, Mn, Ni, Zn, Co, V, S, Mo and Sr. The radiation hazard indices like the radium equivalent activity (Ra_{eq}), the internal hazard index H_{int}, The absorbed dose rate ($D\gamma$) in air at 1 m above the ground, the annual effective dose equivalent (AEDE), and the annual gonadal dose equivalent (AGDE) parameters will also be estimated in this chapter and compared with the worldwide standard. The chapter also discusses the variation of transfer factors in function of the activity concentrations of radionuclides in soil, providing insights into the factors influencing the transfer of radionuclides from soil to crops.

A general conclusion will be drawn at the end of the manuscript, providing valuable insights for environmental risk assessment and management strategies related to radionuclide and heavy metals contamination in agricultural ecosystems.

Chapter I: Background theory

I.1 Radioactivity and its sources

The radioactivity is a spontaneously decay of an unstable parent element to a daughter element by emitting energy in the form of radiation. This can occur naturally or artificially. There are three types of radiation emitted during the radioactive decay: alpha particles, beta particles, and gamma rays. Alpha decay occurs when a nucleus emits an alpha particle, which consists of two protons and two neutrons. Beta decay occurs when a neutron in the nucleus decays into a proton an electron and anti-neutrino. Gamma decay occurs when the nucleus emits high-energy gamma rays. Radioactive decay is described by the law of decay as the following [15]:

$$N(t) = N_0 e^{-\lambda t} \qquad (1)$$

Where N_0 is the number of nuclei present at time t= 0, is the radioactive decay constant and is the half-life of the radioisotope and it presents the rate of decay.

Since the activity is proportional to the number of radioactive atoms, it decreases exponentially with time as well:

$$A\ (t) = A_0 e^{-\lambda t} \ (2)$$

The activity A is the number of radioactive decays per unit time and it can be represented as

$$A = \lambda N \qquad (3)$$

The unit is Becquerel (Bq) in which 1 Bq = 1 decay per second, and it can be expressed in Curie unit (Ci) where: 1 $Ci = 3.7 \times 10^{10}$ decays per second.

1.1 Natural radioactivity

Natural radioactivity occurs as a result of the decay of radioactive elements found in the earth's crust. It comes from three natural radioactive families ^{232}Th, ^{235}U and ^{238}U. During this process, they emit alpha, beta, and gamma particles, which can be detected using radiation detectors. Cosmic radiation is another natural source of radioactivity. It consists of high-energy particles that originate from outer space and penetrate the earth's atmosphere, creating nuclear reactions with the atmosphere atoms and generates radioactive isotopes mainly ^{3}H, ^{14}C, ^{7}Be and ^{22}Na [16].

1.2 Artificial radioactivity

Man-made or artificial radioactivity refers to the creation of radioactive isotopes through human activities, including nuclear reactions, nuclear weapons testing, and nuclear power generation. In nuclear reactions, scientists can artificially create radioactive isotopes by bombarding stable atoms with high-energy particles such as neutrons. This can change the number of protons and neutrons in the nucleus, leading to the creation of new isotopes that may be radioactive. Nuclear weapons testing also produces artificial radioactivity. During a nuclear explosion, atoms are split apart, and new isotopes are created, some of which are radioactive. These radioactive isotopes can contaminate the surrounding environment and persist for many years. Nuclear power generation produces artificial radioactivity in the form of nuclear waste. Nuclear reactors use uranium or plutonium to generate energy, and during the process, radioactive isotopes are created. The spent fuel from nuclear reactors contains a variety of radioactive isotopes, some of which can remain radioactive for thousands of years. Proper storage and disposal of nuclear waste are important to prevent long-term health and environmental hazards. Other man-made activities are industrial applications include the use of radioactive isotopes in manufacturing, research, and agriculture [17].

1.3 Radioactive decay chain

In many cases of radioactive decay, the daughter nuclide formed by the decay of the parent is also radioactive. This situation is commonly referred to as a "radioactive decay chain" or "radioactive progeny series. As a result, the decay of the daughter nuclide is characterized by its own decay constant as the following [18]:

$$X_1 \overset{\lambda_1}{\to} X_2 \overset{\lambda_2}{\to} X_3 \overset{\lambda_3}{\to} \cdots Xn \overset{\lambda_n}{\to} stable$$

The starting nuclide X_1 is called the parent and the others are called the first, second, … daughter nuclides.

The evolution of the populations of parent nuclei and their daughter nuclei can be described by the following differential equation [18]:

$$\frac{dN_i}{dt} = \lambda_{i-1}N_{i-1} - \lambda_i N_i \qquad (4)$$

1.4 Radioactive families

The radioactive family is a group of radionuclides that undergo a series of radioactive decay to reach a stable state. Each decay in the series results a new isotope that is also radioactive, and this process continues until reaching a stable isotope. There are several radioactive families or decay series, including the uranium series, the thorium series, and the actinium series. The abundance of uranium ^{238}U (4n+1) constitutes 99.28% of natural uranium. It decays until reach to stable lead ^{206}Pb (Figure 1). This process includes 14 intermediate isotopes and the most well-known intermediate isotopes in the uranium series include radium-226 (^{226}Ra) and radon-222 (^{222}Rn), both of them emit alpha particles and gamma rays. The ^{232}Th (4n) series starts with ^{232}Th and ends with stable lead-208 (^{208}Pb). Its abundance constitutes all-natural thorium. During the decay, 6 α and 4 β particles are emitted and about 36% of the ^{212}Bi decay produces ^{208}Tl by α emission (Figure 2).

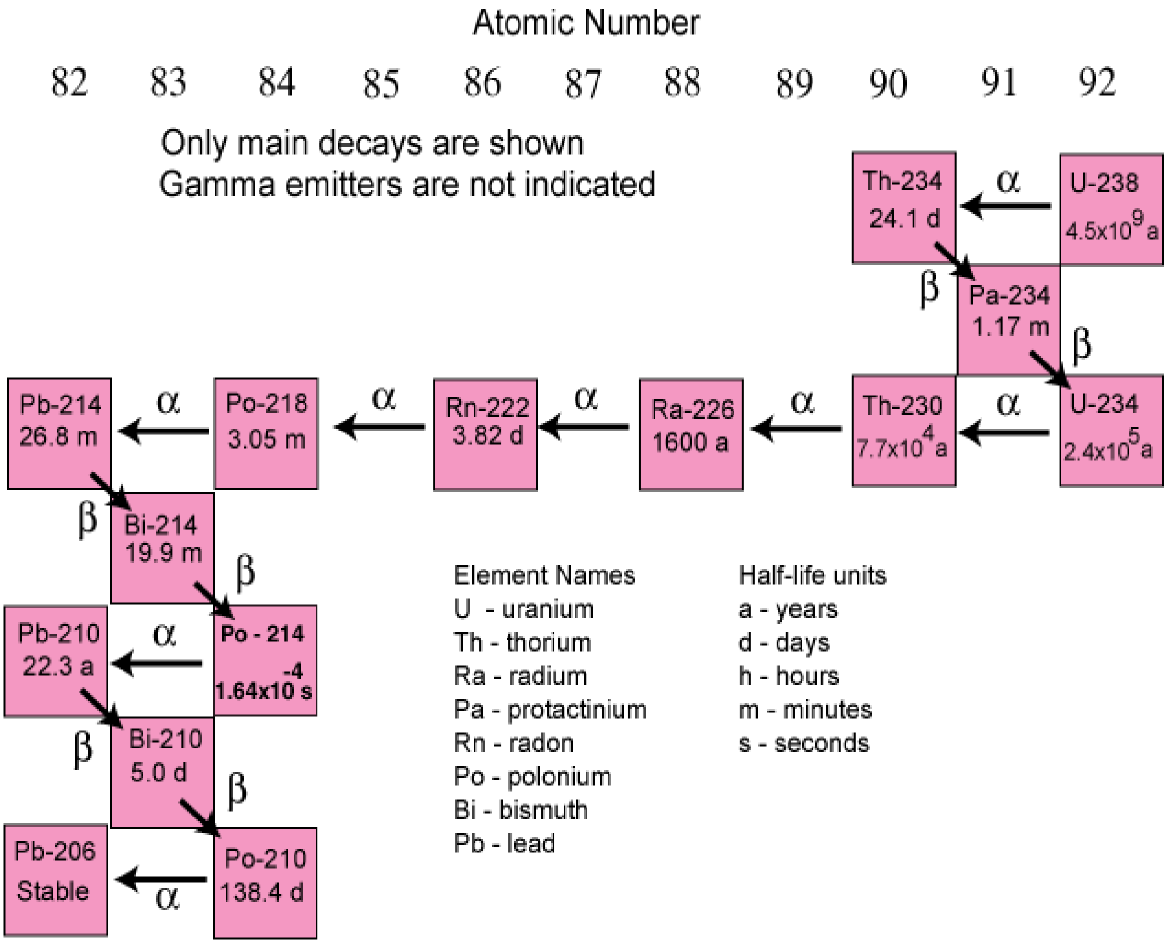

Figure 1. Uranium-238 decay chain

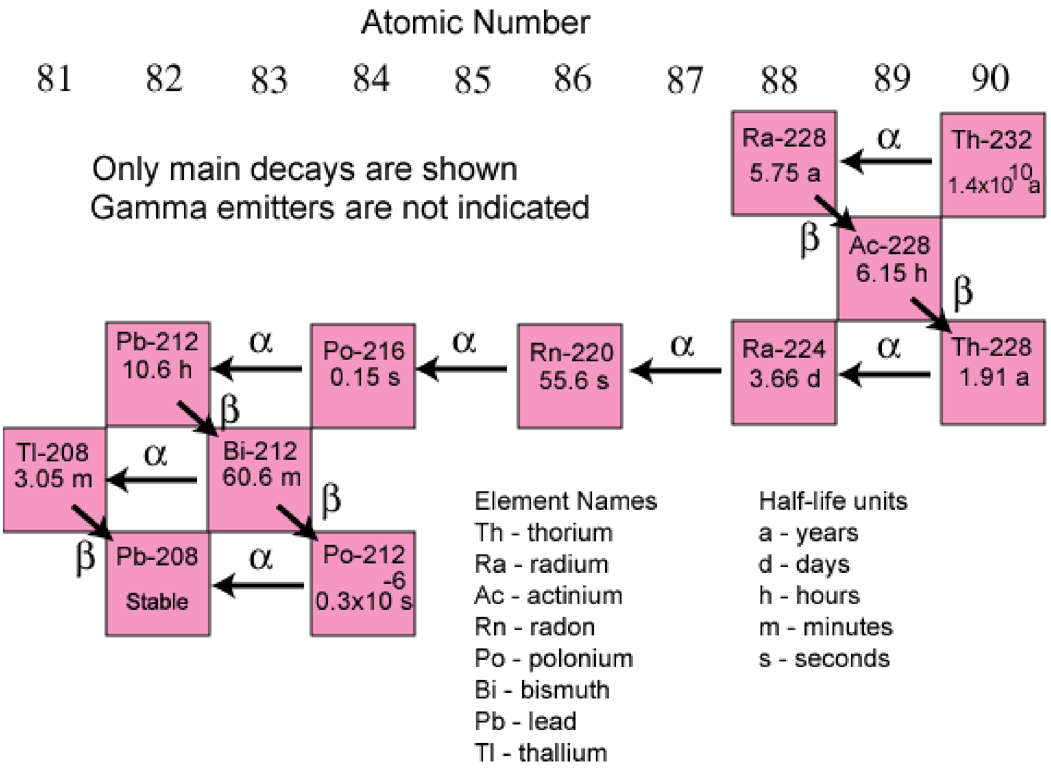

Figure 2. Thorium-232 decay chain

1.5 Secular equilibrium

The secular equilibrium is the steady state occurs when all daughter nuclides have the same decay activity as the parent. At that state, all the daughter nuclides in the ^{238}U, ^{235}U and ^{232}Th decay series have the ratio of activity that is equal to one. The secular equilibrium occurs when:

$$\lambda_A N_A = \lambda_B N_B \qquad (5)$$

Where *A* is the parent radionuclide decaying into daughter radionuclide *B.*

The secular equilibrium is achieved when the half-life of the parent nuclide is much longer than that of its daughter products.

1.6 Gamma Ray Interaction with Matter

When gamma rays penetrating matter, they can interact with the atoms through various processes either with the atomic electrons or the nuclei under three main interactions:

the dominating photoelectric effect at low energy, Compton scattering at intermediate energies, and pair production at high energy (Figure 3). The probability of these events depends on the energy of the photon. In all cases, free electrons are generated, creating ion-electron or electron-hole pairs. The following subsections discuss the three major processes [16, 19]:

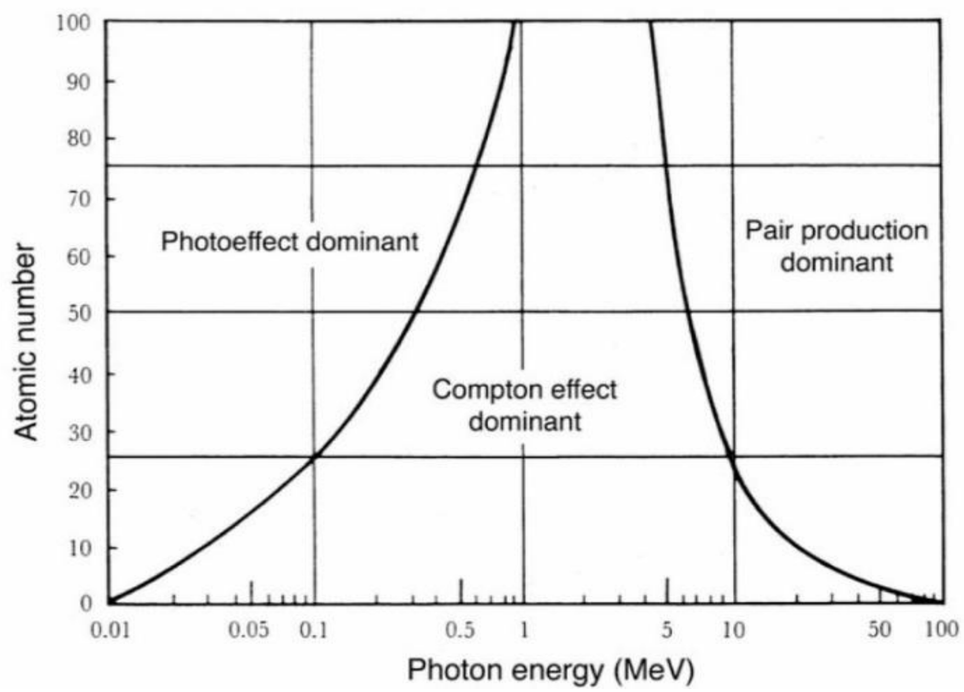

Figure 3. Three major types of photon interaction with matter

A. Rayleigh scattering

Coherent Rayleigh scattering is a phenomenon that occurs when an incident photon interacts with a bound atomic electron in a material, resulting in elastic scattering of the photon without exciting the atom or losing energy in the process. It occurs mainly at small scattering angles, at low energies, and for high Z elements, and does not involve excitation or ionization of the atom (Figure 4).

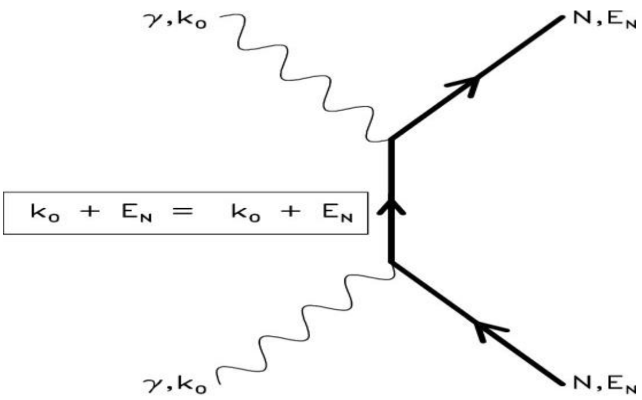

Figure 4. Rayleigh scattering

B. Photoelectric effect

In photoelectric process, an atomic electron absorbs all of gamma ray energy (See Figure 5). The electron is ejected from the atom with a kinetic energy E equal to [17]:

$$E = hv - E_b \qquad (6)$$

Where hv is the incident photon energy.

E_b is the binding energy.

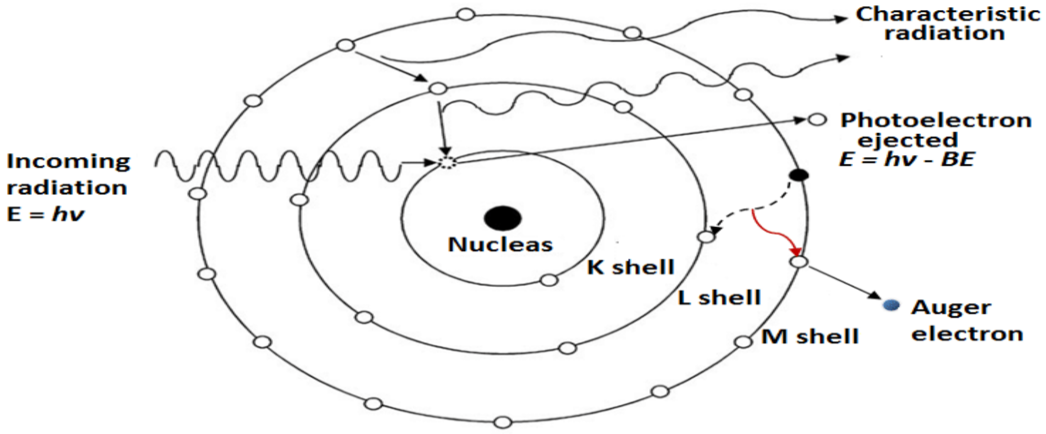

Figure 5. Depiction of photoelectric effect in a free atom

Since the ejected electron leaves a hole in a shell of the atom. This recovers the equilibrium through the emission of one or more X-ray or Auger electron.

The interaction cross section τ is a probability of a photon undergoing photoelectric absorption, which depends on the atomic number Z of the material and the photon energy hv is described by [17]:

$$\tau = \text{constant.}\tan\frac{Z^4}{(hv)^3} \qquad (7)$$

Where Z is atomic number of the photoelectric absorber.

A high Z material with low photon energy is very effective in the absorption of the photon. This explains why this effect is the dominant mode of interaction at low gamma energies and becomes negligible at high energies.

C. Compton scattering

In Compton scattering process, an incident photon undergoes a collision with an electron and transferring a portion of its energy to the electron (see Figure 6). From the conservation of energy and momentum, the photon is scattered with a new energy hv', and the electron recoils at an angle Ψ. The scattered photon energy is given by [16]:

$$hv' = \frac{hv}{1+\alpha(1-cos\theta)} \qquad (8)$$

where is $\alpha = \frac{hv}{m_0c^2}$, m_0c^2 the energy corresponding to the rest mass of electron (511 keV). hv' is the scattered gamma-ray energy.

The two angles are related by:

$$tan\Psi = \frac{1}{(1+\alpha)tan\frac{\theta}{2}} \qquad (9)$$

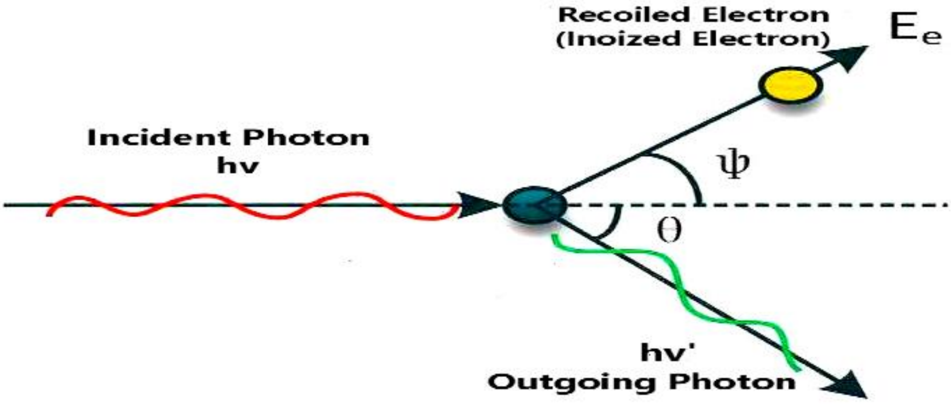

Figure 6. Compton scattering

The cross section of Compton scattering for the photon scattered through any angle θ on free electrons is described by the analytical Nishina–Klein formula:

$$\frac{d\sigma}{d\Omega}(\alpha,\theta)=\frac{r_0^2}{2}\left(\frac{hv'}{hv}\right)^2\left(\frac{hv}{hv'}+\frac{hv'}{hv}-sin^2\theta\right) \qquad (10)$$

D. Pair production

When the energy of the incident photon is greater than twice the energy corresponding to the rest mass of the electron (i.e., 1.022 MeV), the effect of pair production becomes important (Figure 7). The process takes place within the Coulomb field of the nucleus, resulting in the conversion of the photon energy into an electron–positron pair [16].

$$hv = 2m_eC^2 + T_- + T_+ \qquad (11)$$

where m_eC^2=0.511 MeV and m_e is the mass of an electron.

$T_- and\ T_+$ are the kinetic energy of the electron and the positron, respectively.

Both the electron and positron particles will be slowed down in the material and the positron will eventually react with an electron and annihilates. As a result of the interaction, two annihilation -rays are generally produced.

The estimation of pair production cross section shows that it varies by Z^2 [17, 20]:

$$\sigma \propto Z^2 f(Z, hv) \quad (12)$$

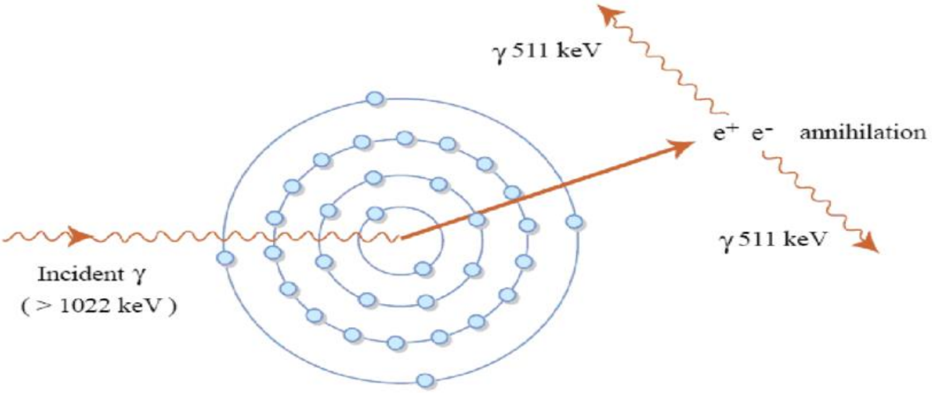

Figure 7. Pair production process

1.7 Photon beam attenuation

If a monoenergetic beam of photons pass through a thin layer of a material, a number of them will be attenuated which means being absorbed or scattered in the layer. The attenuation effect is such a complicated process which could only be determined by Monte Carlo calculation [15]. The total cross section for a photon is given by the equation [15]:

$$\sigma_T = \sigma_\tau + \sigma_c + \sigma_k +$$

The attenuation of gamma radiation can be then described by the following equation [21]:

$$I = I_0 e^{-\mu x} \qquad (14)$$

where, I_0 is the incident intensity and μ is the total absorption coefficient. The attenuation coefficient depends on the density of the absorber, the atomic number Z and photon energy. The gamma ray results from the different interactions within the detector mentioned above should be detected in order to register the presence of the gamma ray and measure its energy. The ionized electrons collide with other atoms and liberate many more electrons. The liberated charge is collected, either directly (as with a proportional counter or a solid-state semiconductor detector) or indirectly (as with a scintillation detector). The final result is an electrical pulse whose voltage is proportional to the energy deposited in the detecting medium.

1.8 Self-absorption effect

During the detection process of gamma rays emitted by the natural radionuclides, a portion of gamma rays is lost due to the self-absorption effect. This loss alters the full energy peak value [55,56] and thus the radionuclides activity will change. This process of self-absorption depends on the matrix composition, sample density and the energy of the gamma radiation [54,55]. Several studies on gamma spectrometry have taken self-absorption correction into account [33-37]. The theoretical correction method developed by Appleby et al. [57] consists in calculating the relative correction coefficient using the attenuation factors. It represents the ratio of the attenuation factor from a photon in the standard to that of the sample. This method requires knowledge of the linear attenuation coefficient of the samples measured. A general analytical function established by Barba et al [37] for calculating the mass attenuation coefficients of samples whose compositions are known such as NORM (Naturally Occurring Radioactive Materials) to correct self-absorption effects in samples measured by gamma spectrometry. Otherwise, various experimental correction methods were discussed in terms of their approaches and limitations. Overwater et al. (1993) approached the correction for voluminous sample. The correction factor was defined by the ratio of the calculated point source photopeak efficiency to the photopeak efficiency of the voluminous sample source. A Monte Carlo calculation was applied to determine the photopeak efficiency and performed by a single photon through the complete source-detector system [58].

This type of correction is more significant at lower gamma energies (≤ 100 keV) and high sample density (has a high atomic number) because more radiation is likely to be absorbed by the material. In this section, we will focus on the contribution of the chemical composition and the density in the counting losses for energies below 150 keV.

1.9 Coincidence summing effect

True coincidence summing occurs when radionuclides emit two or more cascading photons within the resolving time of a detector. It becomes more important at short source-to-detector distances (solid angle is large) and without correction of such an effect, the activity of radionuclides cannot be accurately determined. The correction process can be performed using different methods, depending on the type of gamma-ray detector and the experimental setup. The corrections could be estimated experimentally using a variety of techniques, the most commonly used experimental methods are based on the use of multiple gamma-ray detectors, as well as careful selection of gamma-ray energies and source-detector geometries [59-64]. By comparing the spectra from different detectors, it is possible to identify and correct for coincidence summing effects and measuring the same gamma-ray energy with two different detectors to apply the correction factor. The correction can also be performed using a mathematical approach, that takes into account the probability of two or more gamma-rays interacting in the detector at the same time, and the correction factor is determined using Monte Carlo simulations. The approach consisted of creating a simulation source- detector model in which the simulation takes into account the probability of two or more gamma rays being detected simultaneously and produces an output spectrum that is corrected for coincidence summing effect. Thus, the Monte Carlo simulation approach is more flexible and can be used to model more complex detector geometries and materials [59].

when ^{60}Co undergoes a beta decay, it transforms into ^{60}Ni, often in an excited state. The excited ^{60}Ni is then transitioned to its ground state by emitting two gamma rays in a cascade. These gamma rays have energies of 1173.2 and 1332.5 keV, and are emitted in rapid succession (see Figure 8).

The ^{88}Y also undergoes a beta decay and transforms to an excited ^{88}Sr. The deexcited process is characterized by the cascading emission of two prominent gamma rays with energies of 898.04 keV and 1836.07 keV and other weaker gamma rays (see Figure 9).

In this work, the measured efficiencies were corrected for the coincidence summation effect to improve the accuracies of the efficiencies results, using a simulated MCNP5 model for an HPGe detector with a cylindrical container. The efficiency values of the two radionuclides ^{60}Co and

^{88}Y in both plant and soil matrices have been corrected through the report of experimental and simulated FEPEs (Table 8 in chapter 4).

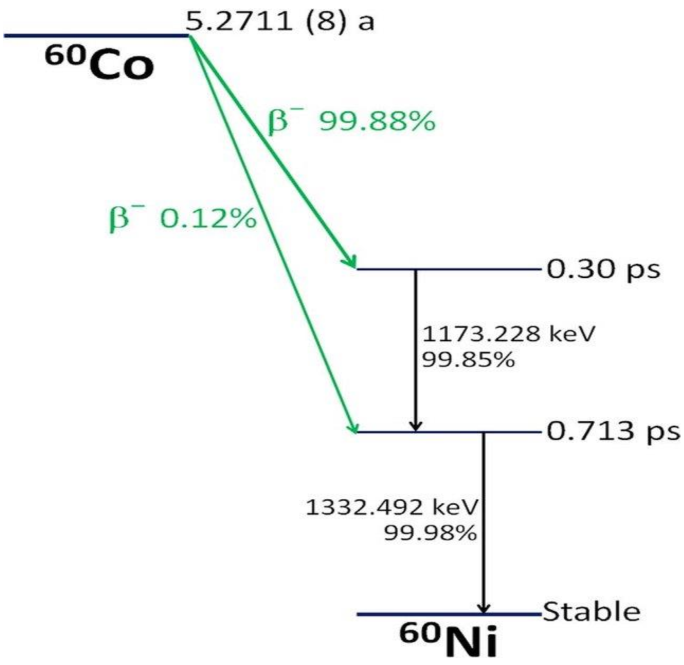

Figure 8. A simplified decay scheme of ^{60}Co

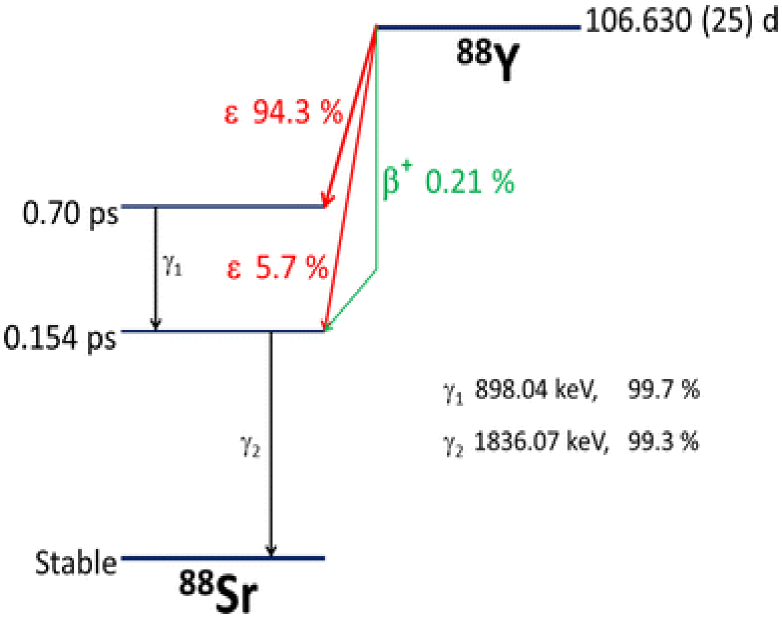

Figure 9. A simplified decay scheme of ^{88}Y.

1.10 Interaction of electrons with matter

As we have addressed previously, the interactions of photons with matter a movement of electrons which they can interact with the material. The interaction occurs in different ways [21]:

A. Ionization process

If an incident electron provides enough energy to an atom, it may eject one of its bound electrons, resulting in the ionization of the atom. The energy of the ejected electron depends on its binding energy and the energy of the incident electron. Thus, the process is an inelastic collision mechanism of an electron or positron. The energy loss per collision is given by the Bethe formula, which describes the energy loss rate for charged particles. [21]:

$$-(\frac{dE}{dX})_{coll} = \frac{2\pi e^4 NZ}{m_e C^2 \beta^2} (Ln \left(\frac{m_e C^2 \beta^2 E}{2I(1-\beta^2)}\right) - Ln(2)\left(2\sqrt{1-\beta^2} - 1 + \beta^2\right) + \frac{1}{8}(1 - \sqrt{1-\beta^2})^2) \quad (15)$$

Where c is the celerity of light, $\beta = \frac{V}{c}$ is the reduced speed, and I is the mean potential depends on the material nature.

B. Bremsstrahlung radiation

Bremsstrahlung is a process in which decelerating charged particles emit electromagnetic radiation. All charged particles can emit this kind of radiation provided they have enough energy [21].

Therefore, can be accelerated by the Coulomb field of the atom because of its small mass, resulting a radiation energy in terms of photons. The electron undergoes a deceleration and transfers a part of its energy to the photons. This is the dominant energy loss process for high energy electrons (and positrons). The loss of linear energy by this interaction is written as the following [22]:

$$-(\frac{dE}{dX})_{Brem} = \frac{NEZ(Z+1)}{137 m_e C^2} (4Ln \left(\frac{2E}{m_e C^2} - \frac{4}{3}\right) \quad (16)$$

Bremsstrahlung depends on the strength of the electric field seen by the particle (usually the nuclear electric field) so screening due to atomic electrons needs to be accounted for. Cross-section is therefore dependent not only on the electron energy, but also on the impact parameter and the Z of the material.

C. Multiple coulomb interaction

Consider an electron traveling through a certain material and makes a "collision" with an electron from the material atoms while crossing its thickness, then it undergoes Coulomb scattering. This leads to a deviation of the electron track from its initial direction. If the number of collisions for each electron is sufficiently large, the angular distribution of the multiple Coulomb scattering follows a Gaussian law at small angles [22].

D. Positron interaction (Annihilation)

When an electron interacts with its antiparticle (positron), the result is the annihilation of both and the generation of photon. The positron behaves exactly like electron, having all its characteristics except for the polarity of its electrical charge, which in this case is attractive. When an electron-positron annihilation occurs, Different particles can be produced during this process depending on their energy. At low energies, only photons are produced, while at high energies other particles such as Z bosons can be produced. The annihilation process is accompanied by the emission of two 511 keV photons emitted at 180° in the laboratory reference frame [22].

1.11 Mean path of charged particle through matter

It represents the distance traveled by a heavy charged particle in a material until it dissipates all of its energy. This distance is directly related to the energy loss [21]:

$$R = \int_{E_0}^{0} (-\frac{dE}{dX})^{-1} dE \quad (17)$$

The trajectory of electrons in matter is erratic due to the multiple random interactions they undergo as they pass through matter. As a result, the actual distance traveled is much greater than the distance from the point of entry to the point of arrival (where the electron has lost all its energy). We then define the depth of penetration Rp which corresponds to the average maximum distance traveled by an electron.

1.12 Detectors

1) Semi-conductor detectors

In radiation measurement, semiconductor detectors are commonly used due to a variety of features, including excellent energy resolution, linearity over a wide range of energies, short pulse rise-time, simplicity, and the insensitivity to magnetic fields [15, 17]. Their principle is based on the semiconductor band theory, where electrons in the valence band are excited by ionization and cross the forbidden band to the conduction band. The transition of an electron from the valence band to the conduction band depends on the temperature and material gap (Figure 10). In the case of germanium, the gap is of the order of 0.67 eV [19, 20].

A. N-type semiconductors

If the crystal is doped with a pentavalent (having five valence electrons) impurity, the latter are added in the N-type semiconductor to increase the number of electrons for conduction.

B. P-type semiconductors

If the crystal is doped with a trivalent (having three valence electron) impurity, they will create number of holes, which can be filled by valence electrons from a nearby atoms, but this will create other holes that can be seen as a moving positive charge.

2) Scintillation Detectors

The active volume of a scintillation detector is a luminescent material (a solid, liquid, or gas) that can be detected by a gamma-ray-induced light emissions device like photomultiplier tube (PMT). The scintillation material can be organic or inorganic which is more common like sodium iodide (NaI), cesium iodide (CSI), zinc sulfide (ZnS), and lithium iodide (LiI). Inorganic crystals NaI and CSI solid scintillation are the most popular detectors. A new scintillation material, bismuth germanate (BiqGesOl 2), known as BGO becomes popular in applications where its high gamma counting efficiency and/or its lower neutron sensitivity outweigh considerations of energy resolution.

The scintillation detector spectroscopy system is consisted of a scintillation crystal of sodium iodide thallium activated, NaI (Tl) of various sizes, a photomultiplier, a series of nuclear electronic instruments, such as high voltage bias supply, a linear spectroscopic amplifier, a pulse counting unit which could be a single channel analyzer SCA or multichannel analyzer, MCA. The resulting multiplication of those electrons (or photo-electrons) produces in an electrical pulse which can then be analyzed and provide meaningful information about the particle that originally struck the scintillator [22].

3) HPGe detectors

In gamma spectrometry, HPGe crystals exist in three different types: planar, coaxial and reverse-coaxial. The use of each detector is lied to the type of sample or radionuclide. For example, Planar detectors whose maximum crystal thickness is about 3 cm, associated with a carbon entrance window, are used for the detection of low energy photons. These detectors are suitable for thin samples. However, for large volume samples, it is preferable to use coaxial detectors with a cylindrical shape. This type of detector has a beryllium or aluminum window.

If the sample quantity is in very small, it is desirable to measure it with a well detector. The well detectors have the same configuration as the coaxial detectors but unlike the latter, the central hole is used to receive the sample with a maximum volume of 5 cm^3. The entrance window is made of aluminum (See Figure 11) [23].

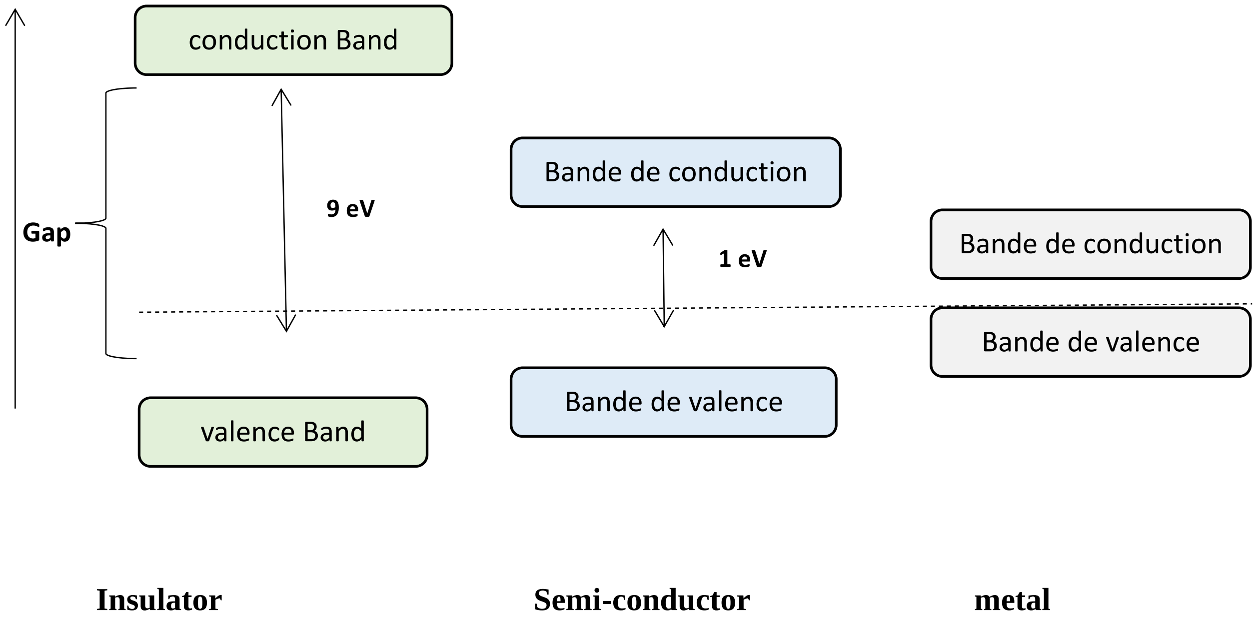

Figure 10. A diagram showing a typical insulator, semi-conductor and conductor with band gap E_g

1.13 Detector specifications

The main characteristics of a detector are: Energy resolution and Efficiency [21].

1) Energy resolution

The energy resolution of a detector is specified as the full width at half maximum (FWHM) of a spectral peak. It determines the ability of a detector to separate the spectral lines. It can be expressed as a percentage of the incident energy or in terms of energy measured in electron volts. The most fundamental factor affecting the resolution of semiconductor detector spectrometers is line broadening due to the statistical uncertainty.

2) Detection efficiency

Detection efficiency is decisive in the quantitative analysis of a sample and it directly affects the accuracy and reliability of the results obtained from a sample. It can be subdivided into two classes: absolute and intrinsic.

The intrinsic efficiency presents the probability that a detector will respond to a particular type of radiation or signal, considering only the interaction of the radiation or signal with the detector material itself. It is the ability of the detector to change energy of the radiation into a useful signal and it is expressed as the ratio of net count rate to the absolute activity of a radionuclide. It is defined as [21]:

$$\varepsilon_{\text{int}}=\frac{\text{number of pulses recorded}}{\text{number of radiation incident on detector}} \tag{18}$$

The absolute efficiencies are defined as [21]:

$$\varepsilon_{\text{abs}}=\frac{\text{number of pulses recorded}}{\text{number of radiation emitted by source}} \tag{19}$$

The absolute efficiencies take account several factors that may affect the detection process such as geometrical efficiency, self-absorption, detector response and electronics, and the energy and type of radiation or signal being detected.

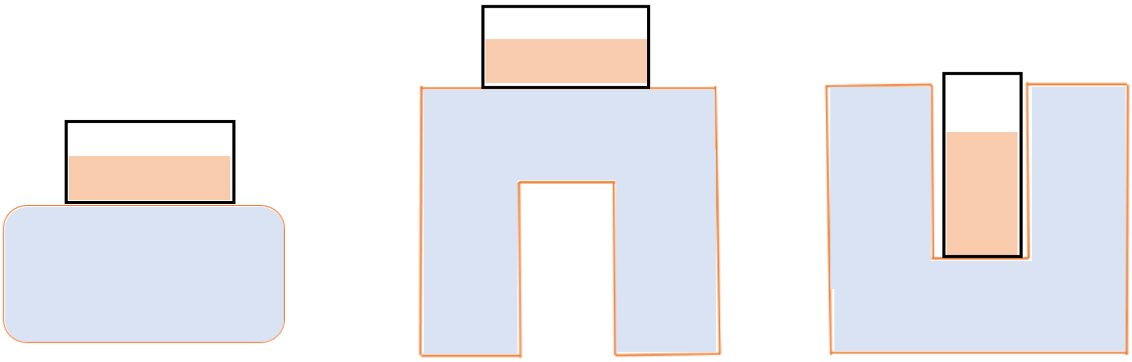

Figure 11. Diagram of different Planar, coaxial and well configurations of HPGe detector used in γ spectrometry.

I.2 Nuclear techniques

2.1 Gamma Spectrometry technique

The determination of the activity concentration for each radionuclide is performed using gamma spectrometry technique which provides a direct identification and quantification with high precision of the measurements. It is non-destructive method, quick and does not require extensive pretreatment steps and chemical separation in radioactivity analysis. The quantification of radionuclides demands prior construction of full energy peak efficiency curve for a given sample geometry [3,10].

Various detector types are used to measure γ-rays. The one used in our laboratory is High Purity Germanium detector (HPGe) which is commonly used for gamma spectrometry measurements due to its high resolution and its ability to estimate the low radioactivity levels in environmental samples [11,12]. Before any gamma-ray emission measurements can be performed, energy and efficiency calibration must be carried out. The latter can be affected experimentally by standard source using either a source “standard” or “reference mixed γ-source”, in which the activity for the whole source is quoted by the supplier [15].

2.1.1 Detection setup

The measurement chain is typically consisting of a detector (whose sensitive part is a germanium crystal) which is the component that detects the gamma rays emitted by the source and converts them into electrical signals, a preamplifier, an amplifier that amplify the electrical signals from the detector, an analog-to-digital converter (ADC), a multi-channel analyzer (MCA) which records the number of signals at each energy level and produces a spectrum that shows the energy distribution of the gamma rays, and analysis software used to control the electronics and analyze the data collected by the MCA. It allows the user to adjust the settings of the instrument like the time of measurement. The analysis software can also be used to identify the radionuclides present in the sample by comparing the measured spectrum with a library of known spectra. This acquisition setup allows to measure a signal resulting from the interaction of radiation with the germanium crystal, to amplify it and to shape it for subsequent analysis [19] (Figure 12).

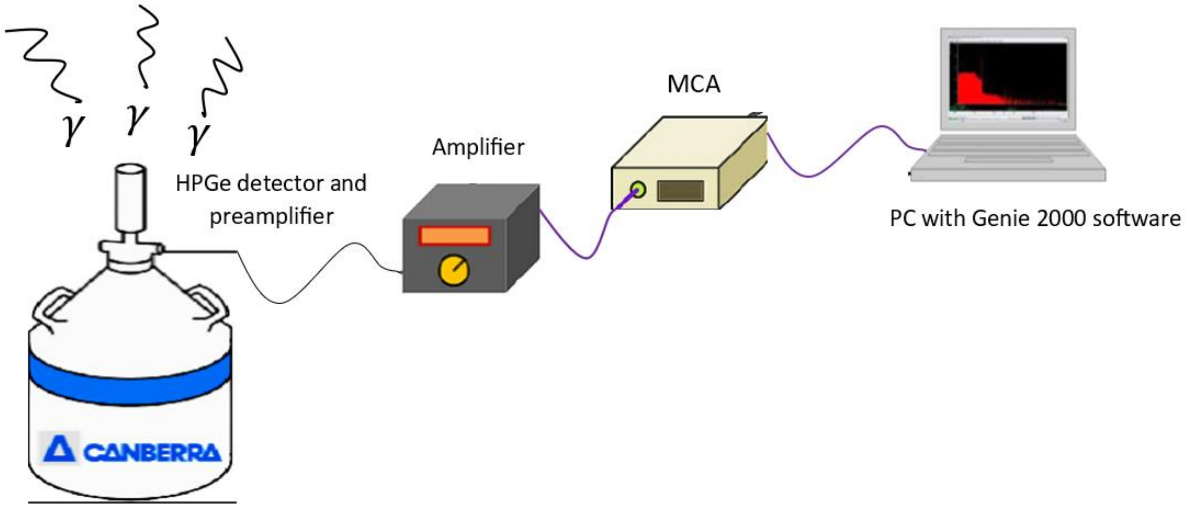

Figure 12. Block diagram of a gamma-ray spectrometer

2.1.2 Spectrum analysis

In gamma-ray spectrometry, it is necessary to calibrate the pulse height scale in terms of absolute energy in keV using standard sources whose activity is determined by direct measurement to identify and quantify unknown gamma-ray emitters. The analysis is based on the study of the total absorption peaks observed in the recorded spectrum. Two steps prior to any measurement are essential: energy calibration for qualitative analyzes and efficiency calibration for quantitative analyses [22]**.**

1) Energy calibration

The energy calibration of a γ spectrometer is accomplished by measuring the spectrum of a source emitting gamma radiation of known energy. The obtained spectra correspond to the energy lines of this source. The total absorption lines are classified by their amplitudes. Each channel is associated with an energy. Equation 18 is used in the energy calibration to determine the relationship between the channel number of the pulse height spectrum and the energy of the photon radiation. It is sufficient to measure the spectrum long enough to achieve good statistical precision for the peaks to be used for the calibration [23]:

$$E_j(keV) = A_0 + A_1 C_j + A_2 C_j^2 \qquad (20)$$

Where E_j is the energy, A_0 is the offset, and C_j are coefficients to be determined and C is the channel number. The more available calibration points, the more accurate energy calibration.

2) Efficiency calibration

The efficiency calibration is required to determine the detection efficiency of the detector as function of energy. To establish an effective calibration, one must use standard sources which are of nature and form similar to those of the sample to be analyzed. An energy curve is obtained for a given geometry and matrix. From this curve, the detection efficiencies of the different peaks showed the spectrum are exploited for the calculation of the activity according to the following equation [23]:

$$\varepsilon = \frac{N_{net}}{A \times t_c \times I\gamma} \qquad (21)$$

Where A is the activity of each gamma energy, N is the net area at the interest peak energy corrected for background counts I_γ is the γ-ray emission probability and t_c is the counting time

2.1.3 Background noise

There are several sources of background noise in HPGe detectors used in gamma spectrometry. One of the main sources is the naturally occurring background radiation, which includes gamma rays from the environment, such as from terrestrial and cosmic radiation, as well as from radioactive isotopes present in the detector itself and its surrounding materials. Another source of background noise is electronic noise generated by the detector's readout electronics, which can introduce additional signals that may interfere with the gamma-ray signals of interest. Additionally, environmental factors such as temperature fluctuations, electromagnetic interference, and radioactive contaminants in the laboratory or measurement environment can also contribute to background noise in HPGe detectors. The presence of background noise can significantly impact the accuracy and sensitivity of gamma spectrometry measurements, as it can mask or interfere with the signals from the radioactive isotopes of interest, leading to reduced measurement precision and accuracy.

Reducing background noise in HPGe detectors for gamma spectrometry can be achieved through techniques such as shielding, active and passive shielding, optimizing electronics and signal processing, conducting background subtraction, implementing environmental controls, selecting low-background detectors, and optimizing measurement conditions. These methods aim to minimize unwanted signals from sources such as background radiation, electronic noise, and environmental factors [15, 21].

2.1.4 Detection limit

Due to stochastic variations in both the signal and the background noise, when detecting low activity levels, the measurement may converge on or even overlap with the background noise level. Establishing the detection limit, or the lowest activity level that can be accurately identified and measured with a particular level of confidence, becomes crucial in such circumstances. The threshold used to separate the signal from the background noise, such as one based on statistical considerations, is often used to calculate the detection limit [23].

2.2 X-Ray Fluorescence technique (XRF)

X-ray fluorescence is a non-destructive analysis method used to obtain qualitative and quantitative analysis of the elemental composition of materials. Excitation can be caused either by an X-ray beam or by bombardment with particles, usually electrons. The emitted X-rays are then measured using a detector, and the resulting spectrum is used to identify the elements present in the sample and determine their concentrations [39] (See Figure 13).

2.2.1 EDXRF (Energy Dispersive X-ray fluorescence) working principle

EDXRF spectrometry is an analytical technique that widely used for the routine determination of the major elements and trace elements in variety of sample types, including solids where uncertainties ranged from 0.2-0.4% and liquids. XRF is reliable enough to provide a high precision of analytical measurements until to ppm detection limit. in which it can analyze elements ranging from beryllium (Be) to uranium (U). When a sample is excited by a primary beam of X-rays. the interaction of X-ray photons with the sample atoms indices an ionization of inner shell orbital electrons by photo-electric effect. Thus, the atom becomes unstable and immediately decays to a more stable electronic configuration by transition of an outer shell electron to fill the vacancy caused by ionisation. The excess energy results from electron falls are emitted as a secondary "fluorescence" X-ray photon having a discrete energy corresponding to the difference in energy between the two orbital levels involved in the transition [39] (Figure 14). Qualitative analysis of X-ray spectroscopy is based on Moseley’s law, and the energy equation is as follows [40]:

$$E_x = RhC(Z-\sigma)^2\left(\frac{1}{n_1^2}-\frac{1}{n_2^2}\right) \quad (22)$$

where E_x is the characteristic X-ray energy, R is Rydberg constant (R_h = 109677.56 cm^{-1}), h is Planck’s constant ($h = 6.6262 \times 10^{-34}$ J·s), and C is the speed of photons, Z is the atomic number, σ is Shielding constant, and n_1 and n_2 are the energy series.

The number of electron transitions from any higher to any lower energy level is limited. The transitions are defined by the quantum mechanical selection rules for dipolar transitions as [41]:

- $\Delta\ell = \pm 1$
- $\Delta J = 0$ or ± 1

where ℓ, J are the quantum numbers.

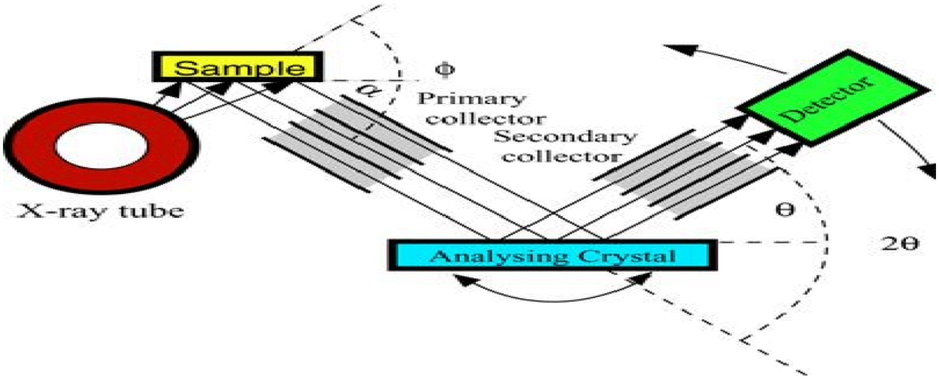

Figure 13. Schematic representation of XRF

X fluorescence spectrum

When a substance to be analyzed is irradiated with high-energy X-rays (primary X photons), electrons from the inner shells of the atom are ejected, leaving vacancies. For the atom, these vacancies create an unstable situation. The atom thus will tend to stabilize, electrons from the outer shells go into the inner shells, where they emit a characteristic x-ray with an energy equal to the difference between the two binding energies of the corresponding shells [40].

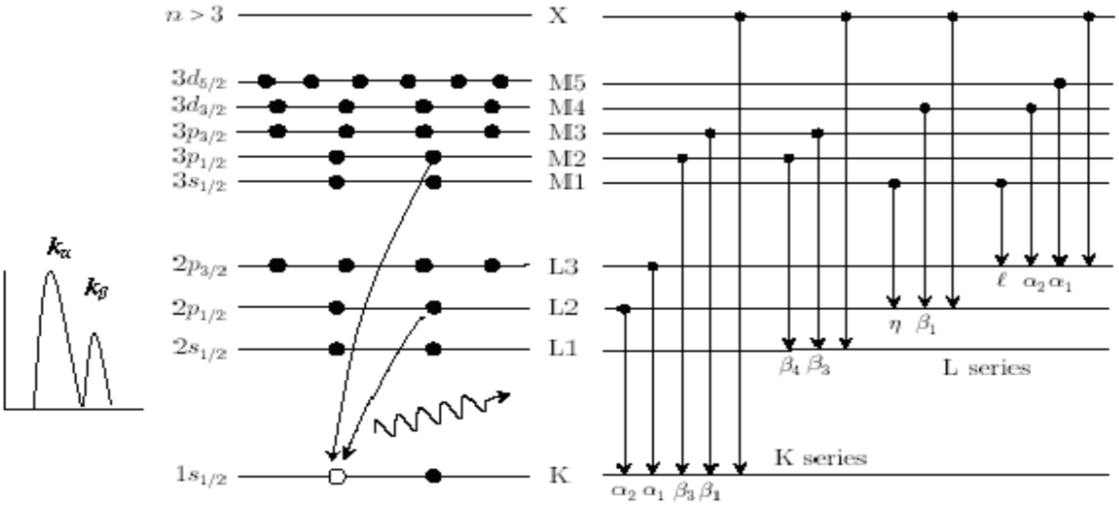

Figure 14. X ray fluorescence process

2.2.2 Wavelength dispersive X-ray fluorescence technique

The Wavelength dispersive X-ray fluorescence (WD-XRF) is a fast multi-elemental analytical technique used to determine the elemental composition of solid samples in which it allows the direct quantification of the minor and trace elements present in the sample. It includes irradiating the sample with high-energy X-rays, causing the emission of characteristic X-rays.

The setup is equipped with a crystal monochromator disperses the emitted X-rays based on their energies, which are detected and analyzed by the detector. The quantitative analysis is carried out by the calibration curve method using reference materials. The WD-XRF technique has benefits including high accuracy, non-destructive analysis, wide elemental range, and sensitivity to trace amounts. However, it is limited to solid samples and can be influenced by matrix effects [19].

WD-XRF working principle

The WD-XRF (Wavelength Dispersive X Ray Fluorescence) is a fast multi-elemental and non-destructive technique which allows a direct quantification of the minor and trace elements present in the sample (Figure 15).

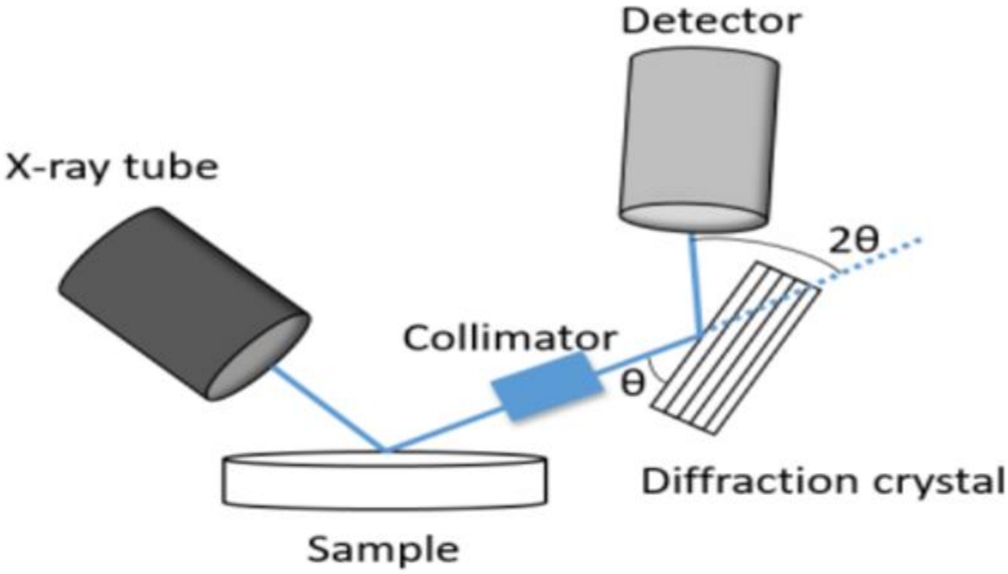

Figure 15. Schematic working principle of WDXRF system

The X-rays emitted following the excitation of the sample are diffracted on a monocrystal characterized by a given reticular distance. The wavelength of the diffracted photons, with a deviation 2θ with respect to the direction of the incident beam. is given by Bragg's law [19] (Figure 16):

$$n\lambda = 2d\sin\theta \qquad (23)$$

n: an integer

λ: Wavelengh of the X-ray

θ: Angle between X-ray and the lattice plane

d: Interplanar placing of the diffracting crystal

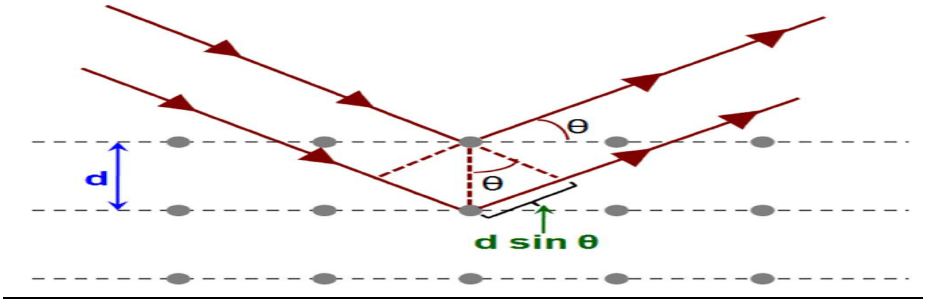

Figure 16. Deriving Bragg's Law using the reflection geometry and applying trigonometry

2.3 Quantitative X-ray Spectra analysis

Quantitative spectrum analysis is one of the most critical steps in X-ray analysis. It involves determining the concentrations of the different elements in a sample based on the intensities of the characteristic X-ray lines. In XRF, a calibration curve is often established by measuring standard reference materials with known element concentrations [42]. The intensities of characteristic X-ray peaks from the standard samples are plotted against their known concentrations, forming a calibration curve. By measuring the intensities of the peaks in the unknown sample and interpolating them on the calibration curve, the corresponding element concentrations can be determined. In WDXRF, a similar quantitative analysis can be performed using either a calibration curve or the fundamental parameters (FP) method. The calibration curve approach involves measuring standards with known concentrations to establish a relationship between X-ray intensities and element concentrations. The FP method utilizes mathematical modeling and physical properties of the sample to calculate the elemental con

I.3 Monte Carlo technique

3.1 Monte Carlo methods

The Monte Carlo method also known as MC techniques is a numerical calculation of a problem that models object-object or object-environment interactions, which refers to a group of computational algorithms based on the principle of repetition of random trials to estimate unknown parameters and that use random number generators to solve problems that cannot be solved analytically. Thus, MC methods are useful for accurately modeling complex physical problems due to its inherent capability of achieving a closer adherence to reality, and finds applications in several fields such as: radiation measurement, radionuclides standardization, radiation dosimetry, transport of radiation and it can also complement the experimental calibration procedures such as the detector calibration problems used in the gamma spectrometry measurement systems [24,25]. The physical system in the Monte Carlo algorithm is described by the function so-called "probability density function" which is given by:

$$f(x) = \sum_{i=1}^{n} N_i f_i\,(x) g_i\,(x) \qquad (24)$$

Where $N_i > 0$, $f_i\,(x)$ are normalized density functions on the interval $[x_1, x_2]$,

and $0 \leq g_i(x) \leq 1$.

3.2 Random number generator

To perform the simulations, it is necessary to generate random numbers uniformly distributed between 0 and 1. However, the storage of the results during the calculation clutters the memory of the computer. Thus, a pseudo-random number generator will be used which referred to a function that will generate a series of random numbers. Pseudo-random numbers differ from random numbers in that when the first is arbitrarily chosen, the whole sequence is completely determined and reproducible. By this effect, one can apply quality tests and verify the programs in which they are used. The following formulae is used to generate the uniformly distributed pseudo-random numbers [26]:

$$Xi = aXi\text{-}1 + c \qquad (25)$$

3.3 Radiation transport

Photons are generated using large number of particles that are produced by a random source in terms of energy, point of production and initial direction. The track (history) of each particle is viewed as random sequence, so will be probabilistically determined. The energy depended to the interaction types is sampled according to the interaction cross-section values. The final state of the particle event is also sampled.

3.4 Monte Carlo codes

Monte Carlo simulation codes are widely used for the simulation of particle transport. They are routinely used for studying both the interaction of radiation with matter in the field of applied nuclear physics, in particular in nuclear detection and statistical models. Historically, the majority of Monte Carlo development fundings has been concentrate on improving analytical techniques and enhancing the features for simulating nuclear physics processes. In this context. the demand for higher processing speeds and lower memory allocation requisites is crucial.

However, the numerical simulation should not be assimilated to reality. Considering the approximations made in the various numerical models and the uncertainty present in the cross sections, especially in the fields that are interested in low energy intervals. The comparison of results obtained using several codes may contribute to its evaluation, provided that the cross sections and physical approaches of the codes used are sufficiently different [27]. Among the main Monte Carlo codes available are EGSnrc/EGS4 (**E**lectron **G**amma **S**hower) codes, MCNP/MCNPX (Monte Carlo N-particles), GEANT4 (**Ge**ometry **a**nd **t**racking), FLUKA (**FLU**ktuierende **KA**skade) and PENELOPE (**PEN**etration and **E**nergy **LO**ss of **P**ositrons and **E**lectrons).

EGSnrc is historically the first code used in ionizing radiation metrology the 1980s. It is developed at the National Research Council Canada (NRCC) Laboratory for Ionizing Radiation Metrology. The programs sources were written in MORTRAN language which requires a preprocessor to convert it to Fortran. It is used for the simulation of the transport of photons, electrons and positrons at large interval of energies from 1 keV to 1 GeV [27].

GEANT4 was originally designed by CERN to study the physics of high energies like electromagnetic interactions of charged hadrons, ions, leptons and photons from 250eV to 1PeV or more [28]. The code was written by C++ programming language that models and simulates the interaction of particles with matter. It can be applied in many different applications include radiation physics, accelerator physics, as well as studies in nuclear medicine. The software requirements of contemporary experiments are what drive GEANT4. Thus, it contains all the detailed of the event generator components, the detector simulation, the reconstruction and analysis that can be used separately or in combinations [29].

FLUKA is a Monte Carlo Code for particle interaction and transport of electromagnetic and hadronic particles, it treats cascades induced by high energy particles. It contains detailed models of electromagnetic interactions hadron-hadron, nucleus-hadron over a wide energy range from MeV to TeV. FLUKA is frequently used for studies related to basic research as well as applications in radiation protection and dosimetry, including the radiation damage in space missions, radiobiology and cosmic ray calculations [30].

PENELOPE is a Monte Carlo simulation that used for the treatment of coupled electron-photon transport in arbitrary materials for a large energy range, from eV to GeV. Photon transport is simulated by means of the standard, while electron and positron histories are generated on the basis of a mixed procedure, which combines detailed simulation of hard events with condensed simulation of soft interactions [31].

3.5 MCNP code

The MCNP (Monte Carlo N-Particle) Code, created by Los Alamos National Laboratory, uses the generation of pseudo-random numbers for radiation transport. It is useful for accurately modeling complex physical problems and also to complement the experimental calibration procedures such as the detector calibration problems used in the gamma spectrometry measurement systems. It is consisted of the numerical generation of photon histories which is used to simulate the detection process [9,11,32]. Previous relevant studies [12, 33-37] proved that this code is sufficiently advanced and reliable to be used for the determination of full energy peak efficiency, self-absorption and summing coincidence effect corrections. The MCNP code input file contains all the detailed information about geometry, materials, energy, position and cross-section data for neutron, photon, and electron transport calculations to truly reflect the real geometry in the laboratory where the experiments are carried on. Cross-section data are considered as an important part of the simulation because each transported particle has its own path which is presented by a probabilistic behavior.

3.6 MCNP code structure

Input File

The main input file for the user contains the input information to describe the problem.

An input file has the following form [38]*:*

Message Block

Blank Line Delimiter

One Line Problem Title Card

Cell Cards

..

Blank Line Delimiter

Surface Cards

Blank Line Delimiter

Data Cards

Blank Line Terminator (optional).

A. Geometry specifications

The geometry of MCNP is composed of different cards such as surfaces. Cells, materials… that accurately help to describe the problem. The geometry must be surrounded by a sphere.

B. Surface cards

Surfaces are defined as the boundaries in space used to create cells (spheres, cylinders, planes…). Table 1 shows the famous surfaces card used in MCNP5 code.

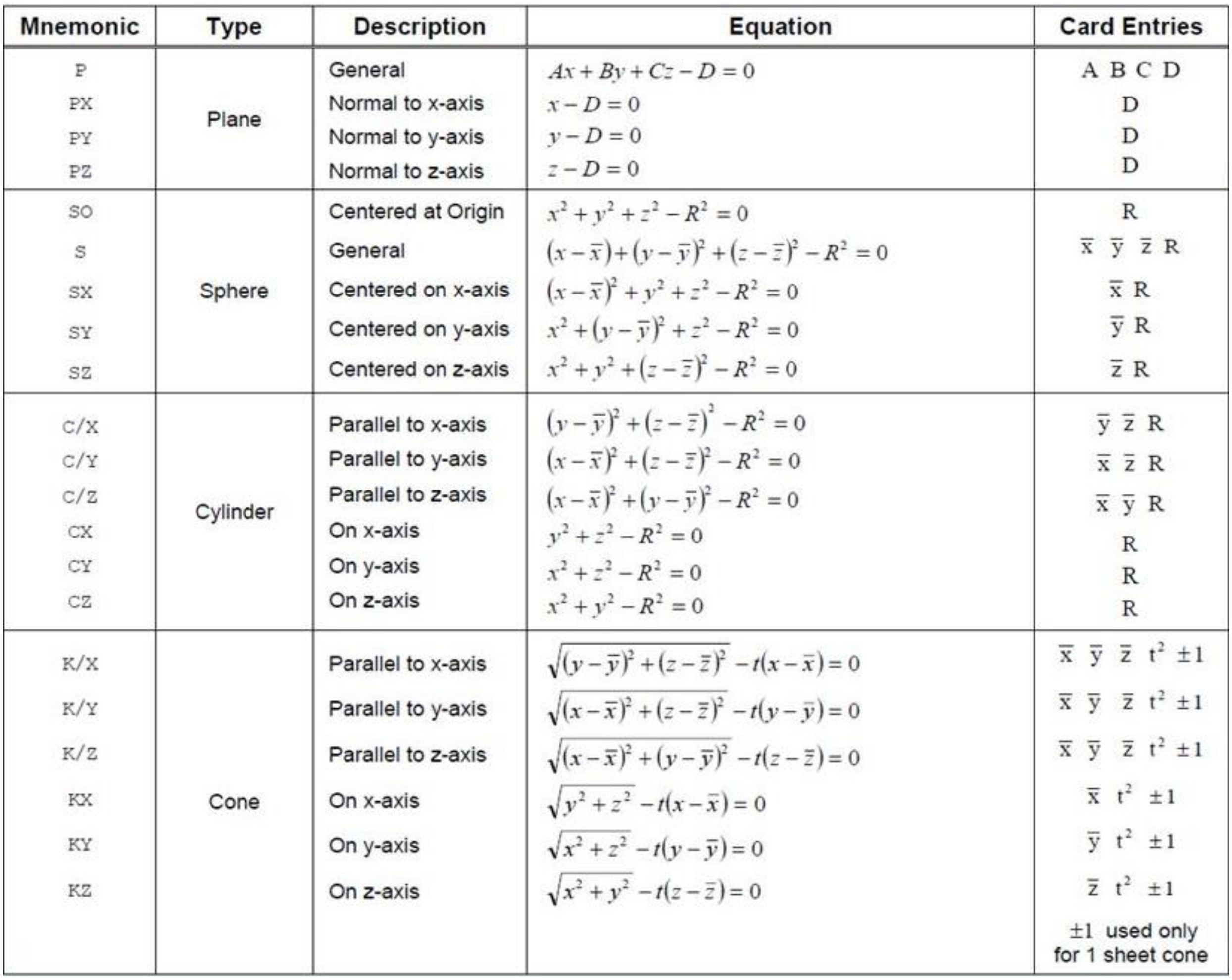

Mnemonic	Type	Description	Equation	Card Entries
P	Plane	General	$Ax + By + Cz - D = 0$	A B C D
PX		Normal to x-axis	$x - D = 0$	D
PY		Normal to y-axis	$y - D = 0$	D
PZ		Normal to z-axis	$z - D = 0$	D
SO	Sphere	Centered at Origin	$x^2 + y^2 + z^2 - R^2 = 0$	R
S		General	$(x - \bar{x}) + (y - \bar{y})^2 + (z - \bar{z})^2 - R^2 = 0$	$\bar{x}$ $\bar{y}$ $\bar{z}$ R
SX		Centered on x-axis	$(x - \bar{x})^2 + y^2 + z^2 - R^2 = 0$	$\bar{x}$ R
SY		Centered on y-axis	$x^2 + (y - \bar{y})^2 + z^2 - R^2 = 0$	$\bar{y}$ R
SZ		Centered on z-axis	$x^2 + y^2 + (z - \bar{z})^2 - R^2 = 0$	$\bar{z}$ R
C/X	Cylinder	Parallel to x-axis	$(y - \bar{y})^2 + (z - \bar{z})^2 - R^2 = 0$	$\bar{y}$ $\bar{z}$ R
C/Y		Parallel to y-axis	$(x - \bar{x})^2 + (z - \bar{z})^2 - R^2 = 0$	$\bar{x}$ $\bar{z}$ R
C/Z		Parallel to z-axis	$(x - \bar{x})^2 + (y - \bar{y})^2 - R^2 = 0$	$\bar{x}$ $\bar{y}$ R
CX		On x-axis	$y^2 + z^2 - R^2 = 0$	R
CY		On y-axis	$x^2 + z^2 - R^2 = 0$	R
CZ		On z-axis	$x^2 + y^2 - R^2 = 0$	R
K/X	Cone	Parallel to x-axis	$\sqrt{(y - \bar{y})^2 + (z - \bar{z})^2} - t(x - \bar{x}) = 0$	$\bar{x}$ $\bar{y}$ $\bar{z}$ t^2 ±1
K/Y		Parallel to y-axis	$\sqrt{(x - \bar{x})^2 + (z - \bar{z})^2} - t(y - \bar{y}) = 0$	$\bar{x}$ $\bar{y}$ $\bar{z}$ t^2 ±1
K/Z		Parallel to z-axis	$\sqrt{(x - \bar{x})^2 + (y - \bar{y})^2} - t(z - \bar{z}) = 0$	$\bar{x}$ $\bar{y}$ $\bar{z}$ t^2 ±1
KX		On x-axis	$\sqrt{y^2 + z^2} - t(x - \bar{x}) = 0$	$\bar{x}$ t^2 ±1
KY		On y-axis	$\sqrt{x^2 + z^2} - t(y - \bar{y}) = 0$	$\bar{y}$ t^2 ±1
KZ		On z-axis	$\sqrt{x^2 + y^2} - t(z - \bar{z}) = 0$	$\bar{z}$ t^2 ±1
				±1 used only for 1 sheet cone

Table 1. Surface cards Library used in MCNP code.

C. Cell cards

The cell number is the first entry and it is defined as the intersection, union or complement of several surfaces. The next entry material number which represents the type of material that constitutes the cell (Mn). Next is the cell density of the material in which the positive entry is interpreted as density in units of 10^{24} atoms.cm^{-3} and the negative entry is referred as mass density in units of g.cm^{-3}.

D. Data specifications

Defines source definitions (SEDF), mode used, materials, tallies and other information needed for solving the problem.

E. MODE card

MCNP can be run in three different modes:

Mode N: neutron transport (default).
N P: neutron and neutron-induced photon transport.
P: photon transport.

F. Tally specification cards

The tally cards are used to specify what you want to learn from the Monte Carlo calculation, that is, current across a surface, flux at a point, etc. The following Table 2 shows all the cards associated with tallies with a full description of each one.

G. Materials specification

The materials cards (Mm) define a unique material number and specify the isotopic composition of the materials and the cross-section evaluations to be used in the cells. The following card is used to specify a material for all cells containing material m:

Mm $ZAID_1$ $fraction_1$ $ZAID_2$ $fraction_2$ ....

H. Source specifications

The source card known as (SDEF) command is a Powerful feature in MCNP code. It allows the specification of spatial extension, energy, direction, and particle radiation type. The SDEF command has many parameters that are used to define all the characteristics of all sources in the problem such as point source, area source, volume source, multiple sources or biasing of one or more aspects of the source term.

The SDEF card defines the basic source parameters, some of which are

POS = the position of the particle x y z default is 0 0 0;

CEL = starting cell number;

ERG = the energy of the particle in MeV (starting energy default is 14 MeV);

WGT= the statistical weight of the particle (starting weight default is 1);

TME = the time in shakes (10~8 sec) default is 0.

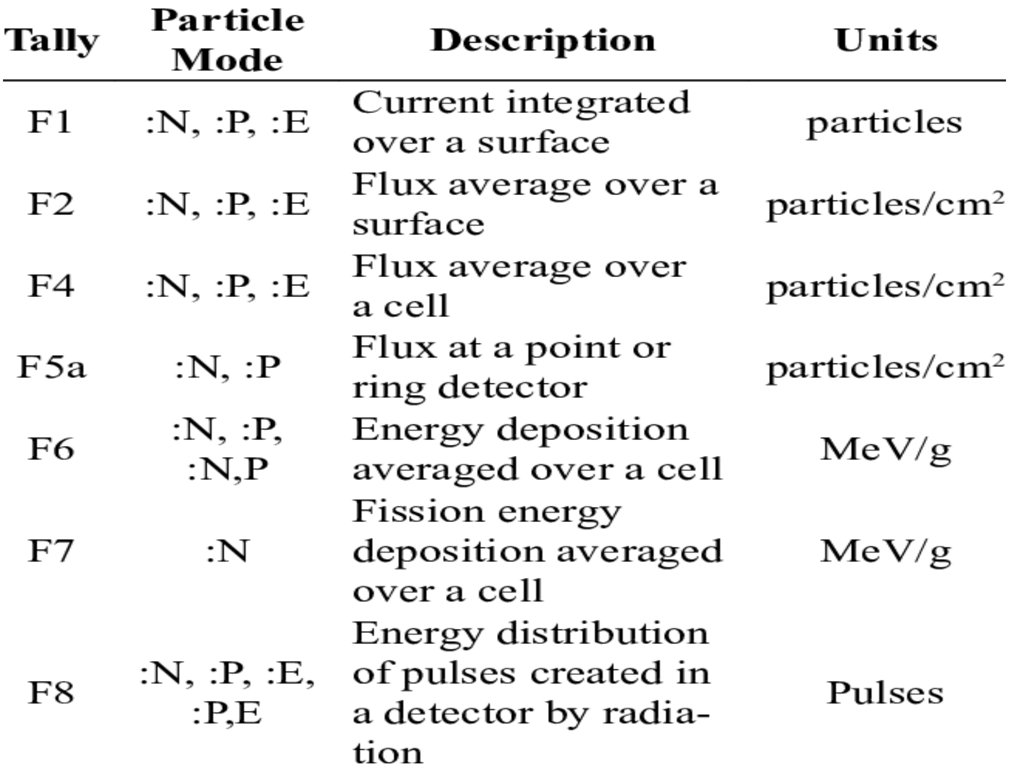

Tally	Particle Mode	Description	Units
F1	:N, :P, :E	Current integrated over a surface	particles
F2	:N, :P, :E	Flux average over a surface	particles/cm^2
F4	:N, :P, :E	Flux average over a cell	particles/cm^2
F5a	:N, :P	Flux at a point or ring detector	particles/cm^2
F6	:N, :P, :N,P	Energy deposition averaged over a cell	MeV/g
F7	:N	Fission energy deposition averaged over a cell	MeV/g
F8	:N, :P, :E, :P,E	Energy distribution of pulses created in a detector by radiation	Pulses

Table 2. Types of tallies available in MCNP.

Chapter II: Materials and Methods

II.1 Experimental device of the gamma spectrometry technique laboratory

The gamma spectrometry chain used in this study includes a high-resolution Ge(HP) type semiconductor detector, a DSA system for signal processing, a computer for data visualization and analysis. and the Genie-2000 software for data processing and analysis.

1.1 HPGe detector

The measurements were performed by closed end coaxial, p-type Canberra HPGe model GX-3519. The detector has a relative efficiency of 35% at 1.33 MeV relative to 3”×3” NaI(Tl) crystal with an energy resolution (FWHM) of 1.85 MeV at 1332.5 keV and 0.86 keV at 122keV, both for ^{60}Co. The crystal diameter is 60.5 mm, a length is 61mm and a carbon epoxy window has a thickness of 0.5 mm. Its core hole has the diameter of 12 mm and depth of 51 mm. The adjustment of the dead layer was estimated by Mezerreg et al.2021 [44] with a thickness of 190 µm which is used in the simulation for this study. The detector surrounded by lead shielding consists of 100 mm graded lead, liners of 1 mm tin and 1.6 mm copper in order to minimize the contribution of the lead X-rays in the spectra (See Figure 17) [45]. These detailed characteristic of the detector and lead shield with the dead layer value were used in the simulated model for this study.

Each sample was measured for 10000 seconds to obtain good statistical uncertainties. The obtained spectra were treated using Genie 2000 software provided by Canberra industry [46].

Figure 17. The configuration measurement used in this study

1.2 DSA (Digital Spectrum Analyzer) system

The DSA system is a set of electronic components that processes the signals produced by the detector. It is connected to a computer via the USB port. It includes amplifiers and signal processors that amplify, adjust and process the pulses delivered by the detector. This system converts the analog signal from the detector into a digital signal that can be processed by a computer.

1.3 Genie 2000 software

The Genie-2000 software is a commonly used for gamma spectrometry analysis. It is used to process the data collected by the detector and generate gamma-ray spectra. It consists of several modules that work together: Hardware configuration editor, Certificate editor, Library editor, MCA input definition and Acquisition and Gamma Analysis [19].

1.3.1 Hardware Configuration Editor:

This module allows users to configure and set up their hardware such as detectors and measurement systems by adding and configuring an MCA analyzer. The module includes a wizard-style interface that guides users through the configuration process and allows them to set parameters such as gain. high voltage, and energy windows [71].

1.3.2 Certificate Editor:

The Certificate Editor module enables users to create and manage calibration certificates for the detector. The module provides a range of tools for creating, editing, and printing calibration certificates with a view of calibration in terms of energy, resolution and efficiency.

1.3.3 Library Editor:

The Library Editor module enables users to create and manage libraries of spectra for the qualitative and quantitative analysis of the nuclides. The module includes tools for creating, editing, and merging libraries, as well as for comparing spectra and identifying unknown isotopes. It also includes a standard library. a demonstration library for NaI (Tl) and one for hyper-pure germanium [46].

1.3.4 MCA Input Definition:

is used for the processing and analysis of the raw spectral data obtained from the detector. It involves setting up the parameters of the MCA, such as the number of channels, the gain, the energy ranges, and configure the physical hardware (total analyzer memory, its memory address, hardware driver, etc. Once the analyzer has been created with the configuration editor, it is saved as a file in MID format, then loaded into the analyzer database to be used during the acquisition step [18,46]**.**

1.3.5 Acquisition and Gamma Analysis:

This module is the heart of the Genie 2000 software and provides users with powerful capabilities to acquire and analyze the gamma spectrum of the given sample. The module includes a range of tools for acquiring data from detectors, such as live spectra and time-based acquisitions, and for analyzing gamma-ray spectra like peak fitting, nuclide identification, and quantitative analysis. The main menus are: File, Analyzer, Calibration, View, Analysis, Edit, Options, Sources and Help [18,46].

II.2 Calibration of the measurement chain

Energy calibration:

It is the process of determining the relationship between the channel number of the Multi-Channel Analyzer (MCA) and the corresponding gamma-ray energy. This relationship is necessary for converting the channel number of an unknown gamma-ray into its corresponding energy, which is important for identifying the gamma-ray emitting radionuclide and quantifying its activity. This process is carried out a point radioactive point source whose gamma energies are well known. The ^{152}Eu source was used to calibrate the gamma measurement chain during 3a time of 3600 seconds. The calibration line giving the energy as a function of the channel number was determined by adjusting the experimental points in which the channel numbers on the MCA represent real energies rather than virtual ones. Table 3 listed the main gamma energies of the ^{152}Eu source used for the energy calibration.

Energy (keV)	**Chanel Number**
121.87	336.00
244.69	667.00
344.24	936.00
778.92	2101.72
867.46	2340.60
964.12	2601.37
1112.27	3001.08
1408.54	3800.37

Table 3. Channel numbers corresponding to the gamma energies of the ^{152}Eu source spectrum

The calibration line is defined as:

$$E= a\times canal + b \quad (26)$$

Where $a= 0.37$ and $b= -1.97$

II.3 Laboratory Standard Preparation

A gamma mixed solution consisting of ^{241}Am, ^{109}Cd, ^{57}Co, ^{139}Ce, ^{51}Cr, ^{113}Sn, ^{85}Sr, ^{137}Cs, ^{88}Y and ^{60}Co. type ERX certified by Czech Metrology Institute in frame of ALG5031 Project. The standard gamma solution covering the energy range of 59.54–1836.12 keV was injected directly into sample containers that were being used for measurements.

The soil and the plant matrices were placed in two identical cylindrical containers with a filling level of 4.1 cm and 5.2 cm. respectively. Both containers were taken as reference samples. For the plant matrix. 29 ml of the standard solution was taken using a micropipette and injected into four layers. the first two layers contain 8 ml for each one and the rest two layers contain 7 ml and 6 ml. respectively. For the soil matrix. 21 ml were added and distributed in three layers. Each layer containing 7 ml of the standard solution. The spiked matrices were well stirred in each measuring container in order to obtain a homogeneous distribution of the activity in samples, and then dried overnight. The preparation procedure was carried out at the Nuclear Techniques Division of Nuclear Research Center of Algiers (CRNA). Table 4 show the radionuclides activity with their uncertainties.

Radionuclide	Half life	Activity (KBq)	The activity uncertainty (%)
Am-241	432.6 (6) years	13.72	7
Cd-109	461.9 (4) days	53.08	74
Ce-139	137.641 (20) days	4.348	76
Co-57	271.81 (4) days	4.348	39
Co-60	5.2711 (8) years	6.317	50
Cs-137	30.05 (8) years	63.3	69
Sn-113	115.09 (3) days	8.49	18
Sr-85	64.850 (7) days	12.93	9
Y-88	106.63 (5) days	6.907	13
Cr-51	27.704 (4) days	21.62	11

Table 4. The used radionuclides activities

II.4 Efficiency calibration using the standard preparation

In order to obtain trustworthy measurements, an accurate calibration is required. In this study, plant and soil reference materials contains the gamma energies ranged from 59.54 to 1836.12 keV was used for the calibration of the detector. Each reference material was measured for 10000 seconds to obtain good statistical uncertainties.

The activity of each radionuclide is calculated by:

$$A = A_0 \, e^{-\frac{ln2}{t1/2}t} \qquad (27)$$

Where:

$t_{1/2}$: is the period of the radionuclide.

t : time since the start of the decay.

A_0: is the specific activity, calculated as the following:

$$A_0 = \frac{A_{0_{radionuclide}} \times m_{sample}}{m_{solution}} \quad (28)$$

With, $m_{solution}$: 106.5 g, m_{sample}= 30.9 g and 22.4 g for soil and plant masses, respectively. The absolute FEPE detector efficiency is given by the following expression [23]:

$$\varepsilon_{exp} = \frac{N}{A.I_\gamma.t_c} \quad (29)$$

Where A is the activity defined in the above equation. N is the net area at the interest peak energy corrected for background counts, I_γ is the γ-ray emission probability and t_c is the counting time. The experimental efficiency uncertainty given by the error propagation law as the following:

$$\delta\varepsilon_{exp} = \varepsilon_{exp}\sqrt{\left(\frac{\delta N}{N}\right)^2 + \left(\frac{\delta A}{A}\right)^2 + \left(\frac{\delta I_\gamma}{I_\gamma}\right)^2 + \left(\frac{\delta \boldsymbol{t_c}}{\boldsymbol{t_c}}\right)^2} \qquad (30)$$

II.5 Monte Carlo simulation

Modelling of source-HPGe detector MCNP5

The important number of the radiation with matter interactions and the random radiation path (electron, photon) cannot be described with precise analytical formulae. Thus, one can apply Monte Carlo simulation using MCNP code, where it can used random numbers to describe the photon-electron transport throughout the detector at the event-level.

The general-purpose of Monte Carlo radiation transport code MCNP5 is frequently used to the behavior of particles in complex geometries and materials.

When a gamma ray interacts with the germanium crystal, it generates electron-hole pairs, and the resulting charge carriers are collected and measured to determine the energy and intensity of the incident gamma ray. Thus, MCNP5 code can be used to simulate the interactions of gamma rays with the germanium crystal, the transport of the resulting particles (electrons, photons) through the detector material, and their interactions with the detector components (crystal, dead layer).

The configuration measurement compound of active germanium detector and the liquid standard source distributed in cylindrical geometry for plant and soil matrices were modeled using an MCNP5 code, in order to determine the full energy peak efficiency of the detector for the both matrices. To create a realistic detector simulation, the input file involved all the necessary data to describe the experimental setup. The high precision geometry, dimensions and materials data of the detector, the sample container and the lead shielding were introduced in detail in cell, surface and material cards of the input file which is composed of 23 cells and 69 surfaces.

The cylindrical containers of diameter 8.0 cm were filled with plant and soil matrices. Both containers contained gamma solution and sit on top of the detector. The chemical composition of the two samples was determined by Wavelength Dispersive X-Ray Fluorescence (WD-XRF) technique and included in the material card to use it in sample cell.

Figure 18 presents the simulated HPGe detector by MCNP5 code with the cylindrical sample placed in the lead shield chamber.

The mode P (photon) was used in the simulation to reduce the run time since the difference between the mode PE (Photons and Electrons) and the mode P results is less than 1% [48,49]. The total number of histories used is 10^8 with run time of 73 min for every simulated gamma energy to reduce the statistical uncertainties [49]. The number of bins used was 1024. based on the energy calibration obtained from the experiment and the cut-off energy for the photons was setup at 1 keV [50, 51]. The F8 tally card was used for determining the detector response from the pulses produced in the crystal. The GEB function was used to simulate the Gaussian Energy Broadening obtained from the experimental spectrum. The GEB card parameters were obtained from the experimental spectrum by fitting the full width at half maximum (FWHM) using the following expression [44]:

$$\mathrm{FWHM}= \mathrm{a} + \mathrm{b}\sqrt{E + cE^2} \qquad (31)$$

Where E is the energy of the incident particle. For the detector used a = 0.70710× $10^{-3} MeV.$

b = 0.946× *and* c = 0

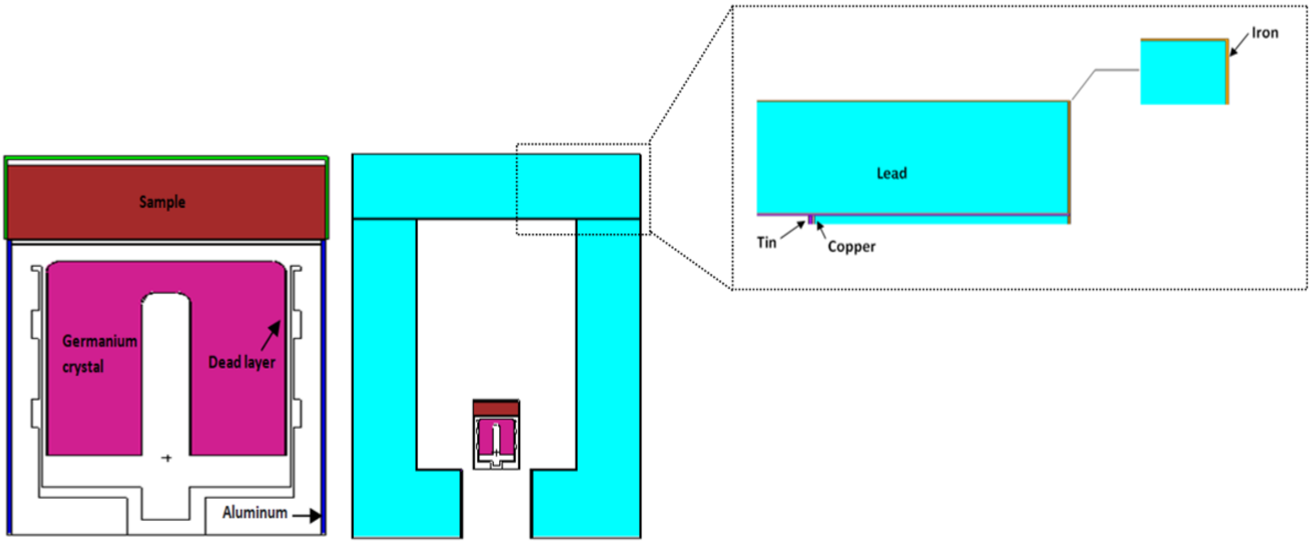

Figure 18. Simulated HPGe detector with cylindrical geometry and shield by MCNP5.

II.6 Characterization of soil and plant matrices using WD-XRF technique

In order to obtain reliable results. The MCNP5 input file requires a precise elemental composition of used sample. For this task, WD-XRF techniques was used for the characterization of soil and plant matrices. The technique is a model of MagixPro high-performance analytical instrument equipped with a Rhodium (Rh) X-ray tube and a set of eight crystal analyzers that can detect elements ranging from Bore to Uranium [19]. The quantitative analysis was carried out by the calibration curve method, obtained with soil and plant standard samples and performed in 42 minutes per sample.

Sample preparation for WD-XRF analysis

Samples were ground using stainless steel. The powders are homogenized using a mixer-mill. Aliquots of 1.5 g weighed from these splits are transferred to cylindrical sample-dies. and with boric acid as a backing. are pelletized at a pressure of 2000 tones in a hydraulic press to give pellets of 41 mm diameter.

II.7 EDXRF system Instrumentation

The used XRF System is of model Thermo Scientific ARL QUANT' which provides a fast and cost-effective analytical capability, allowing for the simultaneous measurement of the emission lines for all elements from sodium (Na, Z=11) through uranium (U, Z=92). It is fitted with an air-cooled Rh end-window tube with thin Be window (0.05 mm) and has a maximum power of 50 Watts. The ARL QUANT'X Spectrometer is equipped with an electrically cooled silicon drift detector (SDD) with an area of 30 mm^2. The instrument features a total of nine primary beam filters ensuring that an optimal excitation condition is always found. In other word, the filters are used to modify the characteristics of the primary x-ray beam emitted from the x-ray tube and are selected based on the elements being analyzed (Table 7). An optional 10 position sample changer allows for unattended analysis [52].

7.1 Sample preparation for XRF analysis

Thirteen samples (7 crops and 6 soils) were ground into a fine powder using stainless steel for soil samples and milling machine for crop samples. The samples passed through a sieve to remove any large particles and to ensure homogeneity. After that. an amount of each sample equals to the standard weight is weighed out, which is about 2g and then placed into capsules. Each sample was measured for 3min. The excitation conditions are shown in Table 5. This procedure was repeated for each collected soil and crop samples. The samples were analyzed using soil reference material (**SRM 2706**) and tomato leaves reference standard (**SRM 1573a**). The results are listed in Table 9 and Table 10 mentioned in chapter 4 (See Figure 19).

7.2 Spectrum analysis

The electrical signals from the detector are then processed and analyzed to obtain elemental concentration data. This typically involves comparing the energy and intensity of the emitted X-rays to the used standards to determine the concentration of each element in the sample.

For the quantitative treatment of the spectra, the software programs Axil and WinTrace were used. WinTrace, in particular, is a comprehensive suite of programs specifically designed to facilitate instrument automation, acquisition control, and data analysis in conjunction with the Thermo Scientific QUANT'X or QuanX-EC system.

The concentration of each element was calculated by:

$$I_{st}.m_{tot\,sp}.C_{sp} = I_{sp}.m_{tot\,st}.C_{st} \qquad (32)$$

Where:

I_{st}: is the intensity of the standard (Soil/ tomato).

$m_{tot\ sp}$: is the total mass of the analyzed sample.

C_{sp}: is the concentration of the sample.

I_{sp}: is the intensity of the sample.

$m_{tot\ st}$: is the total mass of the standard.

C_{st}: is the concentration of the sample.

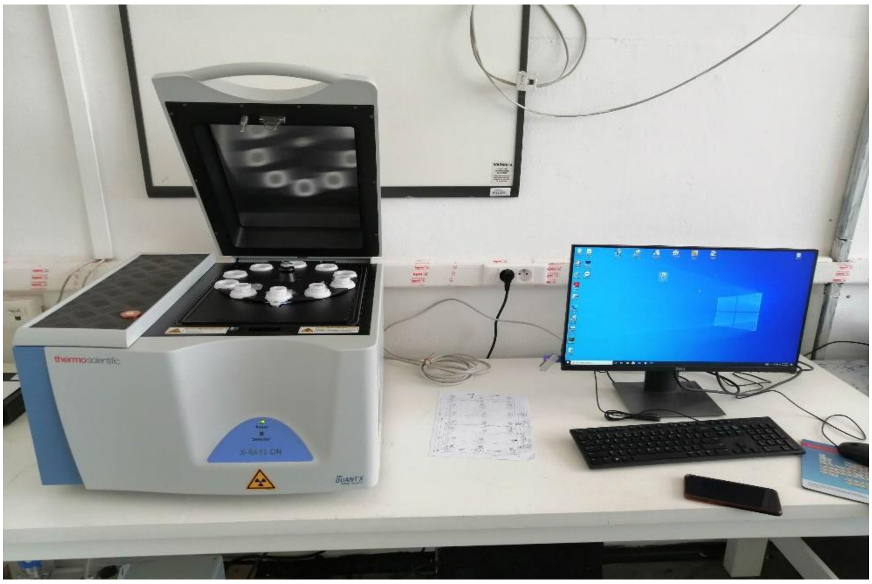

Figure 19. X-ray fluorescence spectrometer

Condition	Used Filter	Voltage (kV)	Auto current	Atmosphere	Count Rate	Elements
High Zb	Cu Thick	50	1.00	Air	Medium	Cd, Ba
Low Za	No filter	4	2.00	Air	Medium	Mg,Al,Si,P,S
Mid Za	Pd Thin	16	2.00	Air	Medium	Ti,V,Cr,Mn,Fe,Ni,La,Nd,Ce,Ba
Mid Zc	Pd Thick	30	1.66	Air	Medium	Ni,Cu,Zn,As,Rb,Sr,Y,Zr,Pb,Th, Ga,Br,Mo,Nb
Low Zb	C Thick	8	2.00	Air	Medium	K, Ca, Sc

Table 5. Excitation conditions.

Chapter III: Results and Discussion

This chapter aims to investigate the effect of the matrix composition on the self-absorption correction for plant and soil matrices using Monte Carlo simulation, applied on gamma spectrometry technique with HPGe coaxial P-type detector. The simulated model will be validated by comparison with the experimental measurements using a mixed standard solution containing the radionuclides ^{241}Am, ^{109}Cd, ^{57}Co, ^{139}Ce, ^{51}Cr, ^{113}Sn, ^{85}Sr, ^{137}Cs, ^{88}Y and ^{60}Co, which cover a wide range of gamma energies [59.54-1836.12] keV. After that, the model will be used successfully for an environmental application mentioned in chapter 5 in order to determine the soil to plant transfer factors of the natural radionuclides ^{226}Ra, ^{232}Th, and ^{40}K and FRN (Fallout RadioNuclide) ^{137}Cs, for mustard, artichoke, fennel, bean, mushroom, onion and garlic crops. These factors are calculated as the ratio of the activity concentration in plant and its corresponding soil.

III.1. Energy and efficiency calibration curves in the Gamma measurement chain

The energy and efficiency calibration curves, as detailed in the materials and methods section, were successfully generated and used to validate the gamma measurement chain. Figure 20 and Figure 21 present the experimental spectrum of ^{152}Eu measured for 10000s and the energy calibration line obtained by Genie 2000, respectively. Additionally, Figure 22 and Figure 23 show the plant and soil efficiency curves, demonstrating the detection efficiency of the system across the studied range of gamma-ray energies.

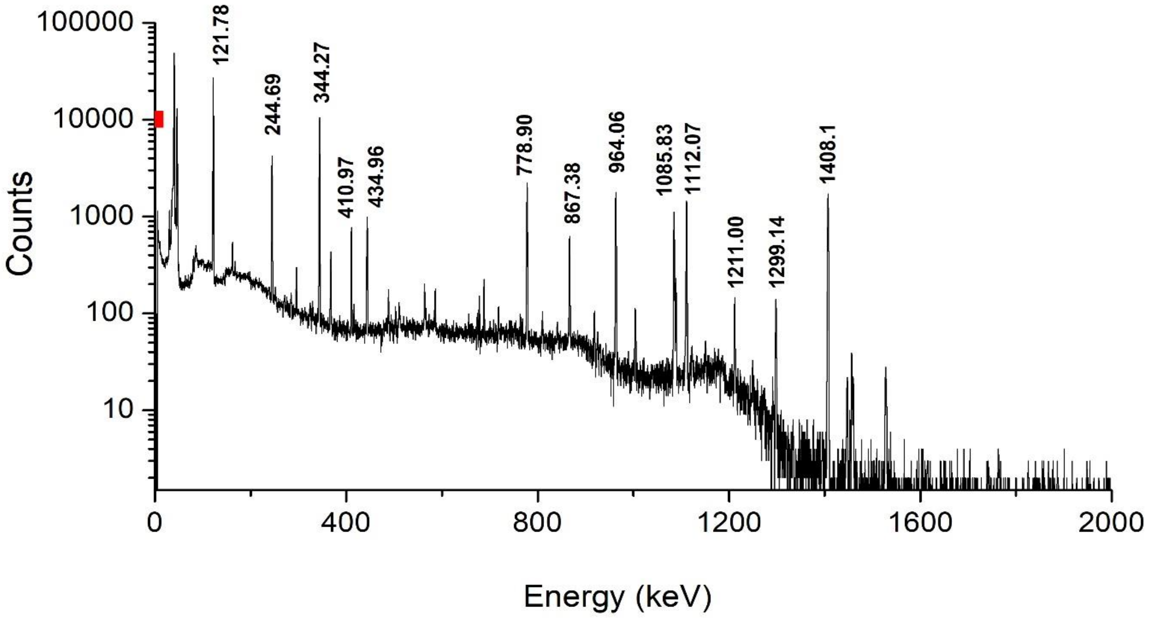

Figure 20. Gamma spectrum of ^{152}Eu measured during 10000 s

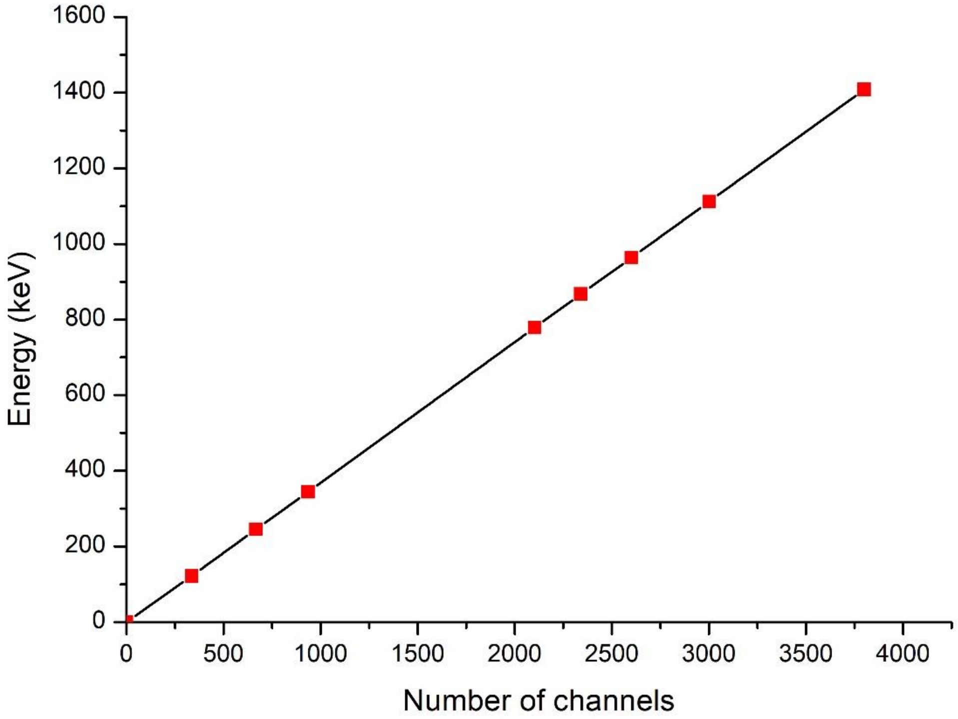

Figure 21. Calibration line

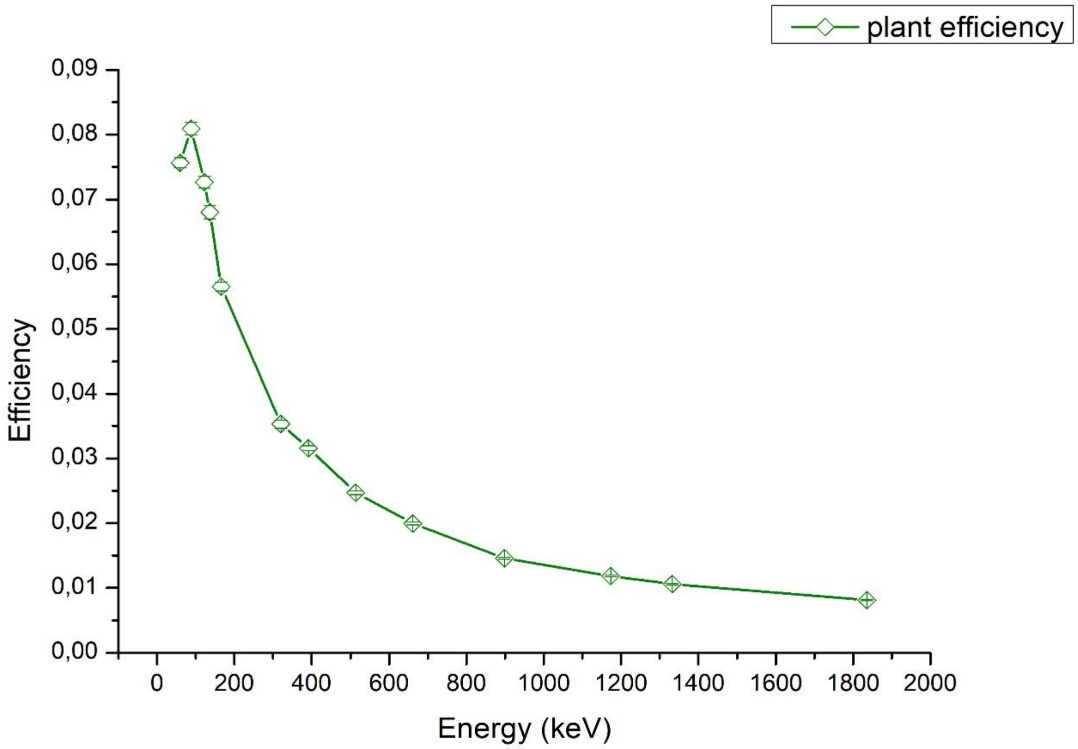

Figure 22. Experimental efficiency of the detector for multi-gamma source mixed in plant matrix

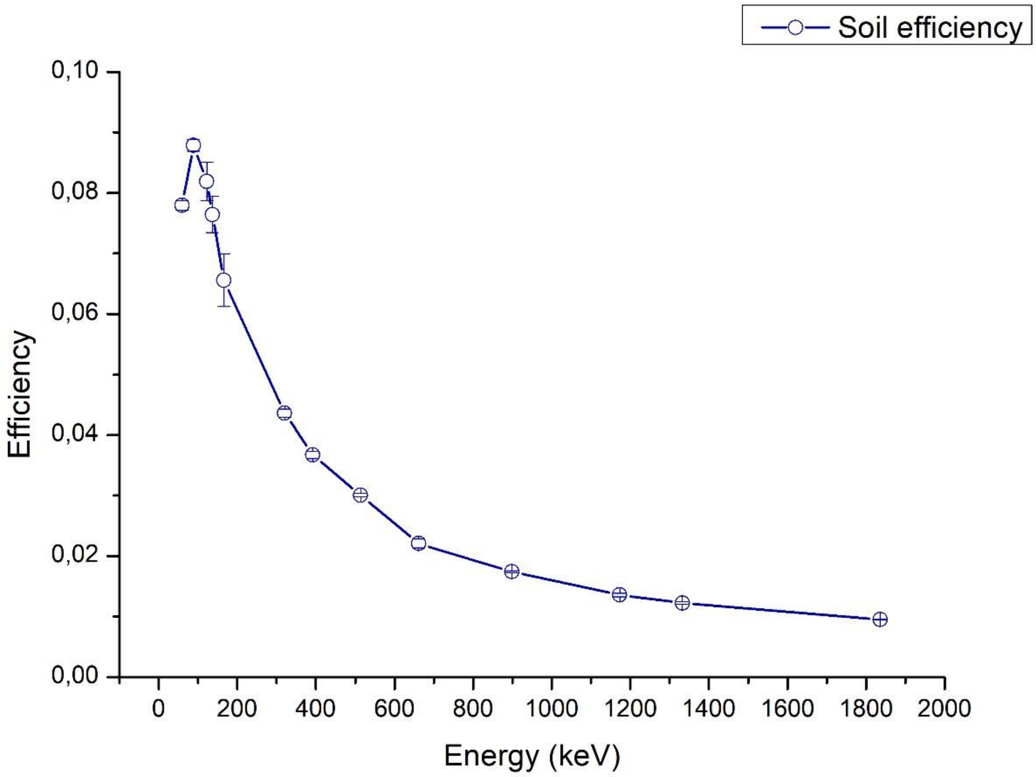

Figure 23. Experimental efficiency of the detector for multi-gamma source mixed in soil matrix

III.2. Validation of the detector-source model

After achieving the model, it should be validated using the experimental measurements. For this purpose, a standard solution contains various gamma energies ranged from 59.54 to 1836.12 keV has been used for the determination of the FEPE curve for soil and plant samples. The Monte Carlo FEPE was simulated for each gamma energy [48]. Two different sets of simulation were run: the first includes the soil matrix while the second presents the plant matrix. The results of the plant and soil samples composition used in the input file are presented in Table 6 and Table 7. The experimental efficiency results with their relative uncertainties (%) and the MCNP to the measured values shift for soil and plant matrices were listed in Table 8. The absolute uncertainty associated to simulated efficiency values with MCNP5 code was found less than 0.01%.

For the low gamma ray energies and particularly in the radionuclide ^{241}Am. the maximum discrepancy is roughly about 20% for the soil matrix and 10% for the plant matrix. This deviation is explained by the self-absorption effect because of the strong dependence of the

FEPE on material composition and atomic number, specifically with gamma energy less than 150 keV [53]. Besides, for the high gamma energies important discrepancies are observed in the radionuclides ^{88}Y and ^{60}Co due to the coincidence summing effect [32, 44, 53]. It is necessary to correct this effect in order to obtain precise efficiency values for calculating specific activities of ^{226}Ra. ^{232}Th and ^{40}K.

The remaining gamma energies of the radionuclides ^{57}Co,^{139}Ce,^{51}Cr,^{113}Sn, ^{85}Sr and ^{137}Cs showed a good agreement between the experimental results and the MCNP ones.

The Figure 24 shows a qualitative calibration of measured and simulated efficiency spectrums of gamma energies in the range of 59.54-1836.12keV presented in mixed gamma solution. The photo peaks position and the overall structure shows a good agreement. This signifies that the major interactions Compton Effect. Photoelectric and Pair Production are well defined in crystal germanium detector [54]. The presence of X-rays peaks in measured spectra is owing to the environmental background and radionuclides composed the mixed gamma source.

In order to clarify the deviation between the experimental and the MCNP results. the fitting of the FEPE curves of the HPGe simulated in MCNP5 and the measuring one for plant and soil matrices is presented in Figure 25 and Figure 26, respectively. These curves were used to calibrate the detector at the energy interval [59.54-1836.12] keV for soil and plant matrices in the environmental radioactivity laboratory.

Element (soil)	C	O	Na	Mg	Al	Si	P	S	Cl
Concentration (%)	0.69	48.48	0.11	0.48	14.1	28.98	0.18	0.09	0.16
Element (soil)	K	Ca	Ti	V	Cr	Mn	Fe	Zr	Ba
Concentration (%)	0.97	0.84	0.47	0.01	0.012	0.03	4.21	0.01	0.01

Table 6. Elements present in soil for MCNP Materials Card analyzed by WD-XRF.

Element (plant)	C	O	Na	Mg	Al	Si	P
Concentration (%)	36.63	25.38	0.34	0.79	1.13	4.26	1.49
Element (plant)	Cl	K	Ca	Mn	Cr	Fe	S
Concentration (%)	2.14	2.32	23.66	0.07	0.02	0.47	1.30

Table 7. Elements present in plant for MCNP Materials Card analyzed by WD-XRF.

Radionuclide		Am-241	Cd-109	Co-57	Co-57	Ce-139
Energy (keV)		59.54	88.03	122.06	136.4	165.8
Plant matrix	Efficiency Measured	7.57E-02 ± 7.74E-04	8.09E-02 ± 9.53E-04	7.27E-02 ± 9.20E-04	6.80E-02 ± 1.01E-03	5.65E-02 ± 6.99E-04
	Efficiency Simulated	6.81E-02	7.37E-02	7.21E-02	6.97E-02	6.38E-02
	Shift*	9.98E-02	8.93E-02	7.71E-03	2.46E-02	1.28E-01
Soil matrix	Efficiency Measured	7.80E-02 ± 8.08E-04	8.79E-02 ± 9.07E-04	8.19E-02 ± 1.19E-03	7.65E-02 ± 1.26E-03	6.56E-02 ± 9.22E-04
	Efficiency Simulated	6.27E-02	8.29E-02	8.45E-02	8.29E-02	7.62E-02
	Shift*	1.96E-01	5.64E-02	3.15E-02	8.43E-02	1.62E-01

Table 8. Comparison of the simulated to experimental FEPEs for a cylindrical geometry in soil and plant matrices.

Y-88	Cs-137	Sr-85	Sn-113	Cr-51	Radionuclide
898.04	661.6	513.98	391.4	320.08	Energy (keV)
1.46E-02 ± 1.53E-04	1.99E-02 ± 2.16E-04	2.47E-02 ± 3.07E-04	3.16E-02 ± 3.76E-04	3.53E-02 ± 6.37E-04	Plant matrix
1.50E-02	2.08E-02	2.52E-02	3.24E-02	3.85E-02	Soil matrix
2.90E-02	4.27E-02	2.00E-02	2.64E-02	9.03E-02	Radionuclide
1.74E-02 ± 1.87E-04	2.21E-02 ± 2.50E-04	3.01E-02± 4.18E-04	3.67E-02 ± 4.83E-04	4.36E-02 ± 8.62E-04	Energy (keV)
2.03E-02	2.48E-02	3.17E-02	4.05E-02	4.78E-02	Plant matrix
1.67E-01	1.24E-01	5.45E-02	1.04E-01	9.54E-02	Soil matrix

Radionuclide	Energy (keV)	Plant matrix	Soil matrix	Radionuclide	Energy (keV)	Plant matrix	Soil matrix
Co-60	1173.2	1.18E-02 ± 1.26E-04	1.20E-02	1.31E-02	1.36E-02 ± 1.50E-04	1.65E-02	2.17E-01
Co-60	1332.5	1.06E-02 ± 1.13E-04	1.19E-02	1.24E-01	1.22E-02 ± 1.35E-04	1.59E-02	2.99E-01
Y-88	1836.12	8.12E-03 ± 8.54E-05	9.39E-03	1.56E-01	9.54E-03 ± 1.03E-04	1.24E-02	3.00E-01

III.3. Study of sample density effect on gamma energy efficiencies using MCNP5 model

Among the essential factors that affect the self-absorption factor in the analyzed sample are the sample's density, composition, the geometry of the source detector and the radionuclides' gamma energies. Samples with higher densities generally result an increased gamma-ray attenuation due to more frequent interactions between the gamma rays and the sample material, which means that a larger fraction of emitted gamma rays are absorbed within the sample, resulting in lower detected counts. On the other hand, samples with lower densities may exhibit lower self-absorption due to less interactions, allowing more gamma rays to escape and be detected by the detector [55]. In addition to sample density, the composition of the sample can also significantly impact the self-absorption factor. Different elements and compounds have varying attenuation properties for gamma radiation, which depend on factors such as their atomic number, mass density, and interaction cross-sections. Samples containing high atomic number elements or compounds, such as heavy metals present in soils, may exhibit higher self-absorption compared to samples with low atomic number elements or compounds, such as organic materials present in plants [64]. Furthermore, the geometry of the source detector relative to the sample can also affect the self-absorption factor. The distance between the gamma-ray source and the detector, as well as the relative orientations of the source, detector, and sample, can impact the path length of gamma rays through the sample, and therefore influence the self-absorption factor. The gamma energies of the radionuclides present in the sample also play a significant role in determining the self-absorption factor. Gamma rays with higher energies are generally less attenuated compared to lower energy gamma rays. Therefore, the energy of the gamma rays emitted by the radionuclides in the sample can impact the self-absorption factor, with higher energy gamma rays potentially experiencing lower self-absorption. For this purpose, the simulated model was used to imply the effect of varying the soil sample densities on the self-absorption factor through the determination of FEPEs [55] investigated the impact of the element composition in soil samples on the efficiencies of gamma energy peaks using the MCNP5 code. Bolivar et al [64] McMahon et al. (2004) [67], and Jodłowski et al. [68] discussed the influence of sample density in terms of gamma-ray energy. Figure 27 show that when analysing the soil sample with gamma-ray energy less than 150 keV, the material density effect of the sample should be taken into account. This is may be due to the fact that at low gamma energies, the higher the density, the less ability to pass through the sample material and be detected by the detector.

The Figure 28, show that higher sample densities result lead to higher attenuation and faster decrease in the self-absorption correction factor. Moreover, the self-absorption correction factor decreases faster for low-energy gamma-rays than for high-energy gamma-rays implies that low-energy gamma rays are more strongly attenuated or absorbed by the sample compared to high-energy gamma rays [55].

III.4. Determination of self-absorption correction factors using the developed model

Once the MCNP calibration efficiency is validated by the experimental measurement for plant and soil samples, it is able to use the simulated efficiencies for determining the self-absorption correction factors f. For this task, different simulations were performed for plant and soil matrices. The f was determined as the following equation [56]:

$$\varepsilon_{sim} = \varepsilon_{0\,sim} \times f \qquad (33)$$

Where $\varepsilon_{0\,sim}$ and ε_{sim} are the simulated FEPE of the reference sample and the simulated FEPE of the investigated soil or plant samples, respectively. The results of the self-absorption correction factor curves are shown in Figure 29. It can be observed that the effect of self-absorption is more evident at low gamma ray energies, especially in the soil matrix. For example, in the ^{241}Am, the FEPE is decreased by 36.7 % in soil sample and only by 1% in plant sample. Indeed, at low gamma energies, the ability to pass through the sample material in which it contains heavy elements with higher densities and be detected by a detector is difficult due to the many interactions with material atoms, which lead to the loss of energy before reaching the detector. However, at high gamma energies, the FEPE is reduced by only 5% in soil matrix, owing to the latter having a larger chance of escaping from the sample and attaining the detector [65-67].

This behavior can be attributed to the interaction mechanisms of gamma rays with matter. At lower energies, gamma rays are more likely to undergo photoelectric absorption or Compton scattering, where the gamma rays transfer energy to electrons in the sample, leading to their absorption or deflection. As a result, the self-absorption correction factor needs to be larger for low-energy gamma rays to account for the higher probability of absorption or scattering, hence it decreases faster. On the other hand, at higher energies, gamma rays are more likely to undergo pair production, where the gamma rays convert into an electron and a positron in the presence of a nucleus, or penetrate through the sample without any interaction. Pair production becomes the dominant interaction mechanism at higher energies, and the probability of absorption or scattering decreases, resulting in a slower decrease in the self-absorption correction factor.

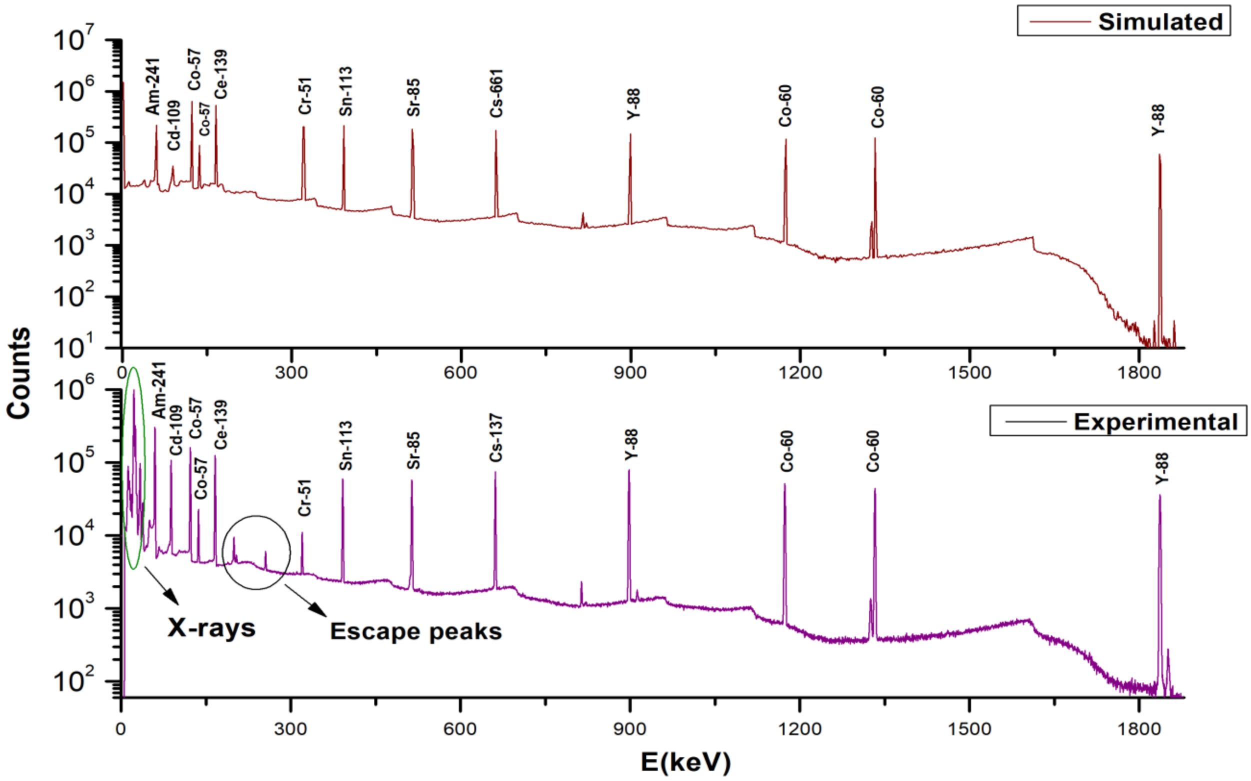

Figure 24. Simulated and Experimental Spectrums for the mixed standard solution in a cylindrical plant matrix.

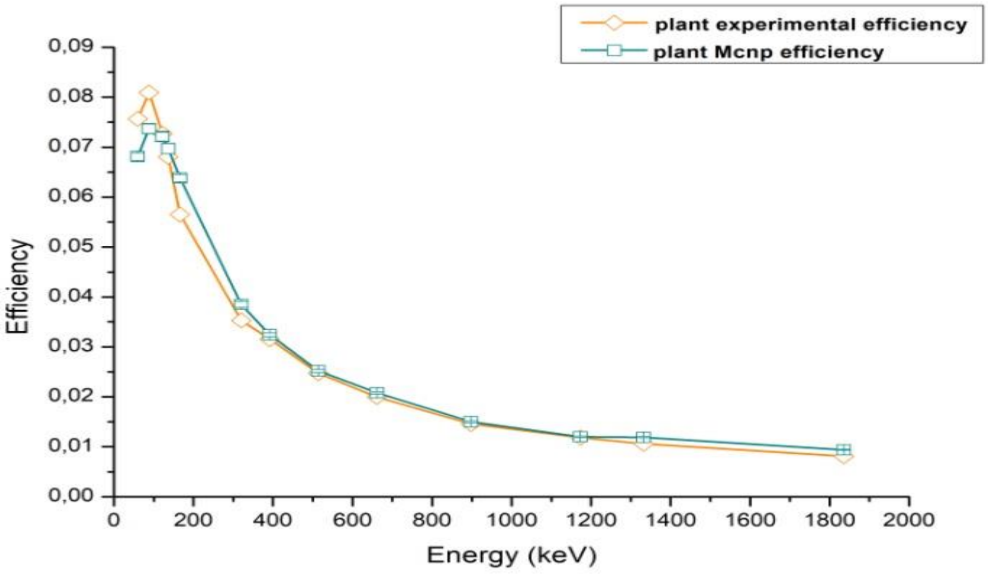

Figure 25. Experimental and simulated Efficiency curves for the plant matrix in a cylindrical geometry.

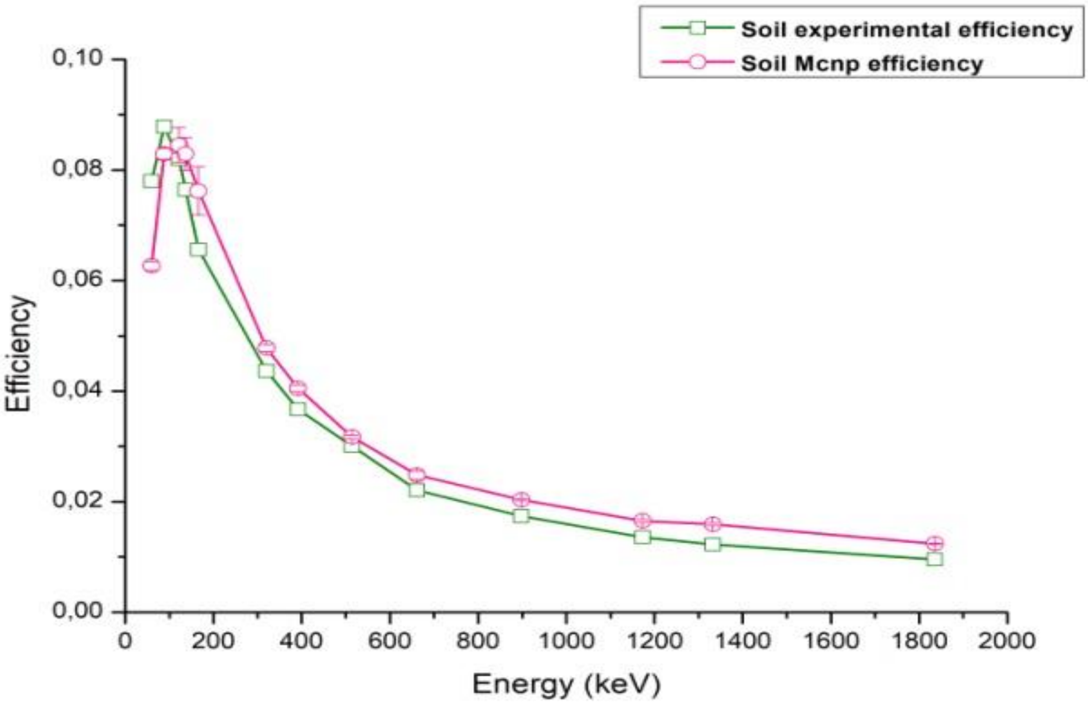

Figure 26. Experimental and simulated Efficiency curves for the soil matrix in a cylindrical geometry.

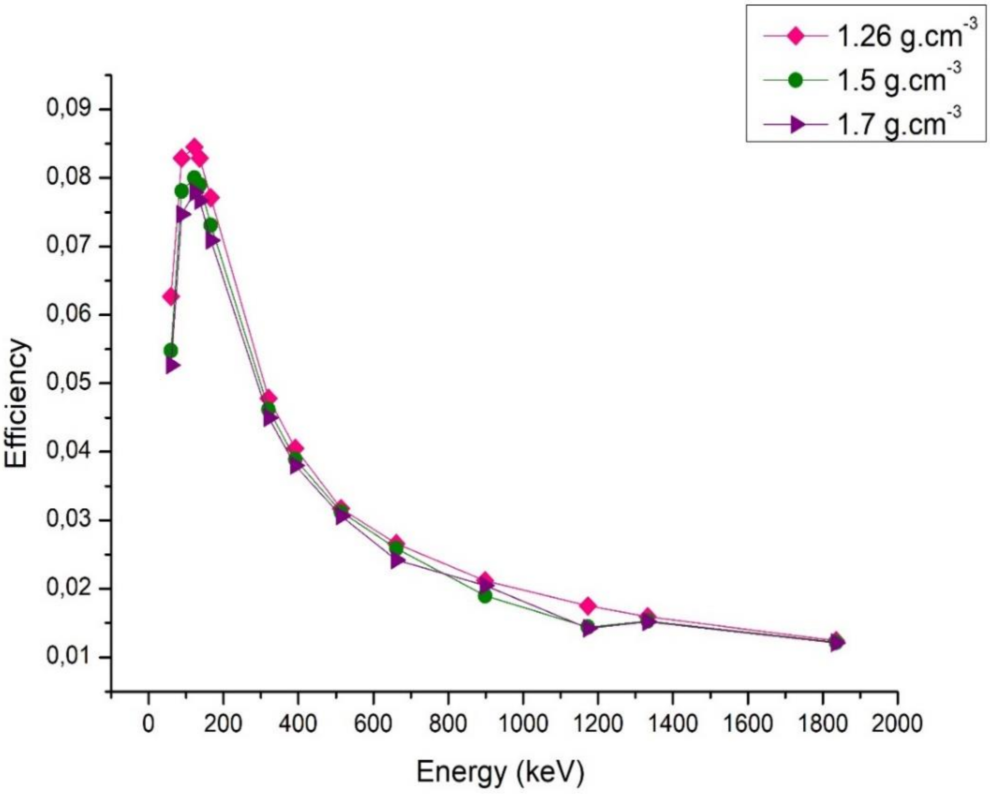

Figure 27. Simulated Efficiency curves for different soil densities.

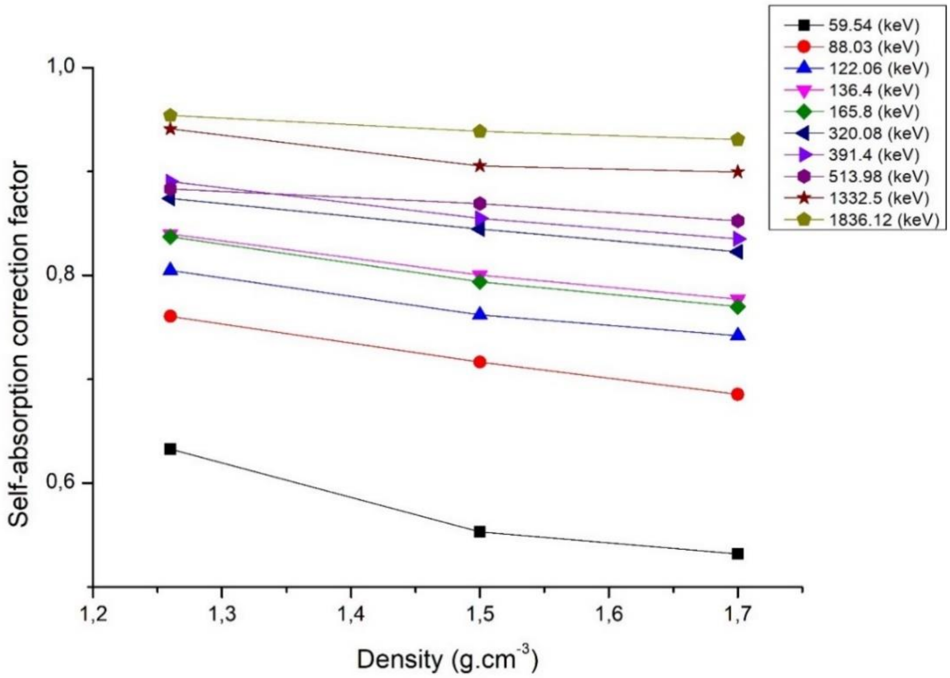

Figure 28. Variation of the self - absorption correction factor on the sample density (g/cm^3)

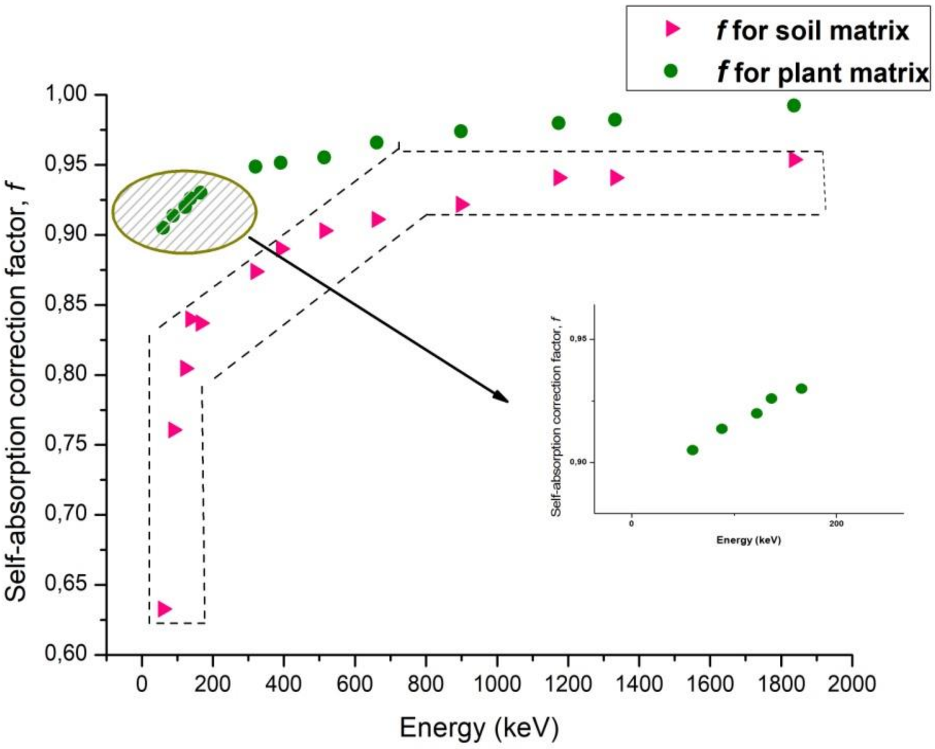

Figure 29. Variation of the self-absorption correction factor for soil and plant matrices according to reference sample calculated by the MCNP5.

III.5. XRF results

The Table 9 and Table 10 show the elemental characterization results of various types of crops with their corresponding soils using XRF (X-ray fluorescence) technique. The values given in the tables are the concentration and standard deviation of the measurements taken for each element from the studied samples, expressed in units of parts per million (ppm).

For the soil samples, the concentrations of Cr in the studied soil are above the recommended levels (12-83 ppm) [69]. The concentrations of Mn, Ni, Cu and Zn in artichoke/fennel soil and mushroom soil are also higher than the permissible limits. The remain concentration are below the standard limits [69].

For the crop samples, it is noticed higher values of Fe in mushroom, mustard and onion, and high levels of Cu and Zn in mushroom. These values are above the permissible limit standard [69,70].

Element	Concentration (ppm)					
	Bean	**Artichoke/fennel**	**Bean**	**Mushroom**	**Bean**	**Onion**
Rb	54.40 ± 2.97	73.54 ±3.99	54.84 ±2.99	72.49 ± 3.93	50.36 ± 2.76	43.92 ± 2.42
Sr	253.88± 13.41	89.11 ± 4.75	254.08 ± 13.42	86.59 ± 4.62	174.68 ± 9.25	266.94 ± 14.10
Zr	147.96 ±12.25	165.15 ± 13.66	148.41 ± 12.29	176.75 ± 14.62	225.23 ± 18.63	141.84 ± 11.74
Nb	9.83 ± 0.43	12.00 ± 0.50	8.72 ± 0.39	11.13 ± 0.47	8.61 ± 0.39	8.96 ± 0.40
Pb	15.17 ± 1.22	38.50 ± 2.39	16.38 ± 1.26	39.79 ± 2.45	17.82 ± 1.31	14.22 ± 1.15
Na	2463.98± 249.07	2456.67± 276.38	2804.92± 269.79	2199.27 ± 223.43	2850.34± 307.31	2827.63 ± 271.33
Mg	1797.53 ± 219.82	2457.27 ± 297.15	2650.45± 270.85	2762.50 ± 274.11	2503.64± 305.42	2360.68 ± 251.76
Al	41679.90 ± 625.76	55654.29 ± 854.08	43597.49± 646.68	52118.82 ± 755.37	38990.75± 644.07	41021.27 ± 612.57
Si	176277.09 ± 332.96	217350.30± 454.66	176546.50± 332.19	207903.20± 374.82	178477.81± 397.37	165040.31± 316.22
P	2231.42 ± 511.82	2598.36 ± 598.11	2602.15± 596.08	2519.23 ± 577.19	5519.37± 1262.73	3086.85 ± 706.53
S	1515.49 ± 16.91	1059.38 ± 17.04	1274.62 ± 14.88	1082.25 ± 13.38	1471.30 ± 20.02	1552.96 ± 17.21
K	19700.03 ± 56.80	13630.49 ± 42.78	19933.61± 56.86	12870.61 ± 40.94	16637.61± 49.11	16002.26 ± 48.01
Ca	95173.75 ± 212.02	8158.76 ± 23.58	90881.56± 202.05	8511.31 ± 24.35	69166.55± 156.61	103438.59± 229.26
Sc	44.05 ± 12.33	8.86 ± 2.55	30.03 ± 8.48	7.99 ± 2.31	\	25.33 ± 7.16
Fe	31072.26 ± 43.14	52729.22 ± 66.04	29519.01± 40.58	52853.04 ± 66.17	27803.11± 39.41	27654.24 ± 39.26
Co	7.65 ± 0.36	11.64 ± 0.53	7.76 ± 0.36	10.85 ± 0.50	7.20 ± 0.34	7.12 ± 0.34
Ni	32.40 ± 7.82	46.68 ± 11.24	26.26 ± 6.35	46.70 ± 11.24	29.24 ± 7.06	24.43 ± 5.92
Cu	17.77 ± 1.48	139.10 ± 10.91	15.91 ± 1.33	141.63 ± 11.10	18.83 ± 1.56	12.51 ± 1.07
Zn	65.65 ± 3.46	161.20 ± 8.37	65.98 ± 3.47	159.99 ± 8.31	88.86 ± 4.65	68.89 ± 3.62
Ga	4.23 ± 0.16	5.40 ± 0.18	3.76 ± 0.14	4.98 ± 0.18	3.16 ± 0.14	3.58 ± 0.14
Ti	3633.59 ± 14.50	5368.99 ± 19.73	3501.92 ± 13.98	5313.49 ± 19.54	3366.17 ± 13.61	3289.56 ± 13.38
V	92.74 ± 13.74	164.24 ± 23.78	81.69 ± 12.20	163.53 ± 23.68	81.11 ± 12.11	84.56 ± 12.57
Cr	102.05 ± 9.53	177.76 ± 16.50	93.93 ± 8.78	177.15 ± 16.44	95.80 ± 8.95	83.29 ± 7.80
Mn	399.34 ± 24.79	803.99 ± 49.82	409.18 ± 25.40	753.66 ± 46.70	391.64 ± 24.31	328.51 ± 20.41

Table 9. Concentration of elements in soil samples using XRF technique.

Element	Concentration (ppm)						
	Bean	**Fennel**	**Artichoke**	**Garlic**	**Mushroom**	**mustard**	**Onion**
Br	11.43 ± 0.37	51.24 ± 0.69	120.60 ± 1.05	10.25 ±0.38	120.60 ± 0.62	42.31 ± 0.64	20.20 ± 0.47
Rb	3.00 ± 0.27	6.90 ± 0.51	6.66 ± 0.53	3.77 ± 0.32	5.22 ± 0.41	5.28 ± 0.42	2.58 ± 0.26
Sr	277.48 ± 2.63	28.11 ± 0.48	55.77 ± 0.75	133.39 ± 1.42	9.16 ± 0.28	83.76 ± 0.99	108.10 ± 1.20
Na	179.50 ± 4.99	193.56 ± 5.85	376.11 ± 10.76	117.61 ± 3.26	82.92 ± 2.33	125.11 ± 4.09	113.93 ± 3.82
Mg	12498.87± 1216.61	20952.80 ±2121.78	25671.91± 2596.47	14656.17± 1366.46	11298.87 ± 1070.25	8777.52 ± 1236.51	9721.34± 1283.86
Al	483.68 ± 32.06	691.49 ± 2.62	310.23 ± 27.56	83.07 ± 5.83	106.29 ±20.92	206.90 ± 20.64	121.09 ± 17.75
P	2157.53 ± 39.25	3500.047 ± 9.99	5587.28 ± 93.25	2329.85 ± 38.20	14879.43 ± 244.04	3548.08 ± 61.82	2378.88 ± 42.07
S	6236.26 ± 17.28	5437.39 ± 4.69	5100.73 ± 13.82	7604.90 ± 14.02	7654.30 ± 20.85	6356.73 ± 17.48	5852.033 ± 15.284
K	10573.95± 190.42	19436.37 ± 49.57	16733.99± 301.01	19933.29 ± 358.48	36545.52 ± 656.74	15293.76 ± 275.15	20831.23 ± 374.61
Ca	35319.45± 386.07	17929.24 ± 96.32	11499.40± 126.07	9981.04 ± 109.62	2670.32 ± 30.00	9698.98 ± 106.44	14353.21 ± 157.31
Fe	256.38 ± 3.97	469.36 ± 6.79	342.10± 5.10	269.23 ± 4.13	1206.46 ± 16.63	1733.90 ± 23.68	628.87 ± 8.92
Co	0.32 ± 0.08	0.51 ± 0.10	0.53 ± 0.10	0.34 ± 0.08	1.56 ± 0.23	1.77 ± 0.26	0.67 ± 0.12
Ni	0.71 ± 0.17	1.06 ± 0.18	0.92 ± 0.17	0.90 ± 0.18	0.87 ± 0.17	7.47 ± 0.80	0.97 ± 0.17
Cu	15.17 ± 0.88	14.22 ± 0.82	15.32 ± 0.89	7.22 ± 0.46	103.20 ± 5.64	7.54 ± 0.47	6.67 ± 0.42
Zn	25.74 ± 0.66	59.86 ± 1.38	56.32 ± 1.30	29.67 ± 0.74	184.22 ± 4.05	59.29 ± 1.36	28.71 ± 0.71
V	2.69 ± 2.43	1.98 ± 1.84	0.46 ± 0.75	1.63 ± 1.55	4.26 ± 3.77	6.75 ± 5.92	3.40 ± 3.03
Mn	24.11 ± 0.86	95.42 ± 2.87	32.71 ± 1.09	27.02 ± 0.96	56.58 ± 1.75	59.47 ± 1.83	41.97 ± 1.34
Cl	14085.53± 67.42	21252.42±97.33	40072.12± 172.26	5373.34 ± 33.19	3097.22 ± 23.24	7954.21 ± 42.74	7030.64 ± 39.95

Table 10. Concentration of elements in plant samples using XRF technique

Chapter IV: Environmental applications

IV.1 Soil to plant transfer factor application

Human beings are continuously exposed to a variety of radiation types, originated from primordial cosmic-rays formed in the upper atmosphere layer, radiation gases released from the ground surface present a continuous radioactive background of the earth, natural decay series radionuclides like the uranium and thorium decay chains together with radioactive potassium, and the artificial radionuclides ^{137}Cs and ^{7}Be. These long-lived radionuclides are transferred from the soil to food crops during the mineral uptake, and then get ingested by human body [71]. Thus, the assessment of radionuclides in farmlands agricultural areas is of significant concern in radiological analysis. The uptake of the environmental radionuclides from soil to plants is determined by transfer factor of various radionuclides from soil to plant which referred to the ratio of the activity concentration in soil and plants. TF is of great importance for prediction the concentration of radionuclides accumulates in plants and studying the impact of contamination in surrounding environment requires a great deal of research work. However, TF data for a given radionuclide vary from plant to another and strongly affected by the soil physical and chemical characteristics and properties such as texture, pH, organic matter, exchangeable potassium and calcium matter content, the radiotracers behavior in soil and plant, and the environmental changes [72]. The knowledge of the TF in the developing countries is constrained [14]. Algeria is one among developing countries that has no any data about the transfer mechanism from soil to plant/crop and has no any information the amount of phosphate fertilizer used in farmlands.

For this purpose, several vegetables (artichoke, fennel, mustard, beans, garlic and onion) were collected from different regions in Algeria in order to estimate the soil to plant transfer factors, provide a baseline data and enlarge the information about radioactivity in soil and crops in the studied areas which are not available yet. The TF was determined from the calculation of the ratio of the activity concentrations of the radionuclides ^{226}Ra, ^{232}Th,^{40}K and ^{137}Cs. their comparison with the literature data.

1.1 Mobility of environmental radionuclides in the Soil

Natural radionuclides, such as thorium, potassium and radium, and the artificial like ^{137}Cs exist in varying concentrations in soil, plant and water. Their mobility in soil is complex and depends on numerous factors, including the solubility of radionuclides depends on their chemical properties, such as their ionic charge, the physical and chemical properties of the soil, the environmental conditions and the radionuclides adsorption into soil particles, in which it can be adsorbed into soil particles through several mechanisms like cation exchange and surface complexation. The degree of adsorption depends on radionuclide and soil characteristics. For example, potassium is present in the soil in both soluble and insoluble forms. It is generally considered to be mobile in most soils and can be easily uptake by plants. Thorium is generally less mobile than potassium and radium appears in the soils in very low concentrations. It is generally less mobile than potassium and thorium due to its low solubility and strong adsorption into soil particles. The ^{137}Cs becomes strongly adsorbed to soil particles and it can become relatively immobile. The mobility of natural radionuclides can also be affected by human activities, such as mining or the use of fertilizers. In agricultural areas, it is important to monitor soil and crops to ensure that these radionuclides are affecting human health [73].

1.2 Radionuclides soil-plant transfer factor mechanism

Soil-to-plant transfer factors (TFs) play an essential role in assessing the movement of contaminants from soil into plants**.** The processes of material absorption, translocation, and accumulation from soil into plant tissues are some of the mechanisms behind this transfer. Nutrients and pollutants from the soil are absorbed by plants through their roots. This process entails the absorption of materials that are either present as ions or dissolved in soil water [1].

Translocation: Substances pass via vascular tissues inside the plant after being absorbed. They can be transported to different parts of the plant such as leaves, fruits, or roots.

Accumulation: Substances accumulated in plant tissues can undergo various transformations or remain in their original form. The concentration of contaminants in different plant parts can vary based on factors like plant species, soil properties, and environmental conditions.

1.3 Crops characteristics used in research study

The reason for choosing these types of crops mustard, artichoke, fennel, onion, garlic, bean and mushroom to study is because these crops are commonly consumed by the Algerian population, and are therefore an important part of their diet. Another reason, is their ability to uptake different radionuclides and heavy metals from soil, produced through natural processes or as a result of human activities.

Salem Djedidi et al. [74] conducted a study to investigate the effectiveness of Indian mustard in removing radioactive cesium from contaminated soil. They found that the amount of radio-cesium removed from the soil was significantly higher in Indian mustard crops compared to other crop species.

Deepshekha Punetha et al., [75] proved that fennel was able to grow in contaminated soils and showed potential for phytoremediation, which is the process of using plants to remove pollutants from soil water, or air. The findings showed that fennel was able to accumulate high levels of cadmium and lead in its roots, and leaves, indicating that it has the ability to remove these heavy metals from the soil.

Satoshi Yoshida et al., [76] investigated the uptake of uranium by several crops, including artichokes, in soil contaminated with uranium. They found that artichokes had a higher Transfer Factor (TF) for uranium compared to other crops.

The Sajida Perveen et al., [77] The study involved collecting samples of onion and garlic plants from various locations and analyzing them for heavy metal content. The results showed that both onion and garlic plants had accumulated significant amounts of heavy metals such as lead, cadmium, nickel, and chromium.

Several studies [77-80] have investigated the accumulation of heavy metals in mushrooms and have found that mushrooms tend to accumulate high amounts of heavy metals compared to other crops.

1.4 Soil-to crop transfer factors determination

The Soil to plant transfer factor (TF) is a valuable parameter widely used for environmental impact assessment, particularly for evaluating the potential impact of contaminants such as heavy metals, radionuclides, and organic pollutants in crops and agricultural products [81]. It is the most important indicator of the radionuclides uptake from soil to agricultural crops because it determines the level of radionuclide contamination in crops grown on contaminated soils, and thus plays a critical role in assessing dose intake by human body. When radionuclides are taken up by crops, they can accumulate in the edible parts of the plant, such as the leaves, stems, and fruits, and may pose a risk to human health if they consumed. The TF varies considerably, depending on several factors such as the radionuclide properties, soil characteristics, and plant species [82].

In some countries, notably in developing countries, knowledge of Transfer Factor is still limited [14,83,84]. Thus, the determination of TF in Algeria is critical for several reasons. Firstly, Algeria has a significant agricultural sector, and many crops are grown on soils that may be contaminated with radionuclides from various sources such as mining activities, industrial processes, or nuclear accidents. Secondly, Algeria has a limited regulatory framework for environmental radiation protection and monitoring, and there is a lack of comprehensive data on the extent and distribution of radionuclides in the environment. Accurate measurement of TFs can help to identify areas where contamination may be a concern and support the development of appropriate monitoring and remediation strategies.

The TF can be determined by the following equation [85]:

$$\text{TF} = \frac{Activity\ of\ radinuclides\ in\ plant\ (\ dry\ weight)}{Activty\ of\ radionuclides\ in\ soil\ (\ dry\ weight)} \quad (34)$$

1.5 Radiological indices estimation

Radium equivalent activity (Ra_{eq})

The equivalent radium activity (Ra $_{eq}$), is a parameter determined by the measurements of the environmental radionuclides ^{226}Ra (^{238}U), ^{232}Th and ^{40}K that evaluate the external exposure originated by gamma-ray emitters. The Ra $_{eq}$ is calculated as follows:

$$Ra_{eq} = A_{Ra} + 1.43A_{Th} + 0.077A_K \quad (35)$$

Where A_{Ra} is the activity concentration of ^{226}Ra in Bq kg^{-1}, A_{Th} is the activity concentration of ^{232}Th in Bq kg^{-1} and A_K is the activity concentration of ^{40}K in Bq kg^{-1}.

Internal Hazard Index (Hint)

It is used to speculate the level of gamma radiation hazard associated with the natural radionuclides in the measured samples.

$$H_{int} = \frac{A_{Ra}}{159} + \frac{A_{Th}}{259} + \frac{A_K}{4810} \leq 1 \quad (36)$$

Absorbed dose rate (Dγ)

The absorption radiation dose in outdoor air at 1 m above the ground for the collected samples is calculated using the following expression:

$$D\boldsymbol{\gamma}\ (nGy\ h^{-1}) = 0.462A_{Ra} + 0.621A_{Th} + 0.0417A_K \quad (37)$$

Where A_{Ra}, A_{Th}, and A_K are the specific activities of ^{226}Ra, ^{232}Th, and ^{40}K, respectively.

Annual effective dose equivalent (AEDE)

The annual effective dose rate is measured using the conversion coefficient from the absorbed dose in the air to the effective dose for adults (0.7 Sv·Gy^{-1}) with the outdoor occupancy factor (0.2), and the indoor occupancy factor (0.8) given by [86]:

$$AEDE(mSv\ y^{-1}) = D_{\boldsymbol{\gamma}} \times 8760 \times 0.7 \times 0.2\ \times 10^{-6} \quad (38)$$

Annual gonadal dose equivalent (AGDE)

The annual gonadal dose equivalent is measured using the activity concentrations of ^{226}Ra, ^{232}Th, and ^{40}K as the following [86]:

$$AGDE(\mu Sv\, y^{-1}) = 3.09A_{Ra} + 4.18A_{Th} + 0.314A_{K} \qquad (39)$$

1.6 Samples collection and preparation

Fourteen (14) samples of crop and soil (7 crop samples and 7 soil samples) were collected from four sites located in the middle east of Algeria, namely Artichoke, fennel, mustard, onion, bean and garlic. The samples were collected into polyethylene bags, prepared and analyzed at the laboratory of the Nuclear Research Center of Algiers (CRNA). The crop samples were washed by water to remove any surface contamination, then chopped into small pieces and oven dried with the soil samples at 65°C for 24 hours to ensure moisture was completely removed. The dried samples were ground using a stainless-steel grinder and sieved through a pore size of 2mm to remove stones. The final samples were sealed with tape in cylindrical containers and kept for 35 days to reach the secular equilibrium between parents and daughter radionuclides ^{226}Ra to ^{222}Rn and ^{232}Th to ^{228}Ac [86]. All the crops were being harvested at maturity. The choice of the sites is owing to their high-density population (Figure 30).

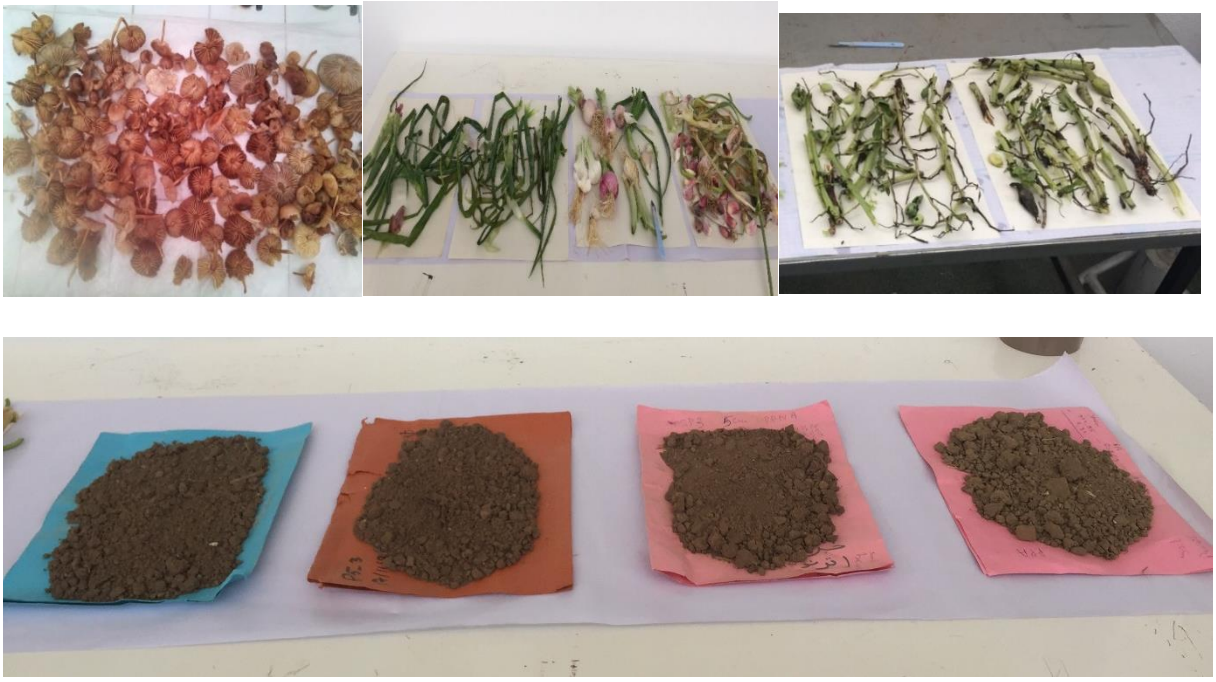

Figure 30. Some crop samples with their corresponding soils

1.7 Radioactivity concentration measurements

In this part, the developed MC model was applied for the calculation of the specific activities of the natural radionuclides ^{226}Ra, ^{232}Th and ^{40}K using the resulting efficiencies obtained from the simulated FEPE curves and the number of counts found by the measurement of each sample for 24h. The radionuclides specific activities were determined as the following [87]:

$$A = \frac{N}{\varepsilon_{sim}.I_{\gamma}.t_c.m} \qquad (40)$$

Where ε_{sim} is the detector simulated efficiency, m is the sample weight (kg) N, I_{γ} and t_c were defined in the equation (31).

The specific activities in the soil samples of ^{40}K, ^{232}Th and ^{226}Ra varied from 284.19 ± 5.31Bq kg^{-1} to 318.99 ± 6.42 Bq kg^{-1}, 15.20 ± 0.46 Bq kg^{-1} to 25.50 ± 0.74 Bq kg^{-1} and 10.20 ± 0.30 Bq kg^{-1} to 14.40 ± 0.41 Bq kg^{-1}, respectively.

In crop samples, the specific activity concentrations were found between 330.14 ± 7.37 Bq kg^{-1} to 444.19 ± 10.40 Bq kg^{-1} for ^{40}K, 0.43±0.08 Bq kg^{-1}to 0.38 ± 0.05 Bq kg^{-1} for ^{232}Th and 1.18 ± 0.14 Bq kg^{-1}to 3.50 ± 0.30 Bq kg^{-1} for ^{226}Ra.

The ^{232}Th in crops presented the lowest activity concentration compared with the ^{226}Ra and ^{40}K activity concentrations and it was below the limit of detection in fennel crop, this probably because thorium is considered as an immobile element with a lower generic geometric mean, which results a low uptake by crops [88]. The higher values of ^{40}K in crops could be explained by the high accumulation of potassium in crop samples since potassium is a necessary nutrient for plants [87-90]. The results are presented in Table 11 and Table 12. All the samples specific activity are below the worldwide average except the specific activity of ^{40}K which was higher than the global limits [86].

Crops	**Mean specific activity (Bq kg^{-1})**			Ra_{eq}**(Bq kg^{-1})**	D_{γ} **(nGy h^{-1})**	H_{int}	**AEDE (µSv/y)**	**AGDE (µSv/y)**
	^{40}K	**^{232} Th**	**^{226}Ra**					
Mustard	330.14 ± 7.37	0.43±0.08	1.18 ± 0.14	27.2	14.57	1.09E-01	1.79E-02	1.09E+02
Artichoke	433.99 ± 9.38	0.38±0.05	2.75 ± 0.22	36.7	19.60	7.77E-02	2.40E-02	1.46E+02
Fennel	444.19± 10.40	**<DL**	3.50 ± 0.30	37.7	20.13	1.14E-01	2.47E-02	1.50E+02
Onion	663 ± 22.00	0.79 ± 0.27	3.12 ± 0.48	54.2	2.91E+01	1.60E-01	3.57E-02	2,21E+02
Bean	461 ± 22.00	2.38 ± 0.34	7.23 ± 1.60	42.73	2.26E+01	1.51E-01	2.77E-02	1,77E+02
Garlic	609 ± 22.40	0.75 ± 0.12	1.15 ± 0.19	48.04	2.59E+01	1.37E-01	3.18E-02	1,98E+02
Mushroom	949±16	0.23±0.046	1.60± 0.19	74.7	4.03E+01	0.21	4.95E-02	3.04E+02

DL: detection limit, DL= 2.71+4.65$\sqrt{B}$. Where B is the background at the region of interest.

Table 11. ^{226}Ra, ^{232}Th and ^{40}Kactivity concentrations, Radium equivalent (Ra_{eq}), Dγ, H_{int} AEDE, and AGDE for crops samples.

Soil	**Mean specific activity (Bq kg^{-1})**			Ra_{eq}**(Bq kg^{-1})**	D_{γ} **(nGy h^{-1})**	H_{int}	**AEDE(µSv/y)**	**AGDE (µSv/y)**
	^{40}K	**^{232}Th**	**^{226}Ra**					
Mustard	284.19 ± 5.31	15.20 ± 0.46	10.20 ± 0.30	53.82	26.00	1.82E-01	3.19E-02	1.84E+02
Artichoke/ Fennel	318.99 ± 6.42	25.50 ± 0.74	14.40 ± 0.41	75.42	35.79	2.55E-01	4.39E-02	2.51E+02
Onion	386 ± 11.7	22.9± 1.33	15.3± 0.77	77.77	37.4	2.65E-01	4.58E-02	3.65E+02
Bean	514 ± 15.2	99.3± 2.98	13.4± 1.07	194.98	89.3	5.75E-01	1.10E-01	2.64E+02
Garlic	572 ± 16.9	27.9± 1.76	20.1± 1.07	104.04	50.4	3.53E-01	6.19E-02	6.18E+02
Mushroom	532±9.52	36.9 ± 0.89	14.3± 0.43	108.03	51.71		6.34E-02	3.65E+02
World average (UNSCEAR-2000)	400	30	35	370	55	≤1	1	300

Table 12. ^{226}Ra, ^{232}Th and ^{40}Kactivity concentrations, Radium equivalent (Ra_{eq}), Dγ, H_{int} AEDE, and and AGDE for soil samples.

1.8 Radiation hazard indices

The radium equivalent activity (Ra_{eq}), the internal hazard index H_{int}, The absorbed dose rate ($D\gamma$) in air at 1 m above the ground, the annual effective dose equivalent (AEDE), and the annual gonadal dose equivalent (AGDE) parameters were calculated for crop and soil samples. The values of radium equivalent activity obtained ranged from 27.2 Bq $kg^{-1}$to 37.7 Bq kg^{-1} for crops and 53.8 Bq kg^{-1} to 75.4 Bq kg^{-1} for soil samples. The maximum absorbed dose rate D_{γ} values were found 35.79 nGy h^{-1} in soil samples and 37.7nGy h^{-1} in crop samples, which are lower than 55 Bq kg^{-1}. The maximum AEDE for both soil and crop samples was found much lower than 1 with the values of 0.0247 and 0.255 µSv/y for soil and crop samples, respectively. The H_{int} values in crop and soil samples were less than 1, varied from 0.078-0.114 for crops and 0.182-0.255 for soil samples. The annual gonadal dose equivalent (AGDE) values were found between 109-150 µSv/y in crops and 184- 251 µSv/yin soils. The results are listed in Table 10 for soil samples and Table 11 for crops samples. It can be clearly seen that all the parameter values are below the world averages.

1.9 Soil-plant Transfer factors

The soil-to-plant transfer factors for the ^{40}K were found to be very high in all the study samples in which the highest values were noticed in mushroom and onion samples. The higher uptake of ^{40}K by crops is may be due to the essential nutrient property of potassium to the plant [90]. The ^{226}Ra transfer factor varied from 0.014 to 0.53 in which the lowest value referred to garlic sample and the highest one referred to bean sample. The soil to plant transfer factors for ^{232}Th ranged from 0.006 to 0.034. The TF of ^{232}Th for the fennel and artichoke crops varied even though they were both harvested from the same soil. This could be attributed to biological heterogeneity in plants, crop types and species, the growing season, and root distribution characteristics [14] (See Figure 31).

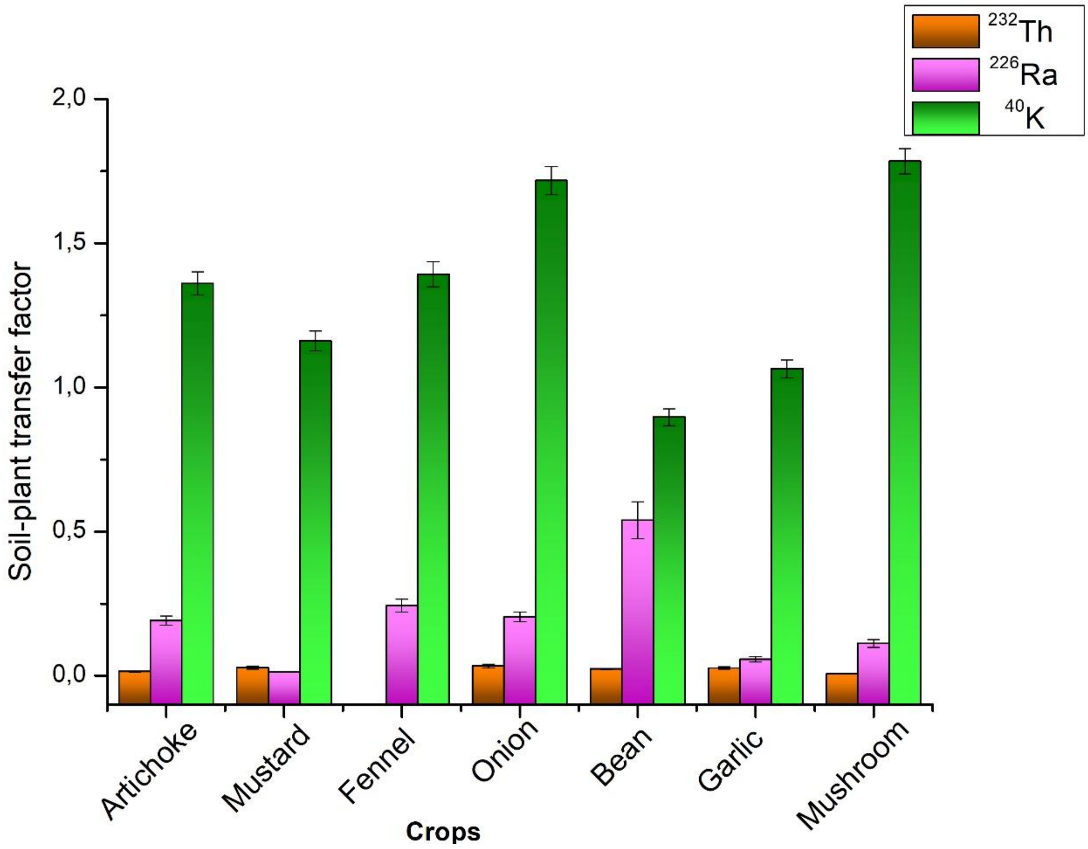

Figure 31. Transfer factor of artichoke, mustard and fennel samples.

1.10 Transfer of metals and trace elements

Accumulation of heavy metals in agriculture soils are derived from both natural and human sources. Natural sources include geological formations that can be found in various regions around the world like in volcanic eruptions, mountainous regions, and marine aerosols. However, it can be either come from human activities such as industrial processes, mining [91], cement-pollution, energy and fuel production [92]. Agricultural practices can also contribute in the accumulation of heavy metals such as the use of fertilizers, sewage sludges, pesticides, and irrigation water, particularly in areas with intensive agricultural production [93]. Numerous studies have been conducted to determine the extent of heavy metal contamination in soils and the potential risks to human health and the environment [94-97]. These studies have shown that heavy metal contamination is widespread and can have harmful effects on ecosystems, water quality, and human health. The uptake of heavy metals by plants has the potential to significantly infiltrate the food chain. The uptake process depends on several factors, such us the type of metal, its concentration in soil, plant species, and the properties of the soil. Around 90% of the overall amount of metal consumed by humans comes from food crops and the remaining 10% coming from skin interactions and breathing in contaminated dust [98]. Some metals and trace elements like zinc (Zn), copper (Cu) and manganese (Mn) are essential for plants growing animals and human beings, they can also be dangerous at high exposure levels and exposure to excessive amounts of these metals can lead to toxicity [99]. For example, excessive zinc in soil can cause stunted growth in plants, while high levels of copper can disrupt the uptake of other essential nutrients and damage plant tissues. In animals, excessive exposure to manganese can lead to neurological problems and impaired growth. Soil-plant transfer of metals and trace elements is an important aspect of environmental chemistry and toxicology. The transfer of metals and trace elements from soil to plant is typically quantified using a parameter called the transfer factor (TF), which is defined as the concentration of the metal or trace element in the plant divided by its concentration in the soil [99]. The TF can vary widely depending on the metal or trace element, the plant species, and the soil conditions. The aim of this part is to assess the kinetic of metals in soil by assessing their uptake by a range of plants.

1.11 Determination of the heavy metals transfer

The XRF results for the collected soil and crop samples showed the existence of some metal concentration like Cu, Mn, Ni, Zn, Co, V, Sr. The results are given in Table 13. The results indicate that the concentration of heavy metals in different plant species varies significantly. The bean crop shows a high concentration of Cu and Sr. The variation in heavy metal concentration in different plant species is likely due to several factors, such as the physicochemical properties of the soil, the type of plant, and the bioavailability of the heavy metals.

	Bean	Onion	Garlic
Cu	0.853 ± 0.086	0.533 ± 0.057	0.454 ±0.047
Mn	0.060 ± 0.004	0.127 ± 0.008	0.066 ± 0.004
Ni	0.027 ± 0.010	0.039 ± 0.012	0.034 ± 0.010
Zn	0.392 ± 0.022	0.416 ± 0.024	0.449 ± 0.026
Co	0.041 ± 0.011	0.094 ± 0.018	0.044 ± 0.011
V	0.029 ± N/A	0.040 ± N/A	0.020 ± N/A
S	4.115 ± 0.047	3.768 ± 0.042	5.966 ± 0.070
Sr	1.093 ± 0.058	0.404 ± 0.022	0.525 ± 0.028

N/A: Not available.

Table 13. Transfer of heavy metals

Fennel	Artichoke	Mustard	Mushroom
0.102 ± N/A	0.110 ± 0.011	0.401 ± 0.041	0.728 ± 0.069
0.118 ± 0.008	0.041 ± 0.002	0.151 ± 0.010	0.075 ± 0.005
0.022 ± 0.006	0.019 ± 0.006	0.255 ± 0.067	0.018 ± 0.005
0.371 ± 0.021	0.349 ± 0.019	0.667 ± 0.038	1.151 ± 0.065
0.044 ± 0.009	0.045 ± 0.009	0.247 ± 0.039	0.144 ± 0.023
0.012 ± N/A	0.002 ± N/A	0.083 ± N/A	0.026 ± N/A
5.132 ± 0.083	4.814 ± 0.078	4.320 ± 0.059	7.072 ± 0.089
1.315± 0.017	0.625 ± 0.034	0.479 ± 0.026	0.106 ± 0.006

1.12 Variation of transfer factors in function of the activity concentrations of radionuclides in soil

After performing a regression analysis, a non-linear relationship was observed between the TF and the activity concentrations of soil samples for the studied radionuclides (Figure 32-34) [100]. The results show that the soil to plant transfer factor for ^{226}Ra and ^{232}Th increased with the increase of the activities of soil samples with a significant positive correlation coefficient (R=0.58) (Figure 32, Figure 33). However, the TF for ^{40}K decreased with the increase of the specific activities of its soil samples with a negative correlation coefficient (R=-0.27) (Figure 34).

The research results show that the soil to plant transfer factor is inversely proportional to the soil samples activity concentration [100]. This is might be due to: the plant properties and species, the soil characteristics (the type of soil, pH value, organic content, moisture of the soil, calcium content) and the climate [101-104].

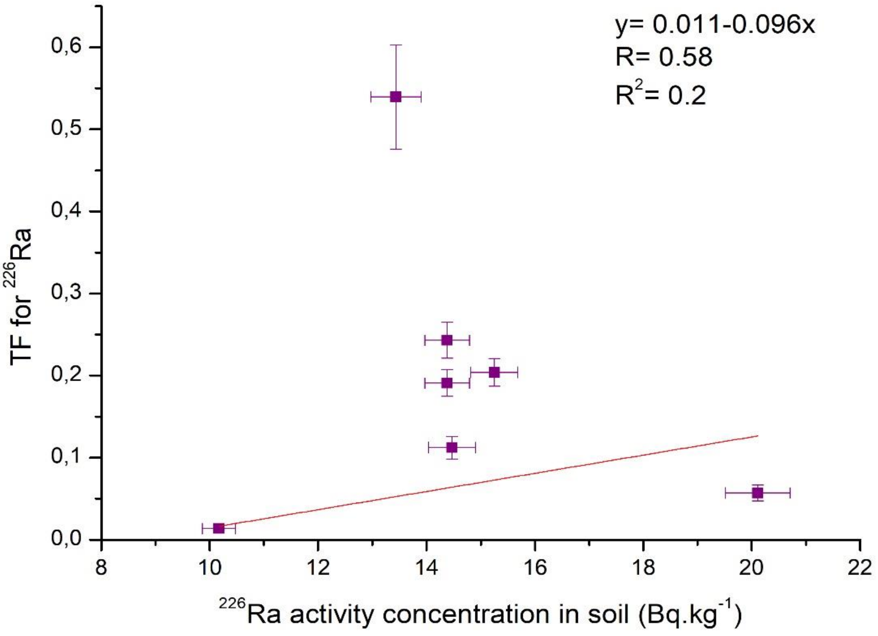

Figure 32. Soil-to-plant transfer factor negatively correlated with activity concentration of ^{226}Ra in soil.

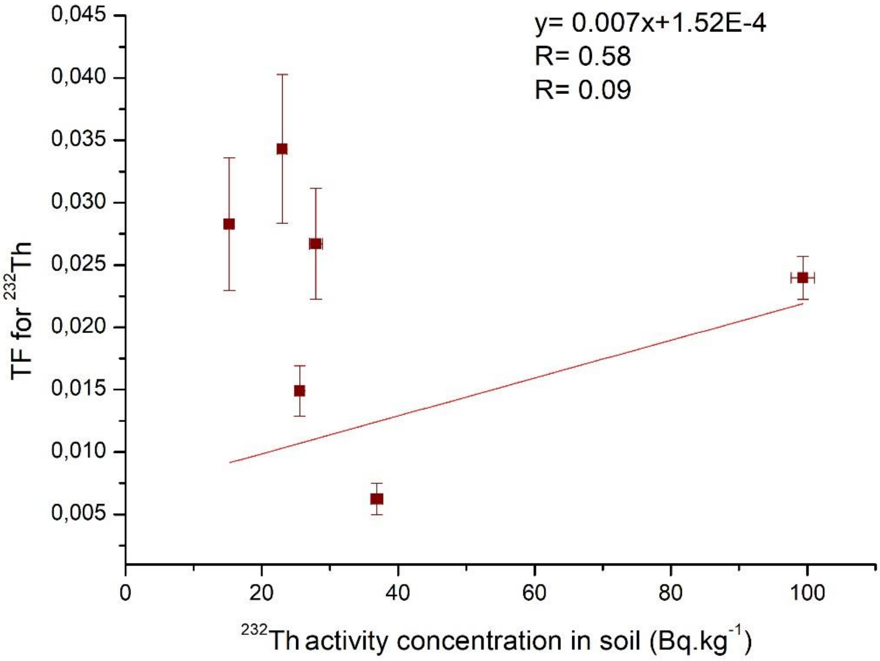

Figure 33. Soil-to-plant transfer factor negatively correlated with activity concentration of ^{232}Th in soil.

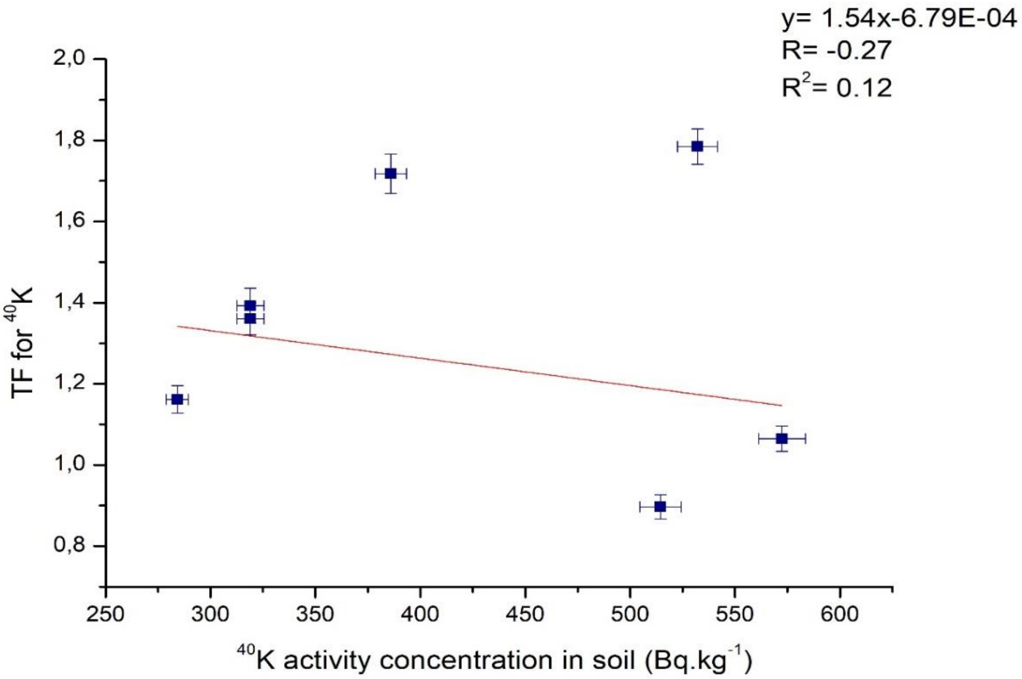

Figure 34. Soil-to-plant transfer factor negatively correlated with activity concentration of ^{40}K in soil.

IV.2 Absorbed fraction by plant for the erosion correction models

2.1 Theoretical models for cultivated soils used in erosion estimation

Soil erosion is a natural or human-induced process in which the top layer of soil is detached, transported, and deposited. The geomorphological processes with the strongest evidence that degrade soil are those caused by wind and water erosion. Water erosion occurs when rainfall or water runoff carries away soil particles. It can be classified into sheet erosion, rill erosion, and gully erosion. Wind erosion can carry away loose soil particles, especially in arid and semi-arid regions. This type of erosion is often seen in deserts or improperly managed agricultural areas. Soil erosion has serious effects for the global environment, including agricultural productivity, water quality, and ecosystem health, making it crucial to study, quantify and implement effective erosion control measures and sustainable land management practices [104,105].

Soil erosion can be studied using various methods including erosion modeling to estimate erosion rates based on factors like rainfall, sediment traps to measure erosion rates directly and the use of fallout radionuclides is called the Fallout Radionuclide (FRNs) Technique. This technique uses the measurement of the specific radionuclide activities deposited in the soil surface. Fallout radionuclides such as ^{137}Cs, ^{210}Pb and ^{7}Be, have proven to be very powerful tracers of soil movements, that can complement interestingly more conventional approaches and therefore, to assess soil erosion magnitude in agricultural land [106,107], in which numerous studies conducted during the last 50 years have been successfully used FRNs to quantify erosion rates and understand erosion dynamics [107-114].

The FRNs are deposited into the land surface through atmospheric fallout. It is presumed that this deposition is spatially uniform, at least within a relatively small region. As these radionuclides swiftly adsorbed by fine soil particles, they tend to accumulate at uppermost soil layer through physical processes (Figure 35). By documenting the subsequent redistribution of these radioactive tracers, which migrate across the landscape in association with soil or sediment particles primarily through physical processes, it becomes possible to effectively trace the rates and patterns of erosion and deposition within agricultural environments [105].

The conversion of FRN inventories into reliable quantitative estimates of soil redistribution presents a prominent challenge when it comes the use the FRN as soil tracers [110]. For this reason, the scientific community has proposed various conversion models for quantifying erosion rates using Fallout Radionuclides (FRNs). These models differ primarily in their assumptions regarding soil stratification and descriptions of FRN transport processes. The International Atomic Energy Agency (IAEA) has acknowledged the existence of these different models [109]. Among the available models for cultivated soils, there are:

2.1.1 Proportional Model:

The proportional model is advantageous due to its simplicity and easy application, relying on plough depth and ^{137}Cs inventory data. However, it oversimplifies the accumulation of ^{137}Cs in soil and fails to consider certain factors. If surface-accumulated ^{137}Cs is eroded before incorporation, the model overestimates soil loss rates. Conversely, the model underestimates soil loss rates by neglecting the dilution of ^{137}Cs within the plough layer caused by the incorporation of soil from below the original plough depth after erosion-induced surface lowering [112]. This model is described by the following equation [113]:

$$Y = 10\frac{BdX}{100TP} \qquad (41)$$

Y: Annual soil loss (t ha^{-1} yr^{-1});

d: depth of plough or cultivation layer (m);

B: bulk density of soil (kg m^{-3});

X: percentage reduction in total ^{137}Cs inventory (defined as $(A_{ref}\text{-}A)/A_{ref}\times 100$);

A_{ref}: local ^{137}Cs reference inventory (Bq m^{-2});

A= measured total ^{137}Cs inventory at the sampling point (Bq m^{-2});

T: time elapsed since initiation of ^{137}Cs accumulation (yr);

P= particle size correction factor.

2.1.2 Simplified Mass Balance Model (Mass Balance Model 1):

The Simplified Mass Balance Model addresses the progressive reduction in the ^{137}Cs concentration within the plough layer caused by the incorporation of soil from below the original plough depth, making it an improvement over the proportional model. This model is user-friendly and only requires information on plough depth. However, it does not consider the potential removal of recently deposited ^{137}Cs fallout before its incorporation into the plough layer through cultivation, which can happen during rainfall events that generate surface runoff and erosion. Additionally, the assumption that the total ^{137}Cs fallout input occurred in 1963 is an oversimplification, as fallout deposition can vary over time [109]. The model is described by the following equation [109]:

$$Y = \frac{10dB}{P}[1 - (1 - \frac{X}{100})^{1/(t-1963)}] \qquad (42)$$

Y= mean annual soil loss (t ha^{-1} yr^{-1});

d= depth of plough or cultivation layer (m);

B= bulk density of soil (kg m^{-3});

X= percentage reduction in total ^{137}Cs inventory (defined as $(A_{ref}\text{-}A)/A_{ref}\times 100$);

P= particle size correction factor;

2.1.3 Mass Balance improved model (Mass balance 2):

The mass balance model 2 takes account of both temporal variation of the ^{137}Cs fallout input and its initial distribution in the surface soil. The results issued from this model are likely to be more realistic than the those provided by the simplified mass balance model 1 presented in the previous section. However, the information on plough depth, relaxation mass depth H and parameter γ is required in order to use this model [109]. The cumulative ^{137}Cs activity can be calculated by [109]:

$$A(t) = A(t_0)e^{-\left(\frac{PR}{d+\lambda}\right)(t-t_0)} + \int_{t_0}^{t}(1 - P\gamma(1 - e^{\frac{R}{H}})I(t')(1 - e^{-\left(\frac{PR}{d+\lambda}\right)(t-t')}dt') \quad (43)$$

$A(t)$= cumulative ^{137}Cs activity per unit area (Bq m^{-2});

R= erosion rate (kg m^{-2} yr^{-1});

d= cumulative mass depth representing the average plough depth (kg m^{-2});

λ= decay constant for *^{137}Cs (yr^{-1});*

$I(t)$= annual ^{137}Cs deposition flux (Bq m^{-2} yr^{-1});

γ= is the proportion of the annual ^{137}Cs fallout susceptible to removal by erosion prior to incorporation into the soil profile by tillage

P= particle size correction factor.

The mass balance model described here takes account of both the temporal variation of the ^{137}Cs fallout input and its initial distribution in the surface soil. Results from this model are likely to be more realistic than the those provided by the simplified mass balance model 1 presented in the previous section. However, information on plough depth, relaxation mass depth H and parameter γ is required in order to use this model.

2.1.4 Mass Balance Model Incorporating Soil Movement by Tillage (Mass Balance Model 3):

The mass balance models discussed earlier do not consider the impact of tillage on soil redistribution. When soil is tilled, it leads to the movement of soil within a field, which in turn redistributes the ^{137}Cs present in the soil. Therefore, it is crucial to account for this re-distribution when using ^{137}Cs measurements to estimate erosion rates. By quantifying and incorporating the effects of tillage redistribution on ^{137}Cs inventories, it can be focused on the remaining component of redistribution, which specifically reflects the impact of water erosion. Taking tillage redistribution into account allows for a more accurate assessment of erosion rates based on ^{137}Cs measurements [109,112].

The effect of tillage in redistributing soil can be assumed to be represented by a downslope sediment flux. Following Govers et al. (1994, 1996) and Quint et al. (1996), the downslope sediment flux F_Q (kg m^{-1} yr^{-1}) from a unit contour length may be expressed as [112]:

$$F_Q = \emptyset sin\beta \qquad (44)$$

where β is the angle of steepest slope, and $\emptyset$ (kg m^{-1} yr^{-1}) is a constant related to the tillage practice involved.

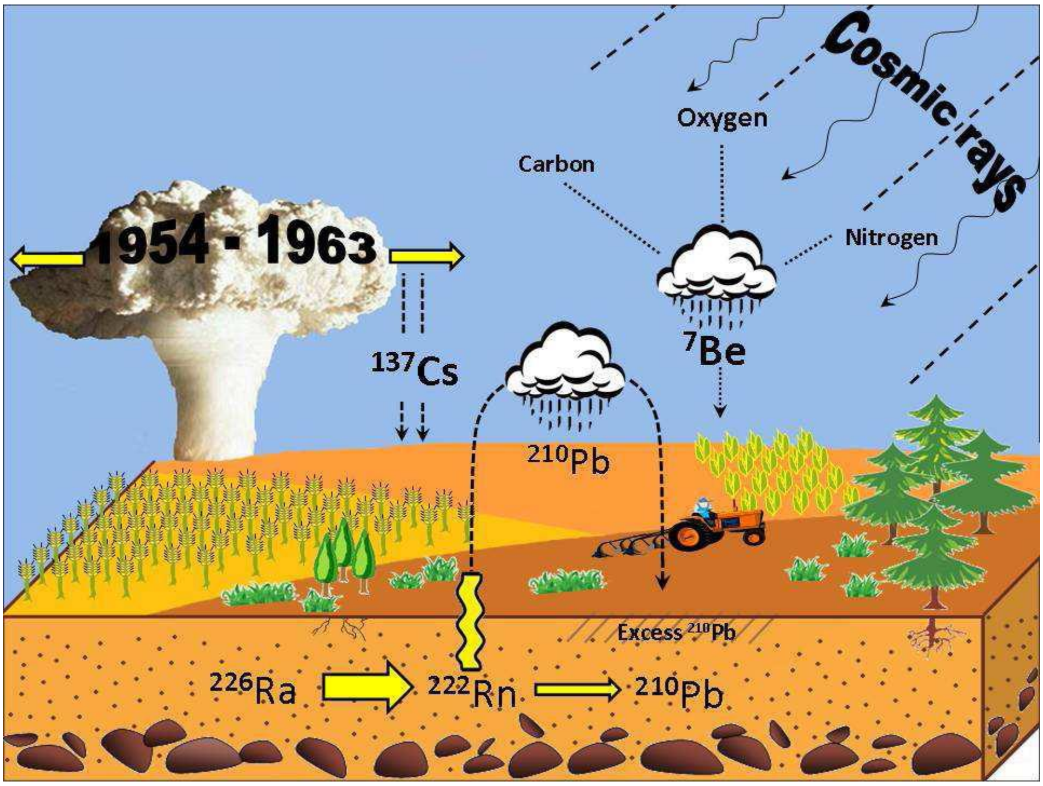

Figure 35. Fallout radionuclides (^{137}Cs, ^{7}Be, and ^{210}Pb$_{ex}$) Origin used as soil tracers in erosion and sedimentation studies [19].

2.2 Study of the cesium-137 transfer in cultivated areas

The previous correction models for soil erosion do not currently account for the fraction of cesium (Cs) that may be absorbed by plants. To address this limitation and improve the accuracy of erosion assessments, it is necessary to determine the specific activities of ^{137}Cs in both plant and soil samples. This will provide valuable information on the extent of ^{137}Cs uptake by plants and facilitate a conclusion regarding its transfer from the soil to the plant.

According to the Table 14, the analysis of soil samples revealed ^{137}Cs activity concentrations ranging from 4.77 to 6.56 Bq kg^{-1}. However, none of the collected plant samples showed any detectable traces of ^{137}Cs. Hence, there is no evident transfer of ^{137}Cs from the soil to the collected plant samples. This finding supports that the correction models are always available for studying erosion and can disregard the absorbed fraction of ^{137}Cs in the studied plants.

^{137}Cs activity concentration (Bq Kg^{-1})	Mustard	Onion	Bean	Garlic	Mushroom
Soil	4.77 ± 0.23	2.57 ± 0.54	3.40 ± 0.11	8.10 ± 0.10	6.56± 0.33
Crops	< DL	< DL	< DL	< DL	< DL

DL Of the $^{137}Cs = 0.0012$ $Bq.kg^{-1}$

Table 14. ^{137}Cs activity concentration in the studied soil samples

General Conclusion

In this thesis, we highlighted the experimental measurements problems that can be limited by some factors like self-absorption, coincidence summing, and the unavailability of standards for the detector calibration. These effects can influence the accuracy and reliability of the efficiency results, and therefore alters the activity concentrations of the environmental radionuclides. To overcome these difficulties, we developed a Monte Carlo model for an HPGe detector and a cylindrical geometry in order to optimize the experimental setups and to precisely evaluate the efficiency of the detector for the measuring geometry.

The developed model was simulated by MCNP5 code, which is a widely used software based on Monte Carlo methods. The code is specifically designed for simulating the passage of particles through matter, and it provides a versatile and comprehensive set of data for modern simulation applications. One of the strengths of MCNP5 is its ability to handle complex geometries efficiently and compactly. It allows users to define intricate and detailed geometries which makes it well-suited for simulating a wide range of systems, from simple to highly complex. Another feature of MCNP5 is its ability to provide visualization of the geometry and particle tracks. This allows users to visually inspect the simulated system, including the positions and paths of particles as they interact with the materials. The visualization capability can aid in understanding the behavior of particles in complex systems and in validating the simulation results.

The simulations were performed for both plant and soil matrices in which the different elements of each matrix were measured by WD-XRF analytical technique. The model was validated by the experimental gamma ray standard solution type ERX certified by Czech Metrology Institute, through the calculation of the FEPE for a wide energy range (59.54 –1836.12) keV for both matrices.

The Monte Carlo simulation model was applied to correct the self-absorption and summing coincidence effects as well as to evaluate the likely variation in self-absorption as a function of energy and matrix composition for soil and plant. The results indicate that the self-absorption effect depends on the variation of the matrix composition basically at low gamma energies in which the FEPE values of low gamma energies are affected by the matrix composition, where in the soil matrix the FEPEs decreased by 36% and only by 1% in the plant matrix. These results provide valuable insights into the behavior of gamma rays in different matrices, which can be used to improve the accuracy of gamma spectrometry measurements in a range of applications.

The simulated HPGe-source detector was then used for the determination of the activity concentrations of ^{226}Ra, ^{232}Th, ^{40}K, and ^{137}Cs for artichoke, fennel, mustard, bean, mushroom, onion and garlic crops with their corresponding soils, harvested from different agricultural areas in Algeria. The transfer factors of those radionuclides were evaluated using the activity concentration of each radionuclide in the soil and crop sample. The determination of TFs provides a preliminary data of the radioactivity level in the studied areas, and it serves as an initial measurement that can be used as a starting point for further investigation or monitoring. The transfer of ^{137}Cs from soil to crops were determined in order to validate and correct the existed soil erosion models. The study found that there was no significant transfer under consideration.

Therefore, the simulated model with the measuring geometry is suitable and reliable enough for the purpose of determining the activity concentrations of soil and plant environmental samples, taking into account the self-absorption and coincidence summing effect corrections.

To enhance our understanding of radionuclide transfer from soil to crops in Algeria, adopting a larger perspective by including a wide variety of crops. This will yield a more robust dataset, for making well informed decisions to safeguard the environment and human health.

References

[1]. Vosniakos, F. K. (2012). *Radioactivity transfer in environment and food*. Springer Science & Business Media.

[2]. Isaksson, M., & Raaf, C. L. (2017). *Environmental radioactivity and emergency preparedness*. CRC Press.

[3] Hassan, N. M., Kim, Y. J., Jang, J., Chang, B. U., & Chae, J. S. (2018). Comparative study of precise measurements of natural radionuclides and radiation dose using in-situ and laboratory γ-ray spectroscopy techniques. Scientific reports, 8(1), 1-11.

[4] Amatullah, S., Rahman, R., Ferdous, J., Siraz, M. M. M., Khandaker, M. U., & Mahal, S. F. (2021). Assessment of radiometric standard and potential health risks from building materials used in Bangladeshi dwellings. *International Journal of Environmental Analytical Chemistry*, 1-13.

[5] Sabatino, G., Di Bella, M., Caridi, F., Italiano, F., Romano, D., Magazù, S., ... & Tripodo, A. (2019). Radiological assessment, mineralogy and geochemistry of the heavy-mineral placers from the Calabrian coast (South Italy). *Journal of Instrumentation*, *14*(05), P05015.

[6] Suman, G., Vinay Kumar Reddy, K., Sreenath Reddy, M., Vidyasagar, D., Gopal Reddy, C., & Yadagiri Reddy, P. (2020). Dose assessment due to natural gamma radiation levels and radioactive nuclides in the environment of Dasarlapally, Nalgonda District, Telangana State, India. *International Journal of Environmental Analytical Chemistry*, 1-10.

[7] Krneta Nikolić, J., Rajačić, M., Todorović, D., Janković, M., Sarap, N., Pantelić, G., & Vukanac, I. (2018). Semiempirical efficiency calibration in semiconductor HPGe gamma-ray spectroscopy. *Journal of Spectroscopy*, *2018*.

[8] Santo, A. S., Wasserman, F. G., & Conti, C. C. (2012). HPGe well detector calibration procedure by MCNP5 Monte Carlo computer code. *Annals of Nuclear Energy*, *46*, 213-217.

[9] Joel, G. S. C., Maurice, N. M., Jilbert, N. M. E., Ousmanou, M., & David, S. (2018). Monte Carlo method for gamma spectrometry based on GEANT4 toolkit: Efficiency calibration of BE6530 detector. *Journal of Environmental Radioactivity*, *189*, 109-119.

[10] Pires, L. F. (2018). Soil analysis using nuclear techniques: A literature review of the gamma ray attenuation method. *Soil and Tillage Research*, *184*, 216-234.

References

[11] Gouda, M. M., Hamzawy, A., Badawi, M. S., El-Khatib, A. M., Thabet, A. A., & Abbas, M. I. (2016). Mathematical method to calculate full-energy peak efficiency of detectors based on transfer technique. Indian Journal of Physics, 90, 201-210

[12] Prozorova, I. V., Sabitova, R. R., Ghal-Eh, N., & Bedenko, S. V. (2019). Modeling an HPGe detector response to gamma-rays using MCNP5 code. *International Journal of Modern Physics C*, *30*(11), 1950099.

[13] Belgin, E. E., & Aycik, G. A. (2015). Derivation of an efficiency-calibration simulation for a well-type HPGe detector using the Monte Carlo approach and analytical techniques. *Radiation Measurements*, *73*, 36-45.

[14] Mostafa, M. Y., Kadhim, N. F., Ammer, H., & Baqir, Y. (2021). The plant transfer factor of natural radionuclides and the soil radiation hazard of some crops. *Environmental Monitoring and Assessment*, *193*(6), 320.

[15]. Debertin, K., & Helmer, R. G. (1988). Gamma-and X-ray spectrometry with semiconductor detectors.

[16]. Tyler, A. N. (1994). *Environmental influences on gamma ray spectrometry* (Doctoral dissertation, University of Glasgow).

[17]. Gilmore, G. (2008). *Practical gamma-ray spectroscopy*. John Wiley & Sons.

[18]. Glascock, M. D. (2014). Nuclear spectroscopy.

[19]. Azbouche, A. (2015). *Développement d'une méthodologie d'analyse par spectrométrie gamma et par activation neutronique pour l'étude de la distribution des radio-traceurs et des terres rares dans le sol* (Doctoral dissertation, USTHB).

[20]. Lilley, J. (2013). *Nuclear physics: principles and applications*. John Wiley & Sons.

[21]. Knoll, G. F. (2010). *Radiation detection and measurement*. John Wiley & Sons.

[22]. Ahmed, S. N. (2007). *Physics and engineering of radiation detection*. Academic Press.

[23]. Dziri, S. (2013). *Etudes expérimentales et simulations Monte Carlo en spectrométrie γ: Correction des effets de cascade et de matrice pour des mesures environnementales* (Doctoral dissertation, Université de Strasbourg).

[24]. Guembou Shouop, C. J., Mbida Mbembe, S., Tayou Kamkumo, C., Beyala Ateba, J. F., Ndontchueng Moyo, M., Nguelem Mekongtso, E. J., ... & Strivay, D. (2022). Monte Carlo optimum management of 241Am/Be disused sealed radioactive sources. *Scientific Reports*, *12*(1), 1183.

References

[25]. Liang, Y., Muhammad, W., Hart, G. R., Nartowt, B. J., Chen, Z. J., Yu, J. B., ... & Deng, J. (2020). A general-purpose Monte Carlo particle transport code based on inverse transform sampling for radiotherapy dose calculation. *Scientific reports*, *10*(1), 1-18.

[26]. Nachab, A. (2003). *Etudes expérimentales et modélisations Monte Carlo de l'auto-absorption gamma et de la dosimétrie active par capteurs CMOS* (Doctoral dissertation, Université Louis Pasteur-Strasbourg I).

[27]. GOURIOU, J. (2012). Utilisation des codes de Monte-Carlo dans l'établissement de références dosimétriques pour les rayonnements ionisants. *Revue française de métrologie*, (29), 13-24.

[28]. Agostinelli, S., Allison, J., Amako, K. A., Apostolakis, J., Araujo, H., Arce, P., ... & Geant4 Collaboration. (2003). GEANT4—a simulation toolkit. *Nuclear instruments and methods in physics research section A: Accelerators, Spectrometers, Detectors and Associated Equipment*, *506*(3), 250-303.

[29]. Collaboration, G. E. A. N. T., & Agostinelli, S. (2003). GEANT4–a simulation toolkit. *Nucl. Instrum. Meth. A*, *506*(25), 0.

[30]. Battistoni, G., Pinsky, L., Tsoulou, A., Roesler, S., Vlachoudis, V., Muraro, S., ... & Ranft, J. (2005). Applications of the FLUKA Monte Carlo code in High Energy and Accelerator Physics.

[31]. Salvat, F., Fernández-Varea, J. M., & Sempau, J. (2006, July). PENELOPE-2006: A code system for Monte Carlo simulation of electron and photon transport. In *Workshop proceedings* (Vol. 4, No. 6222, p. 7). Barcelona, Spain: Nuclear Energy Agency, Organization for Economic Co-operation and Development.

[32]. Ródenas, J., Gallardo, S., Ballester, S., Primault, V., & Ortiz, J. (2007). Application of the Monte Carlo method to the analysis of measurement geometries for the calibration of a HP Ge detector in an environmental radioactivity laboratory. *Nuclear Instruments and Methods in Physics Research Section B: Beam Interactions with Materials and Atoms*, *263*(1), 144-148.

[33]. Mantero, J., Gázquez, M. J., Hurtado, S., Bolivar, J. P., & García-Tenorio, R. (2015). Application of gamma-ray spectrometry in a NORM industry for its radiometrical characterization. *Radiation Physics and Chemistry*, *116*, 78-81.

[34]. Al-Masri, M. S., Hasan, M., Al-Hamwi, A., Amin, Y., & Doubal, A. W. (2013). Mass attenuation coefficients of soil and sediment samples using gamma energies from 46.5 to 1332 keV. *Journal of environmental radioactivity*, *116*, 28-33.

References

[35]. Ajemigbitse, M. A., Cheng, Y., Cannon, F. S., & Warner, N. R. (2020). Self-attenuation corrections for radium measurements of oil and gas solids by gamma spectroscopy. *Journal of environmental radioactivity*, *211*, 106070.

[36]. Landsberger, S., Brabec, C., Canion, B., Hashem, J., Lu, C., Millsap, D., & George, G. (2013). Determination of 226Ra, 228Ra and 210Pb in NORM products from oil and gas exploration: Problems in activity underestimation due to the presence of metals and self-absorption of photons. *Journal of environmental radioactivity*, *125*, 23-26.

[37]. Barba-Lobo, A., Mosqueda, F., & Bolívar, J. P. (2021). A general function for determining mass attenuation coefficients to correct self-absorption effects in samples measured by gamma spectrometry. *Radiation Physics and Chemistry*, *179*, 109247.

[38]. Briesmeister, J. F. (2000). MCNPTM-A general Monte Carlo N-particle transport code. *Version 4C, LA-13709-M, Los Alamos National Laboratory*, *2*.

[39]. Potts, P. J., & Webb, P. C. (1992). X-ray fluorescence spectrometry. *Journal of Geochemical Exploration*, *44*(1-3), 251-296.

[40]. Yao, M., Wang, D., & Zhao, M. (2015). Element analysis based on energy-dispersive X-ray fluorescence. *Advances in Materials Science and Engineering*, *2015*.

[41]. Sokoltsova, T. (2021). *Development of a standardless miniature XRF setup for the analysis of actinides: coupling MC methods with fundamental parameters* (Doctoral dissertation, Université Paris-Saclay).

[42]. Marguí, E., Queralt, I., & Hidalgo, M. (2009). Application of X-ray fluorescence spectrometry to determination and quantitation of metals in vegetal material. *TrAC Trends in Analytical Chemistry*, *28*(3), 362-372.

[43]. Milazzo, M., & Cicardi, C. (1997). Simple methods for quantitative X-ray fluorescence analysis of ancient metal objects of archaeological interest. *X-Ray Spectrometry: An International Journal*, *26*(4), 211-216.

[44]. Mezerreg, N., Azbouche, A., & Haddad, M. (2021). Study of coincidence summing effect using Monte Carlo simulation to improve large samples measurement for environmental applications. *Journal of Environmental Radioactivity*, *232*, 106573.

[45]. Azbouche, A., Belamri, M., & Tchakoua, T. (2018). Study of the germanium dead layer influence on HP (Ge) detector efficiency by Monte Carlo simulation. *Radiation Detection Technology and Methods*, *2*, 1-6.

References

[46]. Canberra Industries, 2008a. Solid-State Photon Detector, Operators Manual, GMX Series, HPGe (High-Purity Germanium). Canberra Industries.

[47]. Pająk, M., Gąsiorek, M., Jasik, M., Halecki, W., Otremba, K., & Pietrzykowski, M. (2020). Risk assessment of potential food chain threats from edible wild mushrooms collected in Forest ecosystems with heavy metal pollution in upper Silesia, Poland. *Forests*, *11*(12), 1240.

[48]. Azbouche, A., Belgaid, M., & Mazrou, H. (2015). Monte Carlo calculations of the HPGe detector efficiency for radioactivity measurement of large volume environmental samples. *Journal of environmental radioactivity*, *146*, 119-124.

[49]. Elanique, A., Marzocchi, O., Leone, D., Hegenbart, L., Breustedt, B., & Oufni, L. (2012).Dead layer thickness characterization of an HPGe detector by measurements and Monte Carlo simulations. *Applied Radiation and Isotopes*, *70*(3), 538-542.

[50]. Trang, L. T. N., Chuong, H. D., & Thanh, T. T. (2021). Optimization of p-type HPGe detector model using Monte Carlo simulation. *Journal of Radioanalytical and Nuclear Chemistry*, *327*, 287-297.

[51]. Jurado Vargas, M., Fernandez Timon, A., Cornejo Díaz, N., & Pérez Sánchez, D. (2002). Monte Carlo simulation of the self-absorption corrections for natural samples in gamma-ray spectrometry. *Applied radiation and isotopes*, *57*(6), 893-898.

[52].https://assets.thermofisher.com/TFS-Assets/MSD/Application-Notes/XRF-AN41963-edxrf-cement-analysis-astm-c114.pdf

[53]. Van der Graaf, E. R., Limburg, J., Koomans, R. L., & Tijs, M. (2011). Monte Carlo based calibration of scintillation detectors for laboratory and in situ gamma ray measurements. *Journal of environmental radioactivity*, *102*(3), 270-282.

[54]. Olivares, D. M. M., Guevara, M. M., & Velasco, F. G. (2017). Determination of the HPGe detector efficiency in measurements of radioactivity in extended environmental samples. *Applied Radiation and Isotopes*, *130*, 34-42.

[55]. Ba, V. N., Thien, B. N., & Loan, T. T. H. (2021). Effects of element composition in soil samples on the efficiencies of gamma energy peaks evaluated by the MCNP5 code. *Nuclear Engineering and Technology*, *53*(1), 337-343.

[56]. Huy, N. Q. (2014). A semi-empirical approach to analyze the activities of cylindrical radioactive samples using gamma energies from 185 to 1764 keV. *Applied Radiation and Isotopes*, *94*, 82-88.

References

[57]. Appleby, P. G., Richardson, N., & Nolan, P. J. (1992). Self-absorption corrections for well-type germanium detectors. *Nuclear Instruments and Methods in Physics Research Section B: Beam Interactions with Materials and Atoms*, *71*(2), 228-233.

[58]. Saat, A. (1996). A review and a preleminary study on self-absorption correction in gamma-spectrometry. *GADING Jurnal Akademik ITM Cawangan Pahang*, *2*(1), 49-60.

[59]. Semkow, T. M., Mehmood, G., Parekh, P. P., & Virgil, M. (1990). Coincidence summing in gamma-ray spectroscopy. *Nuclear Instruments and Methods in Physics Research Section A: Accelerators, Spectrometers, Detectors and Associated Equipment*, *290*(2-3), 437-444.

[60]. McCallum, G. J., & Coote, G. E. (1975). Influence of source-detector distance on relative intensity and angular correlation measurements with Ge (Li) spectrometers. *Nuclear Instruments and Methods*, *130*(1), 189-197.

[61]. Kafala. S. (1995). Simple method for true coincidence summing correction. *Journal of radioanalytical and nuclear chemistry*. *191*(1). 105-114.

[62]. Dziri, S., Nachab, A., Nourreddine, A., Sellam, A., & Pape, A. (2014). Elemental composition effects on self-absorption for photons below 100 keV in gamma-ray spectrometry. *Nuclear Instruments and Methods in Physics Research Section B: Beam Interactions with Materials and Atoms*, *330*, 1-6.

[63]. Huy, N. Q., An, V. X., Loan, T. T. H., & Can, N. T. (2013). Self-absorption correction in determining the 238U activity of soil samples via 63.3 keV gamma ray using MCNP5 code. *Applied Radiation and Isotopes*, *71*(1), 11-20.

[64]. Bolivar. J. P.. Garcia-Leon. M.. & Garcia-Tenorio. R. (1997). On self-attenuation corrections in gamma-ray spectrometry. *Applied radiation and isotopes*. *48*(8). 1125-1126.

[65]. Ba, C. A., Fegan, M. F., Wong, J., Long, S. C., Ryan, T. P., & Colgan, P. A. (2004). Determination of self-absorption corrections for gamma analysis of environmental samples: comparing gamma-absorption curves and spiked matrix-matched samples. *Applied radiation and isotopes*, *60*(2-4), 571-577.

[66]. Gharbi, F. (2021). Correction of the chemical composition effect for soil samples in gamma spectrometry. *Applied Radiation and Isotopes*, *169*, 109512.

[67]. McMahon, C. A., Fegan, M. F., Wong, J., Long, S. C., Ryan, T. P., & Colgan, P. A. (2004). Determination of self-absorption corrections for gamma analysis of environmental samples:

comparing gamma-absorption curves and spiked matrix-matched samples. *Applied radiation and isotopes*, *60*(2-4), 571-577.

[68] Jodłowski, P., Wachniew, P., & Nowak, J. (2017). Determination of the self-attenuation based on the sample composition in gamma-ray spectrometry of 210 Pb: requirements for the scope of chemical analyses. *Journal of Radioanalytical and Nuclear Chemistry*, *311*, 1511-1516.

[69]. Fergusson, J. E., & Prucha, F. P. (1990). *The heavy elements: chemistry, environmental impact and health effects* (Vol. 614). Oxford: Pergamon press.

[70]. FAO, J. W. (2007). FAO Food Standard Programme Codex Alimentarius Commission 13TH session. *Report of the Thirty-Eight Session of the Codex Com. on Food Hyg., Houston, United States of America, AliNorm*.

[71]. Shanthi, G., Thanka Kumaran, J. T., Gnana Raj, G. A., & Maniyan, C. G. (2012). Transfer factor of the radionuclides in food crops from high-background radiation area of south west India. *Radiation protection dosimetry*, *149*(3), 327-332.

[72]. Al-Hamarneh, I. F., Alkhomashi, N., & Almasoud, F. I. (2016). Study on the radioactivity and soil-to-plant transfer factor of 226Ra, 234U and 238U radionuclides in irrigated farms from the northwestern Saudi Arabia. *Journal of environmental radioactivity*, *160*, 1-7.

[73]. ADESIJI, N. E. (2021). *SOIL-TO-PLANT TRANSFER FACTORS OF NATURAL RADIONUCLIDES OF THREE COMMON FOOD CROPS GROWN ON A TIN-MINING IMPACTED SOIL* (Doctoral dissertation).

[74]. Djedidi, S., Terasaki, A., Aung, H. P., Kojima, K., Yamaya, H., Ohkama-Ohtsu, N., ... & Yokoyama, T. (2015). Evaluation of the possibility to use the plant–microbe interaction to stimulate radioactive 137 Cs accumulation by plants in a contaminated farm field in Fukushima, Japan. *Journal of plant research*, *128*, 147-159.

[75]. Punetha, D., Pande, C., Tewari, G., Bhatt, S., Tewari, K., Diwakar, J., & Tripathi, S. EFFECT OF METAL CONTAMINATED SOIL ON Foeniculum vulgare.

[76]. Yoshida, S., Muramatsu, Y., Tagami, K., Uchida, S., Ban-nai, T., Yonehara, H., & Sahoo, S. (2000). Concentrations of uranium and 235U/238U ratios in soil and plant samples collected around the uranium conversion building in the JCO campus. *Journal of Environmental Radioactivity*, *50*(1-2), 161-172.

References

[77]. Perveen, S., Samad, A. B. D. U. S., Nazif, W., & Shah, S. (2012). Impact of sewage water on vegetables quality with respect to heavy metals in Peshawar, Pakistan. *Pakistan Journal of Botany, 44*(6), 1923-1931.

[78]. Świsłowski, P., & Rajfur, M. (2018). Mushrooms as biomonitors of heavy metals contamination in forest areas. *Ecological Chemistry and Engineering S, 25*(4), 557-568.

[79]. Yakovlev, E. Y., Zykova, E. N., Zykov, S. B., Malkov, A. V., & Bazhenov, A. V. (2020). Heavy metals and radionuclides distribution and environmental risk assessment in soils of the Severodvinsk industrial district, NW Russia. *Environmental Earth Sciences, 79*(10), 218.

[80]. Širić, I., Humar, M., Kasap, A., Kos, I., Mioč, B., & Pohleven, F. (2016). Heavy metal bioaccumulation by wild edible saprophytic and ectomycorrhizal mushrooms. *Environmental science and pollution research, 23*, 18239-18252.

[81]. Asaduzzaman, K., Khandaker, M. U., Amin, Y. M., Bradley, D. A., Mahat, R. H., & Nor, R. M. (2014). Soil-to-root vegetable transfer factors for 226Ra, 232Th, 40K, and 88Y in Malaysia. *Journal of environmental radioactivity, 135*, 120-127.

[82]. Balonov, M., Barnett, C. L., Belli, M., Beresford, N. A., Berkovsky, V., Bossew, P., ... & Zibold, G. (2010). Handbook of parameter values for the prediction of radionuclide transfer in terrestrial and freshwater environments.

[83]. Tyovenda, A. A., Ocheje, J. A., Terver, S., & Uttah, E. U. (2022). Investigation of the radiological risk of farmlands and the transfer factor from soil to crops in Jalingo and Wukari LGA of Taraba State, Nigeria. *Journal of Environmental Protection, 13*(1), 1-14.

[84]. Kolapo, A. A., & Omoboyede, J. O. (2018). Health risk assessment of natural radionuclide and heavy metals in commonly consumed medicinal plants in south-west Nigeria. *Ife Journal of Science, 20*(3), 529-537.

[85]. IAEA, Handbook of parameter values for the prediction of radionuclide transfer in temperate environments, Technical Report Series (TRS) No. 472, International Atomic Energy Agency, 2010.

[86]. UNSCEAR, 2000. United Nations Scientific Committee on the Effects of Atomic Radiation, Sources and Effects of Ionizing Radiation, Report to the General Assembly, with Scientific Annexes, United Nations, New York.

References

[87]. Salih, N. F. (2023). Measurement the natural radioactivity concentration levels of radionuclides in selected vegetables collected from Kirkuk, Iraq using HPGe detector. *International Journal of Environmental Analytical Chemistry*, *103*(6), 1323-1342.

[88]. Kh, A., Khandaker, M. U., Amin, Y. M., & Mahat, R. (2015). Uptake and distribution of natural radioactivity in rice from soil in northand west part of peninsular Malaysia for the estimation of ingestion dose to man. *Ann Nucl Energy, 76*, 85-93.

[89]. Kadhim, N. F., Khalaf, H. N. B., Hassan, H. A., & Mostafa, M. Y. (2021). Determining the natural radioactivity of spices widely used in Iraq. *International Journal of Environmental Analytical Chemistry*, 1-12.

[90]. Dreyer, I., & Uozumi, N. (2011). Potassium channels in plant cells. *The FEBS Journal*, *278*(22), 4293-4303.

[91]. Balabanova, B., Stafilov, T., Šajn, R. and Bačeva, K. (2014). Comparison of response of moss, lichens and attic dust to geology and atmospheric pollution from copper mine. International Journal of Environmental Science and Technology 11: 517-528.

[92]. Yan, X., Zhang, F., Zeng, C., Zhang, M., Devkota, L. P. and Yao, T. (2012). Relationship between heavy metal concentrations in soils and grasses of roadside farmland in Nepal. International Journal of Environmental Research and Public Health 9: 3209-3226.

[93]. Intawongse, M., & Dean, J. R. (2006). Uptake of heavy metals by vegetable plants grown on contaminated soil and their bioavailability in the human gastrointestinal tract. *Food additives and contaminants*, *23*(1), 36-48.

[94]. Li, Z., Ma, Z., van der Kuijp, T. J., Yuan, Z., & Huang, L. (2014). A review of soil heavy metal pollution from mines in China: pollution and health risk assessment. *Science of the total environment*, *468*, 843-853.

[95]. Obiora, S. C., Chukwu, A., & Davies, T. C. (2016). Heavy metals and health risk assessment of arable soils and food crops around Pb–Zn mining localities in Enyigba, southeastern Nigeria. *Journal of African Earth Sciences*, *116*, 182-189.

[96]. Dudka, S., Piotrowska, M., & Terelak, H. (1996). Transfer of cadmium, lead, and zinc from industrially contaminated soil to crop plants: a field study. *Environmental Pollution*, *94*(2), 181-188.

References

[97]. Liu, S., Peng, B., & Li, J. (2022). Ecological risk evaluation and source identification of heavy metal pollution in urban village soil based on XRF technique. *Sustainability*, *14*(9), 5030.

[98]. Khan, A., Khan, S., Khan, M. A., Qamar, Z., & Waqas, M. (2015). The uptake and bioaccumulation of heavy metals by food plants, their effects on plants nutrients, and associated health risk: a review. *Environmental science and pollution research*, *22*, 13772-13799.

[99]. Mirecki, N., Agic, R., Sunic, L., Milenkovic, L., & Ilic, Z. S. (2015). Transfer factor as indicator of heavy metals content in plants. *Fresenius Environmental Bulletin*, *24*(11c), 4212-4219.

[100]. Tuovinen, T. S., Roivainen, P., Makkonen, S., Kolehmainen, M., Holopainen, T., & Juutilainen, J. (2011). Soil-to-plant transfer of elements is not linear: results for five elements relevant to radioactive waste in five boreal forest species. *Science of the total environment*, *410*, 191-197.

[101]. Golmakani, S., Moghaddam, M. V., & Hosseini, T. (2008). Factors affecting the transfer of radionuclides from the environment to plants. *Radiation Protection Dosimetry*, *130*(3), 368-375.

[102]. Simon, S. L., Graham, J. C., & Terp, S. D. (2002). Uptake of 40K and 137Cs in native plants of the Marshall Islands. *Journal of environmental radioactivity*, *59*(2), 223-243.

[103]. Ibikunle, S. B., Arogunjo, A. M., & Ajayi, O. S. (2019). Characterization of radiation dose and soil-to-plant transfer factor of natural radionuclides in some cities from south-western Nigeria and its effect on man. *Scientific African*, *3*, e00062.

[104]. Balasubramanian, A. (2017). Soil erosion–causes and effects. *Centre for Advanced Studies in Earth Science, University of Mysore, Mysore*.

[105]. Latrubesse, E. (2009). *Natural Hazards and Human-Exacerbated Disasters in Latin America: Special Volumes of Geomorphology*. Elsevier.

[106]. Bernard, C., & Mabit, L. (2006). The use of radionuclide techniques in soil erosion studies.

[107]. Joint, F. A. O. (2014). *Guidelines for using fallout radionuclides to assess erosion and effectiveness of soil conservation strategies* (No. IAEA-TECDOC--1741). Joint FAO/IAEA Division of Nuclear Techniques in Food and Agriculture.

References

[108]. Rahman, R. A. (Ed.). (2020). *Isotopes Applications in Earth Sciences*. BoD–Books on Demand.

[109]. Ritchie, J. C., & McHenry, J. R. (1990). Application of radioactive fallout cesium-137 for measuring soil erosion and sediment accumulation rates and patterns: A review. *Journal of environmental quality*, *19*(2), 215-233.

[110]. Ritchie, J. C., & Ritchie, C. A. (2007). Bibliography of publications of ^{137}Cesium studies related to erosion and sediment deposition. *USDA–ARS Hydrology and Remote Sensing Laboratory Occasional Paper HRSL-2007-01. USDA–Agricultural Research Service, Beltsville, MD, USA.*

[109]. Zapata, F. (Ed.). (2002). *Handbook for the assessment of soil erosion and sedimentation using environmental radionuclides* (Vol. 219, pp. 9348054-9). Dordrecht: Kluwer Academic Publishers.

[111]. Arata, L., Meusburger, K., Frenkel, E., A'Campo-Neuen, A., Iurian, A. R., Ketterer, M. E., ... & Alewell, C. (2016). Modelling Deposition and Erosion rates with RadioNuclides (MODERN)–Part 1: A new conversion model to derive soil redistribution rates from inventories of fallout radionuclides. *Journal of environmental radioactivity*, *162*, 45-55.

[112]. Mabit, L., Meusburger, K., Fulajtar, E., & Alewell, C. (2013). The usefulness of 137Cs as a tracer for soil erosion assessment: A critical reply to Parsons and Foster (2011). *Earth-science reviews*, *127*, 300-307.

[113]. Walling, D. E., & He, Q. (1999). *Improved models for estimating soil erosion rates from cesium-137 measurements* (Vol. 28, No. 2, pp. 611-622). American Society of Agronomy, Crop Science Society of America, and Soil Science Society of America.

[114]. Muñoz-Arcos, E., Millward, G. E., Clason, C. C., Bravo-Linares, C., & Blake, W. H. (2022). Understanding the complexity of sediment residence time in rivers: Application of Fallout Radionuclides (FRNs). *Earth-Science Reviews*, 104188.